Aerodynamic Optimisation of a Turbofan Bypass Duct with a Heat Exchanger Modelled as a Porous Zone

Kalyan Wessendorp

Delft University of Technology

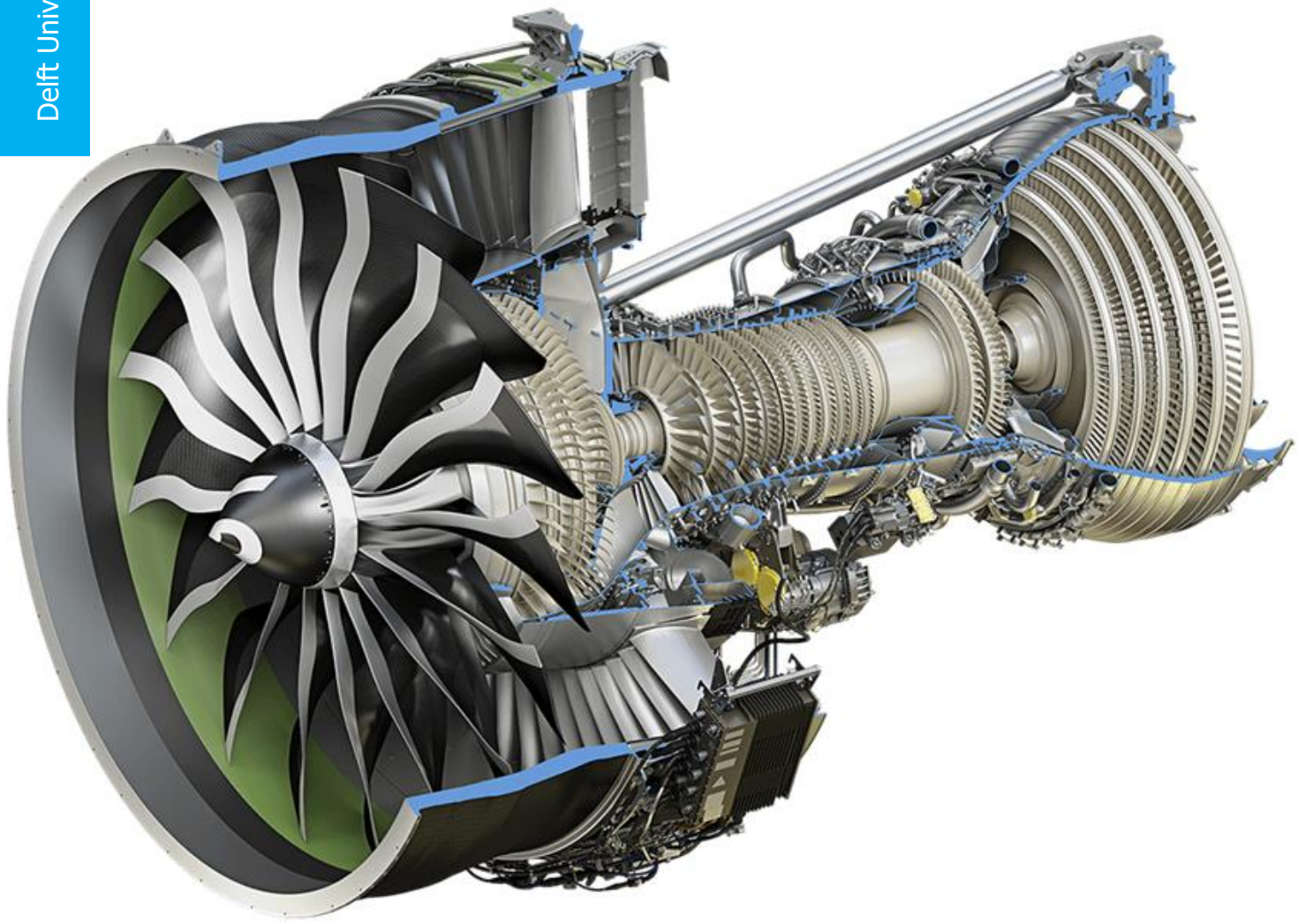

TU Delft Delft University of Technology

Challenge the future

Aerodynamic Optimisation of a Turbofan Bypass Duct with a Heat Exchanger Modelled as a Porous Zone

By

Kalyan Wessendorp

in partial fulfilment of the requirements for the degree of

Master of Science
in Aerospace Engineering

at the Delft University of Technology,
to be defended publicly on Thursday June 19th, 2025 at 1:00 PM.

Supervisors:	Dr. ir. M. Pini	TU Delft
	ir. F. Beltrame	TU Delft

Cover: Turbofan engine cross-sectional view (iStock photo)
An electronic version of this thesis is available at http://repository.tudelft.nl/.

Preface

This thesis marks the end of a very enjoyable student journey at TU Delft. I feel very fortunate to have studied a field I've been passionate about since I was a little boy, but what made the experience truly special were the people around me who supported me and shared the journey.

To start with, grazie mille Fabio, for the guidance and support you have given me throughout the thesis. I've learned a great deal from you and feel privileged to have had you as supervisor. Thank you, Matteo, for offering valuable feedback and for the fresh perspective you brought to our meetings. And thanks, Huger, for being a trusty companion on this thesis journey and sparring ideas back and forth with me.

To my parents and my brother – you've been there for me all along and always given me great encouragement, especially during my Master's degree where things weren't always plain sailing. I look forward to spending some overdue quality time with all of you now that this thesis is completed.

To my friends, you've had my back, made me feel loved and given me some unforgettable times throughout my Bachelor's and Master's. There are really too many moments to share but suffice it to say that I have built up so many more great memories than I could have hoped for.

Dear reader, I hope you find this thesis both informative and enjoyable. A more sustainable future for aviation is within reach, let's do what we can to contribute and make it a reality.

Kalyan Wessendorp
Delft, June 2025

Contents

Aerodynamic Optimisation of a Turbofan Bypass Duct with a Heat Exchanger Modelled as a Porous Zone

Kalyan Wessendorp

The drive for improved fuel efficiency and decreased environmental impact has resulted in the development of advanced jet engine concepts that utilise waste heat recovery, including intercooled-recuperated engines and combined-cycle turbofans (CC-TF). A promising CC-TF variant employs an Organic Rankine Cycle (ORC) bottoming unit to recover waste heat, however it also requires extensive heat dissipation. Integrating a condenser into the bypass duct is a potential solution to meet this heat dissipation requirement. Axisymmetric RANS CFD simulations are employed to simulate this configuration and optimise aerodynamic performance, requiring simplified models for computational efficiency. This study quantifies the effect of the condenser integration on bypass stream net thrust and applies a gradient-based optimisation framework to refine the bypass duct geometry for improved thrust generation. The condenser air-side pressure drop and heat transfer performance are modelled through a porous zone, while the effect of the fan and OGV on the airflow pressure and velocity are predicted using actuator disk models. The integration of the CC-TF condenser results in a 13.7% net thrust penalty, however this penalty is reduced to 9.29% when simulating the heat added by the condenser to the airflow. The optimised bypass duct design further improves net thrust by 3.32% compared to the initial condenser integration approach. The actuator disk setup has been verified and validated by comparing the fan and OGV performance to predictions made by other CFD studies and to data collected in the wind tunnel by the NASA R4 engine. Verification studies also confirmed sufficient mesh refinement and correct porous zone calibration. Future studies can expand on this framework to incorporate the power generated by the ORC unit and assess potential fuel savings.

1 Introduction

Jet engine design is rapidly evolving, driven by the imperative to enhance the fuel efficiency of passenger aircraft. While this can be partially attributed to the significant increase in fuel prices over the past 20 years [1], these efficiency improvements are essential for minimising the aviation industry's environmental impact, currently contributing around 3% of total greenhouse gas emissions [2]. The International Civil Aviation Organization's (ICAO) member states adopted a long-term target of reaching net-zero carbon dioxide emissions from international aviation by 2050 [3]. The emerging new propulsion systems, such as hybrid electric configurations, internal combustion engines using hydrogen as fuel, intercooled-recuperated turbofans and combined-cycle turbofans (CC-TF), are a potential solution to mitigate these greenhouse emissions. However, these solutions often have larger thermal power dissipation requirements, and the thermal management systems must be adapted accordingly.

The CC-TF configuration combines the gas turbine Brayton cycle with a bottoming Organic Rankine Cycle (ORC), which harvests thermal energy from the hot exhaust of the gas turbine and converts it into additional power to improve engine efficiency. Figure 1 depicts a simplified process flow diagram of the waste heat recovery (WHR) unit. Studies have shown that this process not only has the potential to increase the engine's efficiency but also reduce fuel consumption and lower emissions [4]. The ORC system requires a heat sink for the condensation of the organic working fluid, which can be provided by the cold airflow passing through the turbofan bypass duct [5].

The integration of a HEX in the bypass duct poses some design challenges. Mainly, the drag penalty should be as low as possible to maximise the propulsive efficiency and reduce fuel consumption. Van Dongen [6] used a lumped parameter model to assess the aerodynamic performance of a HEX in

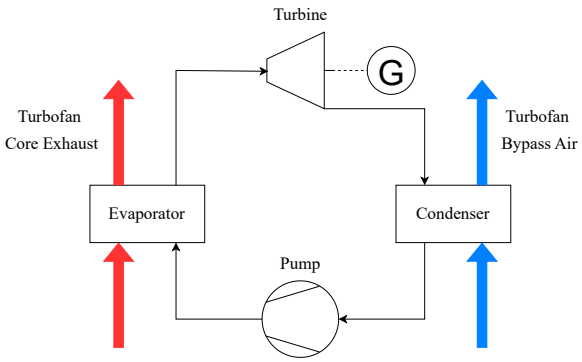

Figure 1: The simplified process flow diagram of the bottoming ORC unit of the CC-TF engine concept.

a ram-air duct, specifically the condenser of a CC-TF. The model was compared with CFD simulations of the HEX and ducts. However, the model did not encompass the effect of the turbofan geometry when integrating the condenser inside the turbofan engine. Similarly, other studies have also explored the possibility of integrating a HEX in the bypass duct using CFD simulations [7]–[10]. Despite the insights provided by these studies, none have simulated the influence of the upstream fan or the external airflow around the engine nacelle in configurations where a HEX is positioned within the bypass duct.

Therefore, this study aims at simulating the airflow through the bypass duct of a turbofan engine housing a condenser. The objective of the study is to develop a computationally efficient framework to optimise the bypass duct shape to maximise thrust, leveraging the thermal energy discharge into the bypass air flow. The condenser core geometry is a flat-tube microchannel HEX with louvred fins, mounted in an annular configuration to allow for a simple and axisymmetric integration within the bypass duct. The HEX is modelled as a porous zone to increase the computational efficiency of the CFD simulations, by replicating the expected flow resistance and heat transfer without explicitly resolving detailed geometrical HEX features. The fan is modelled using a simplifying actuator disk approach, simulating the pressure jump across the fan plane without resolving individual blade geometries. The turbofan geometry and performance are based on the LEAP-1A engine, which is representative of modern high bypass ratio (BPR) turbofan technology.

2 Literature Review

A critical aspect of the model setup is selecting a condenser topology with the appropriate aerothermal performance characteristics and compactness. The compactness is defined as the ratio of heat transfer surface area to volume and is a crucial metric for aerospace-grade HEXs. A compact HEX core is characterised by [11]

$$\beta_{\text{HEX}} \geq 700\,\text{m}^2/\text{m}^3 \tag{1}$$

and is the first requirement of the condenser. Further selection is guided by construction characteristics, with particular attention to plate-fin, tube-fin, and flat-tube HEX designs, all of which have established use in aerospace applications.

Plate-fin heat exchangers (PF-HEXs) are widely used in aircraft environmental control systems (ECS) and oil cooling systems due to their high thermal effectiveness and low weight [12], [13]. While more commonly associated with automotive applications, the tube-fin configuration has also been implemented in aerospace systems where robustness and durability are critical design considerations [9], [11].

The preferred HEX design for this research is the flat-tube heat exchanger (FT-HEX). The low-profile flat tube geometry maximises the heat transfer area on the hot fluid side while minimising obstruction to the air-side flow [11], [14]. Modern FT-HEXs often incorporate microchannels into the design, dividing the flat tubes into small parallel flow channels that significantly enhance heat transfer rates while maintaining a compact form factor.

These geometries often feature fins to increase the air side heat transfer area, which is characterised by a higher thermal resistance compared to the working fluid side. By using louvred fins, the fin structures promote flow mixing and boundary layer disruption, leading to a two- to fourfold increase in the heat transfer coefficient compared to conventional fin geometries [11]. Given these advantages, the flat-tube microchannel heat exchanger with louvred fins emerges as an optimal choice for this research due to the high compactness and thermohydraulic performance.

2.1 Porous Media Model

The porous media model (PMM) in CFD simulations can be used to analyse flow passing through porous geometries such as soil, fences and filtration devices (see Refs. [15]–[17]) without the need to model the porous medium geom-

etry, thus reducing computational time and complexity. The PMM approach has also been applied to simulate the pressure drop and temperature increase through compact HEX core geometries in aerospace applications (see Refs. [8], [9], [14]). The pressure drop through the PMM is simulated by including a momentum source term in the conservation of momentum equation, formulated as

$$\frac{\partial}{\partial t}(\rho\vec{v}) + \nabla\cdot(\rho\vec{v}\vec{v}) = -\nabla p + \nabla\cdot\bar{\tau} + \rho\vec{g} + \vec{S}_m\,. \quad (2)$$

The momentum source term is modelled using the Darcy-Forchheimer equation, an evolution of Darcy's law [18], which applies to airflows with high Reynolds numbers. The Darcy-Forchheimer equation expresses pressure gradient per unit length L as a quadratic function of airflow velocity,

$$\frac{\nabla P}{L} = \left(\frac{\mu}{K}\right) v + \left(\frac{c_F}{\sqrt{K}}\right)\rho|v|v\,, \quad (3)$$

where c_F is the inertial coefficient, K is the specific permeability of the porous zone and μ is the dynamic viscosity.

Equation 3 can be reformulated as

$$\vec{S}_m = \frac{\nabla P}{L} = \mu\mathbf{D}\vec{v} + \frac{\rho}{2}\mathbf{F}|\vec{v}|\vec{v} \quad (4)$$

where the elements of matrices **D** and **F** are adjusted to vary the pressure gradient of the flow in each flow direction. The flat tubes and fins inside the condenser constrain the airflow to travel straight through the heat exchanger core. To ensure that the flow is normal to the HEX frontal area, the flow resistance per unit length along the other flow directions is imposed to be significantly larger than that of the flow through the HEX core.

The thermal performance of the HEX in the porous zone is modelled by means of an energy source term in the energy balance equation. The energy balance can be expressed according to nomenclature introduced by Quintard [19], where the β-phase represents the fluid travelling through the σ-phase structure. Therefore, in the case of a heat exchanger, the β-phase is the airflow passing through it, while the σ-phase is the solid metal structure of the heat exchanger itself. The resulting energy equation is

$$\begin{aligned}&\frac{\partial}{\partial t}\left(\varepsilon\rho_\beta E_\beta + (1-\varepsilon)\rho_\sigma E_\sigma\right) + \nabla\cdot\left(\vec{v}\left(\rho_\beta E_\beta + p\right)\right) = \\ &\nabla\cdot\left[k_\beta\nabla T + (\bar{\tau}\cdot\vec{v})\right] + \vec{S}_e\end{aligned} \quad (5)$$

where ε is the medium porosity, defined as the volume fraction V_β/V. The heat conduction term on the right-hand side (RHS) of Equation 5 is dependent on the fluid thermal conductivity k_β.

The energy source term in Equation 5 is equivalent to the volumetric heat flux, defined according to

$$q_{\text{local}} = h_{\text{local}}\,(T_{\text{wall}} - T)\,\beta_{\text{HEX}} \quad (6)$$

where h_{local} is the local heat transfer coefficient, T_{wall} is the temperature of the HEX wall in contact with the airflow, and T is the local airflow temperature. The parameter h_{local} depends on the local flow conditions and thermal properties of the fluid according to

$$h_{\text{local}} = \frac{k_\beta\,Nu}{D_{\text{eq}}} \quad (7)$$

reformulated from the definition of the Nusselt number Nu. D_{eq} is the hydraulic diameter of the louvred fin geometry, calculated through

$$D_{\text{eq}} = \frac{4A_0}{P} \quad (8)$$

where A_0 is the cross-sectional flow area of the air conduit bounded by the louvred fins and flat tubes, while P is the wetted perimeter of the conduit. This definition is commonly used in HEX calculations to estimate the Reynolds number.

The Nusselt number Nu represents the convective to conductive heat transfer ratio and it can be expressed in the following general form [9]

$$Nu = a\,Pr^m\,Re^n_{D_{\text{eq}}} \quad (9)$$

where coefficients a, b and n are selected to approximate the thermohydraulic performance of the HEX core.

Combining Equations 6, 7 and 9, the energy source term can be expressed as

$$\vec{S_e} = q_{\text{local}} = \frac{k_\beta\,a\,Pr^m\,Re^n_{D_{\text{eq}}}\,(T_{\text{wall}} - T)\,\beta_{\text{HEX}}}{D_{\text{eq}}}\,. \quad (10)$$

Within the porous zone, the wall temperature T_{wall} is assumed constant; this assumption does not introduce significant errors as the HEX being analysed is a condenser. Additionally, the total heat exchanger length L must be much larger than the pore-scale characteristic lengths l_β and l_σ [19].

The PMM provides sufficiently accurate results provided

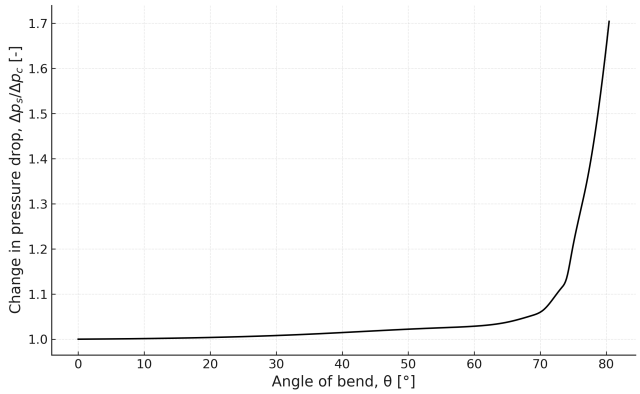

Figure 2: Effect of changing the incoming flow orientation on the airflow pressure drop through a heat exchanger. Adapted from [22].

that the model is calibrated with accurate and sufficient calibration data [9], [14], [20] while reducing computational cost and modelling time. This approach is also adaptable to different HEX geometries by adjusting porosity and resistance coefficients.

2.2 Heat Exchanger Integration

Research by Drela [21] found that the HEX positioning for a high-altitude aircraft can significantly affect the resulting drag penalty. Therefore, the placement of the condenser inside the bypass duct must be carefully selected.

A critical design parameter is the inclination of the condenser within the bypass duct. Tilting the HEX allows for increasing its frontal area without affecting the diameter of the turbofan engine nacelle. Changes to the nacelle diameter affect the engine bypass ratio, weight, drag, and fan performance, and are therefore avoided in this work. Beyond a 70-degree inclination, the air-side pressure drop through the condenser increases substantially as shown in Figure 2. The graph is based on experimental data collected by Nichols [22] obtained in an early wind tunnel setup and at a low air velocity. At the higher velocities typical of turbofan bypass flows, the sharp pressure loss escalation likely occurs at a lower inclination angle.

Based on these considerations, the inclination angle of the HEX is chosen to be 55 degrees.

The total pressure loss associated with the presence of the HEX in the bypass duct introduces a drag penalty which can be offset by converting part of the thermal energy discharged to the bypass duct air into kinetic energy. This effect was investigated by Meredith in 1935 for a piston engine aircraft [23]. Exploiting the thermal energy discharge to the bypass duct is even more critical for modern aero engine concepts. Notably, Kaiser et al. [7] analysed an ultra-high bypass ratio (UHBPR) Water-Enhanced Turbofan (WET) employing a Cheng cycle – a combination of a Brayton and Rankine cycle – for reduction of engine contrails, $\mathrm{CO_2}$ and $\mathrm{NO_x}$ emissions. This engine concept features an inclined condenser placed in the bypass duct that extracts water from the exhaust gas, condensing it using the bypass air as a heat sink. The study claims that the thermal energy discharged to the bypass duct could be used to accelerate the airflow through a nozzle and completely compensate for the additional drag caused by the HEX pressure loss. The potential for HEX drag recovery is promising, although it should be noted that the nacelle length had to be increased by 40% in the study by Kaiser et al. [7] to incorporate the condenser while retaining enough length for the bypass nozzle. Compact and efficient packaging will thus be key in avoiding changes to the external turbofan geometry.

To link the heat dissipated by a ducted HEX to the resulting drag of the HEX core, Drela [21] devised a relation that takes into account the Meredith effect, expressed as

$$D_{\text{HEXcore}}\, V_\infty \simeq \frac{\dot{m}}{2} V_\infty^2 \frac{\Delta p_{\text{HEX}}}{q_1} \left(\frac{V_1}{V_\infty}\right)^2 - \dot{H}\frac{\gamma-1}{2} M_\infty^2 \,. \tag{11}$$

In this equation, $\dot{H}$ is the heat rejection rate, $\dot{m}$ is the air mass flow into the heat exchanger, and subscript 1 denotes conditions directly in front of the heat exchanger. Equation 11 highlights the benefit of slowing down the flow in front of the heat exchanger from V_∞ to a low V_1. If $\dot{H}$ is made as large as possible, it is even possible to obtain a negative value for $D_{\text{HEXcore}}\, V_\infty$ as postulated by Meredith. Equation 11 suggests that the optimiser will seek to adjust the duct wall geometry to slow the flow from V_∞ to a low V_1 and/or to maximise the heat duty.

2.3 Actuator Disk Model

The actuator disk (AD) method is used to model the fan and OGVs as permeable disks that exert forces on the air passing through without needing to resolve the exact geometry of the blades or vanes. The AD method involves adding momentum to the flow through source terms rather than through complex 3D flow interactions. A fan modelled as an AD represents an idealised configuration with an infinite number of blades and

without unsteady flow discontinuities. This modelling approach is appropriate for time-averaged flow representations, as required in RANS simulations of turbofans. Originally introduced by Froude in 1920 for aviation propellers, actuator disk theory has since been extensively refined.

There are two approaches for modelling a fan as an AD: adding source terms to the AD region or imposing a pressure jump as a boundary condition to the flow. Rajagopalan and Fanucci [24] first implemented the former method to model wind turbines, modelling the volume occupied by the spinning blades as a porous cylinder in which these momentum source terms are applied. The method can be used for both a disk of one control volume width and a wider region, allowing the entire rotor width to be represented by an actuator disk and spreading the pressure rise over this volume. This more accurately portrays the actual behaviour of a fan and is therefore preferred over a pressure jump boundary condition, which is easier to implement but may lead to strong discontinuities in the flow [25]. The source term method is also more robust than imposing a pressure jump when introducing a swirl component to the airflow [25].

The momentum source terms can be calculated in different ways. Research from Spinner et al. [26] and Baratchi et al. [27] use Blade Element Momentum theory, in which a propeller or fan blade is broken down into a finite number of airfoils stacked together. The inputs for this model are the airfoil geometries along several sections of the fan blade. For each airfoil section, the lift and drag coefficients C_L and C_D are computed over a range of angles of attack α. These forces are integrated along circumferential sections of the fan blade to produce a force distribution, which can then, in turn, be converted to a momentum source term. This approach shows good agreement with results from higher fidelity URANS simulations; however, it requires detailed 3D geometrical information of the fan and OGV, which is unavailable to the author.

A second AD method involves using a custom thrust loading profile that varies along the blade radial direction, providing a more holistic method of modelling the fan and OGVs. This method is used by Stich et al. [25] to model the fan of the NASA Glenn Ultra High Bypass Drive Rig, a 1:5 scale turbofan model. Two axial and tangential loading profiles are considered: the first assumes a radially uniform thrust distribution, corresponding to the classical actuator disk approximation. The second adopts the circulation distribution derived by Goldstein and Prandtl [28], which more accurately represents finite-blade effects. This latter profile, commonly referred to as the Goldstein loading, is depicted in Figure 3. This circulation distribution can be converted into a thrust distribution for a typical propeller, which minimises the energy lost in a propeller slipstream. Lastly, custom load profiles generated from detailed URANS results are inputs for the simplified actuator disk method. Stich et al. [25] showed that all three methods can predict the overall mass flow rate, total pressure ratio, and total temperature ratio to within 1% accuracy. However, the velocity profile at the OGV exit differs slightly from experimental results, which in the case of a CC-TF engine would have a direct effect on the heat transfer occurring in the condenser.

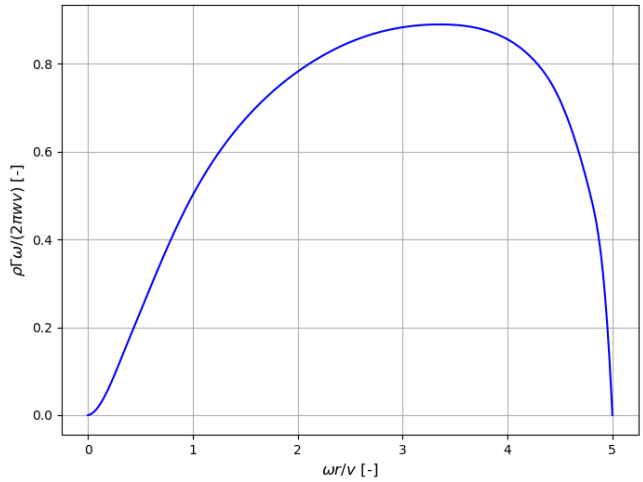

Figure 3: The Goldstein load distribution, showing the non-dimensional circulation as a function of the dimensionless rotational velocity ratio for a 4-bladed propeller. Adapted from [28]

A fundamental limitation of using an axisymmetric RANS actuator disk model is the inability to capture the effects of geometrical asymmetries on the circumferential distribution of thrust and flow properties. Examples of these engine asymmetries are the engine pylon, structural struts downstream of the OGVs, the presence of the wing, and the shape of the inlet lip. The asymmetries introduce local flow distortions by partially obstructing the bypass duct.

Kodama and Nagano [29] investigated the influence of such components on circumferential pressure variations and demonstrated that their effects can be incorporated into an actuator disk model by modifying the loading through the

OGVs, thereby enabling reduced-order simulations while preserving key flow features. Similarly, previous studies have quantified the aerodynamic penalties associated with engine integration using CFD simulations, particularly in terms of flow non-uniformity and drag increments (see Refs. [30]–[32]).

This work assumes a negligible effect of these asymmetries on the flow solution inside the bypass duct and the duct optimisation process, since they primarily affect the external nacelle shape and the placement of local flow control devices such as vortex generators.

2.4 Optimisation Methods

The optimisation algorithms used for optimising duct geometries can be divided into two categories: derivative-free methods and gradient-based methods. Among the derivative-free methods, genetic algorithms (GAs) are a popular choice and are based on the principles of natural selection and evolution. These algorithms evaluate a population of potential solutions and employ processes like mutation, crossover, and selection to evolve towards an optimal design. In the context of turbofan duct shaping, Patrao et al. [10] and Clemen et al. [33] both chose to employ the Natural Search Genetic Algorithm NSGA-II to optimise turbofan duct and OGV geometries, with the former using a population size of 100 individuals over 100 different generations and the latter using 80 individuals over 60 generations to improve the OGV shape. Genetic algorithms help explore complex design spaces and are good at avoiding local optima, but they come with a relatively high computational cost.

Another approach to derivative-free optimisation is the Design of Experiments (DoE) method, which systematically samples the design space to explore relationships between design variables and performance metrics. Bajimaya et al. [34] employed a full factorial DoE approach to study the integration of a ducted HEX within the bypass duct while varying both the length and height of the HEX. A DoE is particularly well-suited for initial design exploration and allows researchers to understand the entire design space. However, the method becomes computationally expensive when applied to high-dimensional problems.

Gradient-based methods utilise derivative information to locate the optimal solutions, therefore, they are often employed in problems with smooth and differentiable objective functions. Witte and Bode [35] use a gradient-based method to optimise a simplified bypass duct geometry to integrate heat transfer structures that contribute to aerodynamic efficiency. Employing a multi-objective optimisation routine allowed Witte and Bode [35] to construct a 2D Pareto front of solutions featuring minimum pressure drop and maximum heat transfer. Gradient-based optimisations generally converge faster than derivative-free approaches and are widely used for aerodynamic and thermal optimisation [36].

The chosen parametrisation method for the bypass duct geometry can impact the optimisation solution, computational time and flexibility. One approach of geometric parametrisation involves using control points to define smooth Bézier curves, cubic splines, or B-splines, allowing automatic geometry updates by adjusting point coordinates. Patrao et al. [10] use Bézier curves and control points for HEX and duct parametrisation, while Clemen et al. [33] use five axially fixed points varying only radially, halving variable count and simplifying geometry definition. Keeping the bypass duct inlet and exit positions fixed avoids changes to turbofan length, preventing extensive engine redesign. The cubic splines generated in Ansys are preferred over B-splines or Bézier curves, ensuring the curves pass through control points and simplifying constraint implementation.

An alternative parametrisation method is Class Shape Transformation (CST), which is widely used in aerospace engineering to define aerodynamic surfaces. The CST method combines a class function $C(x)$, which sets general geometric features, with a shape function $S(x)$, which refines finer details:

$$y(x) = C(x)\, S(x) + x\, \Delta y\,. \tag{12}$$

CST has been successfully applied to bypass duct nozzle design and optimisation [32] and can also be integrated with other methods for enhanced control. Namely, Christie et al. [37] combined CST with the PARSEC method [38], creating the iCST method for greater aerodynamic flexibility. Bajimaya et al. [34] demonstrated its suitability for turbofan bypass duct design.

While CST methods provide more refined geometrical control, they do not necessarily reduce the number of variables compared to a method employing axially fixed control points. Given the simplicity of implementing a control point method into ANSYS Fluent, it is preferred for initial optimisation studies.

3 Methodology

3.1 Computational Domain

To account for compressible flow effects, the upstream boundary condition (BC) is defined as a pressure inlet and the downstream BC as a pressure outlet. This approach improves numerical stability and solution accuracy in comparison to a velocity inlet specification, particularly when shock waves are present [39]. The turbofan axis and the far-field wall form the upper and lower boundaries, and the flow into the engine core is set through a mass flow outlet BC.

Kaplan [40] used the definition of the engine length L as a reference and modelled a domain spanning $10L$ upstream and $12.5L$ downstream, with a conical far-field boundary tapering from $10L$ upstream to $12.5L$ downstream. Other detailed simulations, such as that performed by Heidebrecht et al. [41] focus on the nacelle diameter D_n and model between $30D_n$ and $45D_n$ around the nacelle. Smaller domains are also reported in the literature, such as in Mund [42], which suggests that a domain height of 4-5.5D_n is sufficient when only analysing cruise conditions. Note that these measurements consider the entire domain; therefore, in a 2D axisymmetric setup, only half of this domain is modelled in ANSYS Fluent. Mund [42] also demonstrated that upstream domain modelling has a relatively small impact on pressure recovery at the engine intake: increasing the upstream modelled domain from $4D_n$ to 10 D_n only increases pressure recovery by 0.05%.

Ultimately, the total domain height chosen for this study is $6.5D_n$, as this height did not yield any noticeable pressure fluctuations along the far-field wall. A length of $5.2D_n$ in front of the turbofan engine is considered in the CFD domain to fully capture the pre-diffusion of the airflow as it enters the turbofan inlet.

The CFD computational domain size downstream of the turbofan engine can have a slight effect on the propulsive efficiency. Namely, Zimmermann [43] demonstrated that the thrust coefficient of the engine could be improved by up to 1% by carefully tailoring the velocity distribution at the bypass duct outlet, due to the downstream interaction with the external nacelle flow and core exhaust flow. Capturing these aerodynamic gains would require simulating the core exhaust temperature and pressure distributions, complicating the CFD model and substantially increasing the domain size. Due to the limited performance gains involved, the downstream effects are deemed out of the scope of this research. Other works studying turbofan bypass duct flow, such as that by Zennaro [44], similarly omit downstream domain modelling.

3.2 Generation of the Turbofan Geometry

The baseline geometry of the LEAP-1A turbofan engine is first constructed using ANSYS DesignModeler. Modifications are then applied to the bypass duct to enable integration of the condenser unit at an inclination angle of 55 degrees. Specifically, the local duct wall is reoriented to align with the expected flow direction through the heat exchanger core, and the surrounding duct contours are shaped to maintain smooth curvature transitions. This adjustment is made to promote flow attachment along the duct surfaces and to maintain a high mesh quality, particularly in regions of strong curvature and flow acceleration near the HEX inlet and outlet.

To prevent airflow stalling at high angles of attack, the bottom lip of the inlet is typically shorter and rounder than the top lip. However, due to the axisymmetric constraints of this study and a focus on cruise conditions, these anti-stall features are neglected and instead a constant inlet shape is assumed, based on the shape at the top of the LEAP-1A engine nacelle. Kaplan [40] employed a NACA 1-series airfoil profile to approximate the external surface of the turbofan inlet, producing sufficiently accurate results for the supersonic flow behaviour observed over the nacelle exterior surface. The NACA 1-series profile is also employed in this research to generate the turbofan inlet geometry.

Figure 4 displays the resulting turbofan geometry modelled in Ansys Fluent. The station numbers are also displayed; those prefixed with 1 are part of the main intake and bypass duct, whereas station 21 is the inlet of the core flow.

3.3 Grid Generation

Turbofan engine CFD simulations employ a range meshing techniques to balance accuracy and computational efficiency. A commonly adopted approach uses structured quadrilateral grids, with the highest mesh density concentrated near the air intake, actuator disk and nozzle outlet (see Refs. [26], [41], [42], [45]). Other studies adopt an unstructured mesh, incorporating triangular or tetrahedral elements in the core flow regions, combined with structured quadrilateral elements in the near-wall boundary layer (see Refs. [10], [40], [46]).

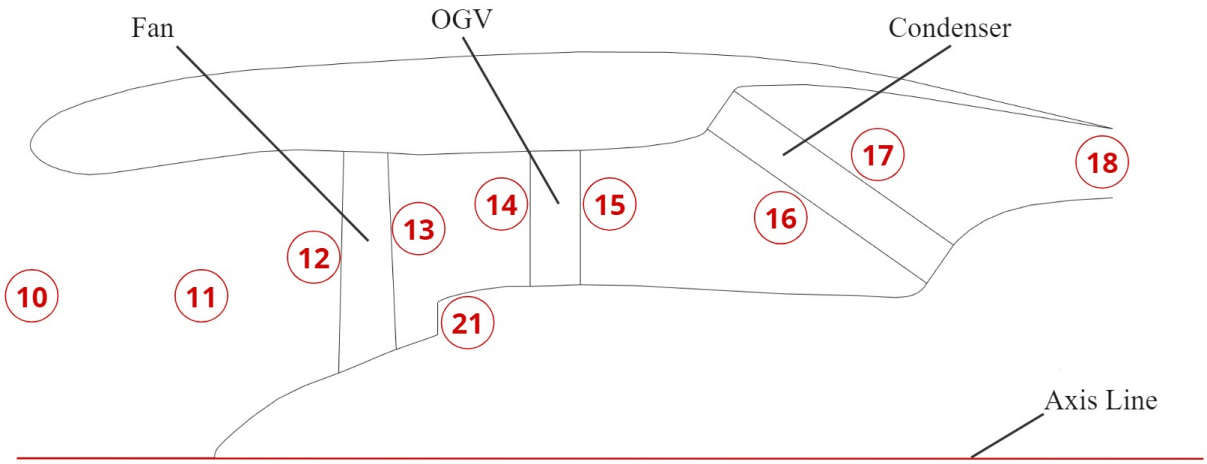

Figure 4: The modelled geometry of the CC-TF in ANSYS Fluent, with station numbers.

Mesh robustness is particularly critical for duct optimisation studies. Patrao et al. [10] optimised the duct shape for a turbofan intercooler and recuperator, utilising an unstructured mesh comprising quadrilateral and triangular elements. This approach can ensure sufficient mesh element quality even when the duct geometry is adjusted. However, this flexibility comes with the trade-off of increased computational time between iterations.

In this study, a hybrid meshing strategy is adopted, combining elements of both structured and unstructured meshing. An unstructured mesh, comprising a combination of triangular and quadrilateral elements, is applied around the inlet lip, the core flow inlet, and the condenser inlet and outlet. Outside these areas, particularly in the upstream domain, the mesh transitions smoothly into a structured layout, as illustrated in Figures 5 and 6.

A uniform inflation layer is applied to all solid walls except those bounding the HEX porous zone. In this zone, wall friction effects are captured through the momentum source terms rather than near-wall meshing. The inflation layer consists of 34 layers with a growth rate of 1.2 and a transition ratio of 1.0 for a smooth gradation into the background mesh. This layering is particularly visible along the nacelle surface shown in Figure 5.

A mesh convergence study determines the element size and total element count for the optimisation process. The mesh convergence plots are presented with the other CFD mesh verification results in Subsection 4.1.

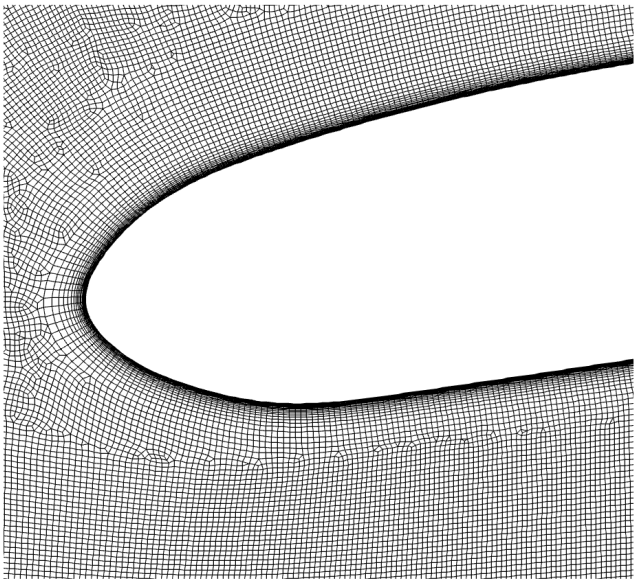

Figure 5: The generated mesh around the inlet lip of the turbofan.

3.4 Porous Media Model Setup and Calibration

The porous media model requires the specification of the HEX porosity ε, which primarily determines the velocity inside the porous zone as well as the associated flow deceleration and acceleration at the inlet and outlet interfaces. For this study, a porosity value of 0.77 is selected, reflecting typical values for flat tube microchannel louvred fin heat exchangers. The porosity value is based on the research by Krempus [47] for a condenser of a CC-TF engine concept optimised for minimum fuel consumption.

To calibrate the pressure drop characteristics of the porous

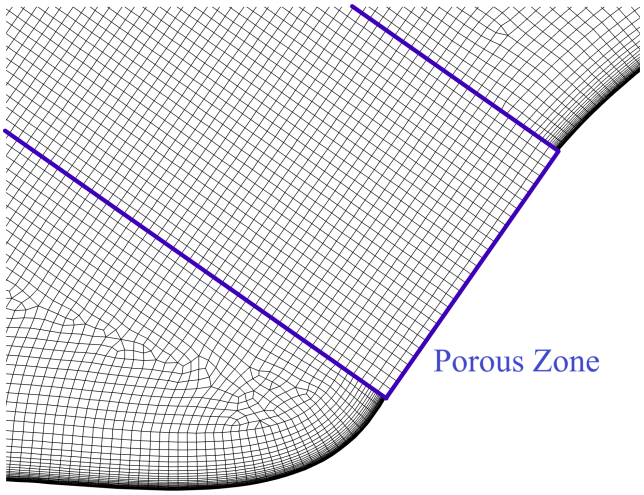

Figure 6: The generated mesh around the condenser porous zone.

media, the matrices $\mathbf{D}$ and $\mathbf{F}$ from the momentum source term in Equation 4 are determined using HeXaCode, an in-house developed tool designed for the rating and sizing of heat exchangers which has been successfully verified through comparison with commercial code and has been employed in prior research [48]. The rating function implemented in HeXaCode estimates the condenser outlet temperature and pressure for both fluids, given a fixed heat exchanger area and geometry. The rating of the HEX at varying mass flow rate, inlet temperature and inlet pressure is performed to generate a quadratic calibrated pressure drop relation, consisting of the viscous resistance term and inertial resistance term

$$\vec{S}_m = C_1 \vec{v} + C_2 \frac{\rho}{2} |\vec{v}| \vec{v}. \tag{13}$$

and expressed in terms of viscous coefficient C_1 and inertial coefficient C_2. In ANSYS Fluent, the viscous term requires the inverse absolute permeability as input, expressed in terms of C_1 as

$$\frac{1}{K} = \frac{C_1}{\mu} \tag{14}$$

ANSYS Fluent requires the coefficients to be designated in 3 directional vectors for an axisymmetric simulation, where the direction-1 vector is the direction normal to the HEX frontal area. For this direction, the coefficients determined by HeXaCode are used, while in the remaining two directions, the resistance coefficients are multiplied by a factor of 1000 to simulate the presence of flat tubes and fins within the condenser core.

Table 1 lists the value of the momentum source term parameters used to approximate the presence of the CC-TF condenser.

Parameter	**Value**	**Unit**
Porosity ε	0.77	-
Viscous Resistance $\frac{C_1}{\mu}$	9,798,361	m^{-2}
Inertial Resistance C_2	70.86	m^{-1}

Table 1: The momentum source term parameters inputted into Ansys Fluent.

The energy source term is inputted in ANSYS Fluent according to Equation 10. Table 2 summarises the inputted parameters to set up the energy source terms. The parameters β_{HEX}, D_{eq} and T_{wall} are calculated using the HEX sizing function of HeXaCode for the condenser of the CC-TF analysed by Krempus et al. [47]. The wall temperature T_{wall} is calculated as a heat transfer area weighted average across the HEX. The parameters a and n from the Prandtl number relation in Equation 9 are also calibrated through the HeXaCode sizing function, while the parameter n is set to 0.33, a commonly used value found in the research by Sieder and Tate [49].

Parameter	**Value**	**Unit**
D_{eq}	0.00289064	m
a	0.439774	-
m	0.33	-
n	0.522314	-
T_{wall}	377.9	K
β_{HEX}	1066	m^{-1}

Table 2: The energy source term parameters inputted into Ansys Fluent.

The local thermophysical properties of the airflow are estimated through polynomial equations as a function of local air temperature. The dynamic viscosity μ varies locally according to Sutherland's law [50]. The specific heat capacity at constant pressure follows the quadratic relation

$$C_p(T) = 1024.201 - 0.17345\,T + 3.7 \cdot 10^{-4}\,T^2 \tag{15}$$

while the air thermal conductivity follows the relation

$$k_\beta(T) = 7.68049 \cdot 10^{-4} + 9.56909 \cdot 10^{-5}\,T - 3.49 \cdot 10^{8}\,T^2\,. \tag{16}$$

The polynomial coefficients have been determined by van Dongen [6] for a condenser placed inside an aircraft ram air duct at cruise altitude and were determined using the soft-

ware CoolProp. With these properties specified, the Prandtl number is then calculated through

$$Pr = \frac{\mu C_p}{k_\beta}. \tag{17}$$

The air density calculations follow the ideal gas law.

3.5 Actuator Disk Models

The 2D axisymmetric CFD domain is divided into zones, with specific zones designated to represent the fan and OGVs. Within these regions, axial and tangential momentum sources are applied to simulate the aerodynamic effects of these components. Instead of concentrating the momentum sources within a disk of single-cell thickness, they are distributed across the entire thickness of the fan and OGVs which causes a more uniform pressure rise. This pressure rise replicates the expected flow behaviour inside a turbofan engine [25].

The radial distribution of thrust in the fan is defined to approximate the Goldstein loading, with a peak occurring near 70% of the blade span. However, direct implementation of the original Goldstein profile introduces numerical instabilities near the hub and casing ($r/R \to 0$ and $r/R \to 1$), where the momentum source terms approach zero. This results in large velocity gradients, local flow reversal and the formation of vortices, leading to departures from the results of the performance simulation tool employed by Mund and Pilidis [51] and the detailed URANS results obtained by Spinner et al. [26]. To mitigate these effects and improve agreement with high-fidelity data, the thrust profile is modified to increase the thrust contribution near the inner and outer radial boundaries. A comparison between the modified and original Goldstein distributions is presented in Figure 7. These adjustments lead to improved numerical stability and more accurate reproduction of the total pressure field downstream of the fan.

The thrust distribution is implemented in ANSYS Fluent as a fourth-order polynomial function of the radial position. The thrust distribution is calibrated to produce a total net thrust of 50,000 N, typical for a short-to-medium-range aircraft.

A factor limiting the flow solution accuracy near the turbofan casing wall is that the AD model does not account for supersonic flow and 3D effects near the blade tips. Spinner et al. [26] compared an AD methodology to a 3D URANS simulation of the fan and OGVs, revealing that results from the AD method showed a deviation in total pressure and flow swirl angle at the blade tips when compared to the URANS results. The authors partially attributed this difference to the 3D flow effects in the URANS simulations.

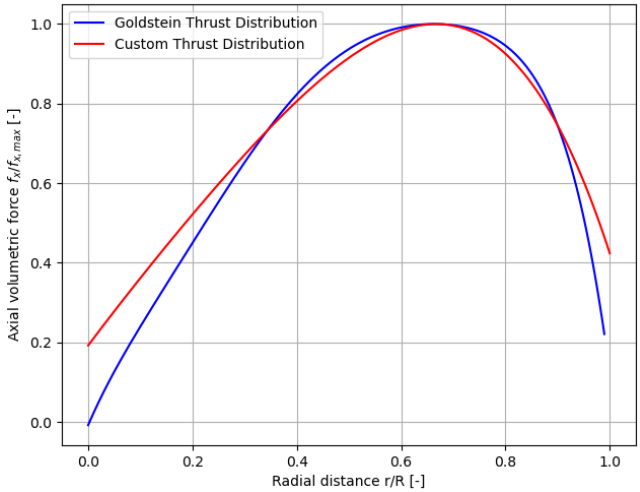

Figure 7: Comparison of a Goldstein thrust distribution to the custom function inputted into Ansys Fluent, as a function of radial distance.

The limited accuracy of the AD model in predicting tip effects could also impact the heat transfer in a downstream HEX, however this has not been previously investigated. Therefore, the heat transfer near the nacelle and hub walls must be critically analysed when observing the CFD results.

3.6 Turbulence Model, Boundary Conditions and Numerical Setup

For turbofan and porous zone CFD simulations, the RANS turbulence models most commonly employed are the k-ω Shear Stress Transport (SST), the k-ε, and the Spalart-Allmaras (S-A) models. The S-A model is a simpler, one-equation model, making it a computationally efficient option, particularly in high-speed aerodynamic applications. Unlike two-equation models, the S-A model does not require an extremely fine near-wall mesh, as it incorporates a wall-damping function that allows for moderate $y+$ values. However, while this reduces the computational cost, the S-A model is less accurate for flows with strong separation or adverse pressure gradients.

Ahlinder [52] recommends using a two-equation turbulence model to balance flow resolution within the porous

zone and the remainder of the CFD domain. Consequently, the k-ω SST turbulence model is selected, combining the strengths of both k-ε and k-ω models. The k-ε model performs well in freestream regions, while the k-ω model is superior in near-wall turbulence resolution. The SST formulation improves accuracy by blending these two models using a cross-diffusion term. The turbulence model only requires the input of constants, which have been determined by Menter [53] [54].

The boundary conditions are selected to replicate the cruise conditions for the A320 aircraft family. Table 3 lists the cruise parameters and resulting boundary conditions implemented in the CFD simulation. A total pressure inlet is specified at the intake, while a static pressure outlet is applied at the bypass duct exit. Additionally, a mass flux outlet is defined at station 21, to reproduce the expected air mass flow rate to the engine core.

All walls are set up with a no-slip boundary condition except those inside the porous media model, where the momentum source terms simulate the entire flow resistance. A turbulence intensity of 5% at the domain inlet strikes a compromise between the low-turbulence flow around the nacelle and the high-turbulence flow inside the turbofan engine.

Parameter	Value	Unit
Cruise altitude	10000	m
Cruise Mach	0.78	-
Inlet total pressure	39516	Pa
Outlet static pressure	26436	Pa
Core mass flux condition	35.67	kg/(m^2 s)
Far-field static pressure	26436	Pa

Table 3: The cruise conditions of the A320 aircraft and the resulting imposed boundary conditions in Ansys Fluent.

A pressure-based solver is employed for this study because it accounts for the increase in airflow velocity inside the porous zone resulting from the local reduction in flow area [39]. Accurately resolving the velocity field in the condenser is essential for the reliable prediction of both the simulated heat transfer and pressure drop.

The CFD simulations employ a coupled pressure-velocity algorithm as it provides a robust method for single-phase steady flow simulations and converges faster than segregated algorithms. Second-order spatial discretisation methods limit the effect of numerical diffusion on the accuracy of the results. Convergence is considered achieved when all residuals reach below 10^{-4} except the energy residual, with a stricter criterion of 10^{-6} applied to the energy equation. These convergence criteria keep the simulations computationally efficient with satisfactory solution accuracy for an initial duct optimisation study.

3.7 Verification and Validation

The verification procedure starts with a sensitivity study of the generated grid mesh. The grid is progressively refined with a refinement ratio of around 1.5, with a mesh size ranging from 250,000 to 1,650,000 elements. The parameters analysed in the grid convergence study are the total temperature change across the condenser $\Delta T_{t,\mathrm{HEX}}$, total pressure change across the condenser $\Delta p_{t,\mathrm{HEX}}$, and net thrust of the turbofan cold air stream. These parameters are selected for their direct relevance to the thermal and aerodynamic performance of the system: a reliable HEX heat transfer and pressure drop model requires sufficient grid independence, while the optimisation procedure depends on accurate net thrust calculations.

Next, a turbulent boundary layer (TBL) plot is generated to compare the y^+ values to the U^+ values near the walls of the CFD domain. When $y^+ < 5$, the flow is in the viscous sublayer with a characteristic linear velocity profile, $U^+ = y^+$. In the buffer layer, $5 < y^+ < 30$, both viscous and turbulent forces affect the flow behaviour, and as such, the velocity profile begins to deviate from its linear behaviour. Above $y^+ = 30$, the flow is dominated by turbulent behaviour, and the non-dimensional flow velocity should follow a logarithmic relation given by

$$U^+ = \frac{1}{k} ln(y^+) + B \tag{18}$$

where $k = 0.4187$ and $B = 5.2$. If the generated TBL plot agrees with this expected behaviour, the CFD simulation is able to resolve the near-wall flow well and the turbulence model predicts velocity gradients realistically.

In a wall-resolving turbulence model, like the k-ω SST model, the value of y^+ should always be smaller than 1 at the walls. It is critical to ensure $y^+ < 1$ even in areas where a large velocity change occurs, such as at the turbofan air intake and bypass outlet nozzle. Therefore, the y^+ values are independently verified along all walls to ensure proper

turbulence modelling.

A simple verification of the porous zone setup is performed by observing the pressure losses, flow velocity and heat transfer in a straight duct section. The velocity should increase by the inverse of the porosity $1/\varepsilon$ when only the porosity is activated without source terms. Activating the momentum source terms should result in a quasi-linear decrease in pressure as the flow passes through the HEX, as observed by van Dongen [6]. If the energy source terms are correctly implemented, the airflow temperature should not exceed the HEX wall temperature T_{wall} and the change in temperature should also follow observations made by van Dongen [6].

The final verification procedure compares the fan and OGV AD performance to results obtained in previous turbofan AD studies. Namely, the total pressure distribution at station 13, directly after the fan, can be compared to results from Spinner et al. [26] and Mund and Pilidis [51]. The tangential velocities induced by the fan and OGV are evaluated through the measured swirl angle at station 15, after the OGVs, and then compared against results from the research of Stich et al. [25].

The external aerodynamics, particularly around the nacelle and inlet lip, can be compared against contour data trends from the high bypass ratio turbofan engine simulated in the work of Savelyev et al. [55]. Correct inlet flow behaviour is crucial for determining an accurate mass flow and pressure distribution at the fan and bypass duct.

Partial validation of the fan performance is performed through comparison with experimental data collected by Hughes [56] from NASA's UHB Drive Rig for a high bypass ratio turbofan. The data gathered relates the fan speed as a percentage of maximum rpm to the corrected mass flow rate, which in turn can be used to derive the fan total pressure ratio $p_{t,f}/p_{t,0}$. The Ansys Fluent results obtained in this research should be comparable to those found by Hughes [56] for a typical cruise thrust setting.

The fourth-order thrust distribution polynomial coefficients of the AD model are also adjusted to observe how sensitive the flow prediction quality is to any changes in the thrust distribution. This helps gain an understanding of the robustness of this AD method.

3.8 Optimisation setup

The optimisation process permits geometric modifications to the bypass duct walls both upstream and downstream of the HEX. Both the upper and lower walls between the OGVs and HEX are allowed to deform, while in the bypass duct nozzle section only the lower wall is permitted to vary. This restriction was introduced based on preliminary studies, which showed limited effect of the upper wall shape on the aerodynamic results.

The duct shape is controlled by adjusting the y-coordinates of a set of control points that define the duct wall cubic spline profiles. Each control point is constrained within individually defined upper and lower bounds based on estimated clearances and the spatial positioning of the surrounding components in the turbofan engine. The boundaries are primarily between 30 and 50mm, providing a relatively narrow range of variation for the ducts. This helps avoid diverging CFD results and allows the current turbofan outer dimensions to remain the same. However, this narrow range limits the maximum net thrust increase the optimiser is able to achieve.

In addition to net thrust, the heat duty of the condenser, the bypass nozzle outlet velocity, and the flow uniformity index at the HEX outlet are evaluated for both the initial and optimised bypass duct configurations. While these parameters are not objective functions in the optimisation process, they provide insight into the thermal and aerodynamic performance of the ducted HEX. Their comparison can help support broader conclusions on the optimisation outcome and overall system-level performance. The HEX flow uniformity index is defined according to the mass-weighted average of the airflow velocity at the HEX inlet as [39]

$$\gamma_m = 1 - \frac{\sum_{i=1}^{n} \left[\left(\left| \phi_i - \bar{\phi}_m \right| \right) \left(\left| \rho_i \vec{V}_i \cdot \vec{A}_i \right| \right) \right]}{2 \left| \bar{\phi}_m \right| \sum_{i=1}^{n} \left[\left| \rho_i \vec{v}_i \cdot \vec{A}_i \right| \right]} \tag{19}$$

where ϕ is the parameter in consideration spanning across n elements and $\bar{\phi}_m$ is its mass-averaged value according to

$$\bar{\phi}_m = \frac{\sum_{i=1}^{n} \left[\phi_i \left(\left| \rho_i \vec{v}_i \cdot \vec{A}_i \right| \right) \right]}{\sum_{i=1}^{n} \left[\left| \rho_i \vec{v}_i \cdot \vec{A}_i \right| \right]} . \tag{20}$$

The optimisation routine selected for this analysis is the Adaptive-Single Objective (ASO) method, a hybrid of the gradient-based and Design of Experiments (DoE) approach.

It first employs an Optimal Space-Filling (OSF) DoE to gather an initial sample of CFD results, from which the optimiser constructs a Kriging response surface [39]. The gradient-based MISQP optimiser is run on this response surface, generating three candidates with the highest net thrust. If these candidates are not global optimum values, they are verified through simulations before being fed back into the response surface as refinement points. If the optimiser determines the candidates to be unstable, a DoE is performed again but with a reduced domain around the potential candidates, keeping results from the previous DoE analysis. This process continues until the global optimum candidates are stable and within the convergence tolerance, at which point the simulation ends. Figure 8 illustrates a flow diagram of the optimisation process.

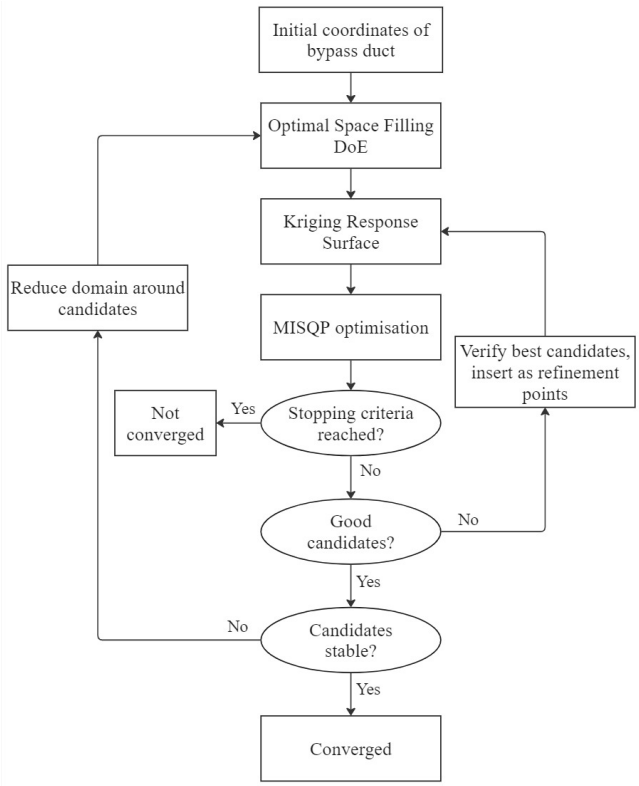

Figure 8: A flow diagram of the Adaptive Single-Objective optimisation scheme. Adapted from [39].

For this optimisation, the OSF DoE runs 66 simulations to construct the Kriging response surface. A 220 iteration limit is selected before the process terminates, at which point the three best candidates are presented. A convergence tolerance of 0.1% determines the stopping criterion of the optimisation.

4 Results

4.1 Verification and Validation of the Models

Firstly, a grid convergence study is performed to measure the net thrust, total temperature difference across the HEX and total pressure difference across the HEX. Figure 9 plots the variation in net thrust, HEX total temperature change and HEX total pressure change as a function of the grid mesh size. The total temperature rise varies by approximately 1.4% between the coarsest and finest meshes, while the total pressure drop changes by only 0.11%. This indicates that the net thrust is more sensitive to an increase in thermal performance than to an increase in pressure losses. As a result, the net thrust increases by 0.49% with mesh refinement.

A clear asymptotic flattening of all three parameter trends is observed for meshes with 500,000 cells and above, suggesting that mesh independence is largely achieved beyond this point. Therefore, the 500,000-cell mesh is selected for detailed CFD simulations and subsequent verification and validation. However, to reduce computational cost during the optimisation process, a coarser mesh with 350,000 cells is used. This provides a significant reduction in simulation time, while maintaining result deviations within an acceptable tolerance compared to the finest mesh.

Figure 10 presents the TBL diagram at station 14, with the non-dimensional velocity profile U^+ as a function of y^+, assessing whether the turbulence model captures the boundary layer flow with sufficient accuracy and resolution. Within the viscous sublayer where $y^+ < 5$, the Fluent solution shows good agreement with the viscous sublayer law, $U^+ = y^+$. In the Log-law region, where $30 < y^+ < 300$, the solution in ANSYS Fluent approaches the logarithmic relation outlined in Equation 18, with minor deviation from the law above $y^+ = 300$. In the buffer region $5 < y^+ < 30$, the flow velocity deviates from the theoretical laws, agreeing with the observations made in previous research investigating turbulent boundary layer flow [57]–[59].

The results align well with theoretical predictions, indicating that the inflation layer mesh around the turbofan walls has an adequate refinement to capture high-Reynolds-number boundary layer behaviour. Further refinement would provide diminishing returns while significantly increasing computational cost.

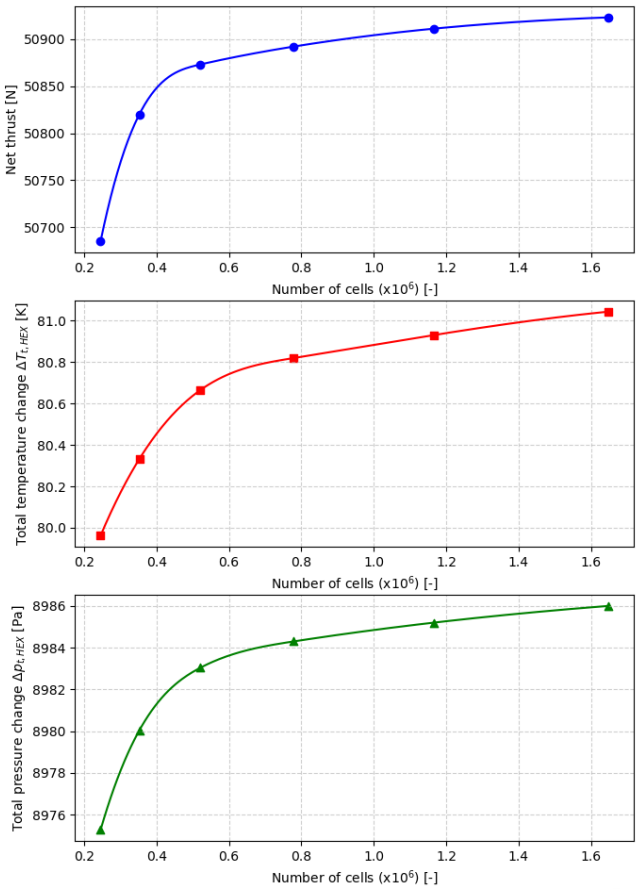

Figure 9: Results of grid convergence study, illustrating the variation in net thrust, HEX total temperature difference and HEX total pressure difference with a varying grid size.

Figure 11 plots the y^+ value along the length of the bypass duct nozzle wall between stations 17 and 18, revealing that y^+ remains below 1 even throughout the region with the highest velocity gradients. At the beginning of the nozzle, the airflow has just exited the porous zone and encounters an abrupt velocity gradient, resulting in the initial y^+ spike. However, the remaining nozzle section shows a gradual increase in y^+ and confirms that the mesh size at the wall is appropriate.

The CFD simulations were also performed using the k-ε and Spalart-Allmaras turbulence models to compare the net thrust calculations with the k-ω SST results. The k-ε simulations showed a 1.63% reduction in net thrust on average, while the Spalart-Allmaras thrust results deviated by only 0.10% from the k-ω SST simulations. These results are consistent with expectations: the k-ϵ model is known to perform less accurately in flows with adverse pressure gradients, which are present in the bypass duct and can lead to under-

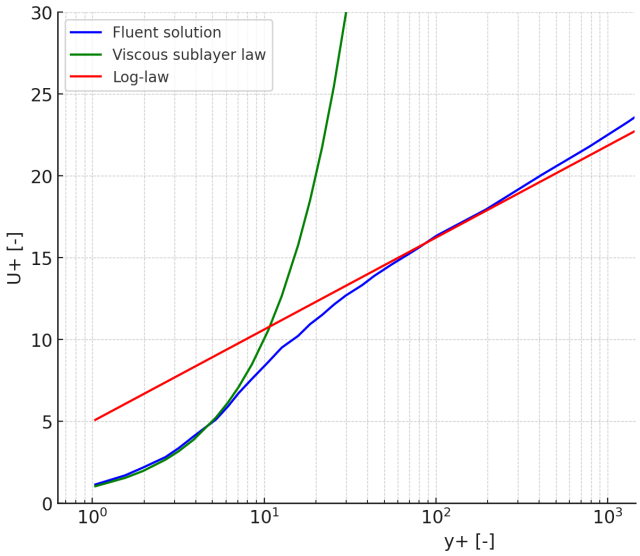

Figure 10: The turbulent boundary layer (TBL) diagram of the Ansys Fluent solution, with U^+ plotted as a function of y^+ and a comparison with pre-defined laws for the viscous sublayer and logarithmic regions.

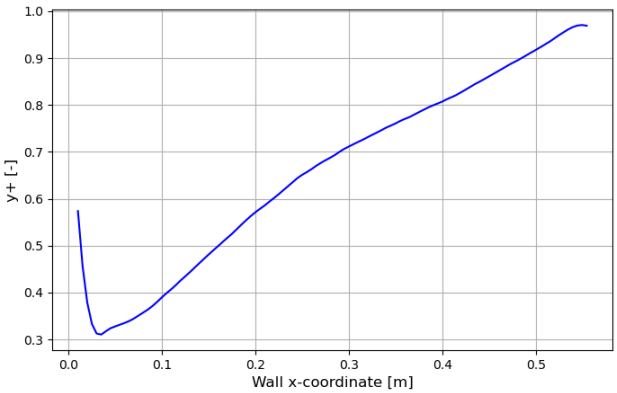

Figure 11: Plot of the y^+ values along the length of the bypass duct nozzle wall, between stations 17 and 18.

prediction of wall shear and separation effects.

In contrast, the S-A model is designed for wall-bounded flows and can provide reliable near-wall flow predictions even under adverse pressure gradients [39]. Additionally, simulations of the axisymmetric CC-TF employing the S-A model converge approximately 25% faster than simulations using the k-ω SST model, due to its simpler, single-equation formulation. While this study does not explicitly assess the influence of turbulence model on the flow conditions in the porous zone, the small deviation in thrust and reduced computational cost suggest that the S-A model could be a suitable alternative for future studies, particularly optimisation-based workflows.

To verify the correct implementation of the porous zone in the CFD setup, a simplified straight test section with slip walls is used for calibration. The porosity, momentum source terms, and energy source terms are introduced in separate stages to isolate their effects.

First, with a porosity value of $\varepsilon = 0.77$, the velocity within the porous region jumps by a factor of 1.298. This is consistent with the theoretical velocity increase of $1/\varepsilon$, confirming that the porosity is correctly implemented.

Next, both the porosity and the momentum source term are activated, revealing a linear decrease in total pressure as the flow passes through the porous zone. This trend is consistent with observations made in the porous media calibration studies performed by van Dongen [6]. Minor oscillations in the pressure distribution were observed at both the inlet and outlet of the porous zone. These are attributed to flow acceleration at the entrance and rapid expansion at the exit.

Finally, the energy source term is also enabled based on the Nusselt correlation method described in Subsection 2.1. The total temperature shows an initial steep rise before gradually stabilising as the temperature difference between the flow and the wall decreases along the flow direction. This also follows the total temperature trend measured by van Dongen [6].

The overall pressure rise generated by the fan actuator disk model is partially validated through comparison with experimental data gathered from NASA's UHB Drive Rig wind tunnel data [56]. As a first step, the fan rpm of the CC-TF at cruise conditions is determined based on the engine performance of an A320 aircraft during cruise: the engines typically produce between 80.7% and 84% N_1 thrust depending on the weight of the aircraft [60]. The thrust is then converted to sea-level corrected fan speed $N_{1,c}$ through the relation

$$N_{1,c} = \frac{N_1}{\sqrt{\frac{T_{t,0}}{288.15}}}. \tag{21}$$

With freestream cruise-level conditions of $T_{t,0} = 238.15K$ and $M = 0.78$, this results in a 3.8% increase in thrust when at sea level; thus, the A320 requires between 83.76% and 87.19% $N_{1,c}$ thrust. The NASA test experiments from Hughes [56] relate this to a fan pressure ratio of between 1.32 and 1.35.

Results from the CFD simulations show an average total pressure ratio of 1.32 due to the fan actuator disk zone, therefore falling within the expected range for typical cruise. It should be noted that the NASA Test Rig simulates a turbofan with a Design BPR of 8.85, and lower BPR engines tend to have higher total pressure ratios during standard operation. Nevertheless, the data suggests that the CFD calculations fall within reasonable expected values.

While the mass-averaged total fan pressure ratio is compared with experimental data, the radial distribution of total pressure behind the fan is compared with the CFD results obtained by Spinner et al. [26] to assess whether the thrust distribution trend is realistically captured. The study by Spinner et al. [26] analyses a geometry representative of modern high-bypass-ratio turbofan engines, making it a suitable reference model for comparison.

Figure 12 plots the total pressure ratio distribution at station 13, immediately downstream of the fan, compared to the URANS CFD simulations from Spinner et al. [26]. In both datasets, the pressure distribution peaks at a radial distance between 0.7 and 0.8 r/R, consistent with typical thrust-loading patterns in high-bypass fans. However, the Ansys Fluent simulations – based on a modified Goldstein distribution – underpredict the pressure rise near the hub relative to the URANS results with fully modelled rotating blades.

Differences are also observed at the blade tip, where the URANS simulation captures the tip losses and compressibility effects which are absent in the AD method. Additional studies on high BPR fans (See Refs. [44], [51]) report similar radial pressure profiles to those found by Spinner et al. [26], however a decrease in total pressure ratio at the tip of the fan blade is observed. Overall, the pressure ratio trends from the Ansys Fluent simulations provide a satisfactory representation of the expected pressure rise for this duct optimisation study.

Figure 13 plots the swirl angle of the flow at station 15, after the fan and OGVs, compared to results obtained by Spinner et al. [26]. There is an overall agreement in results in the region $0.2 < r/R < 0.9$ where swirl angles are near 0 degrees. Near the engine hub in the region $0 < r/R < 0.2$, there is a negative swirl angle observed both in literature and in the Fluent simulations due to the OGVs over-correcting the swirl introduced by the fan. The differences in fan blade tip effects at station 13 is propagated downstream to the OGVs, evident in the diverging swirl angles in the region $0.9 < r/R < 1$.

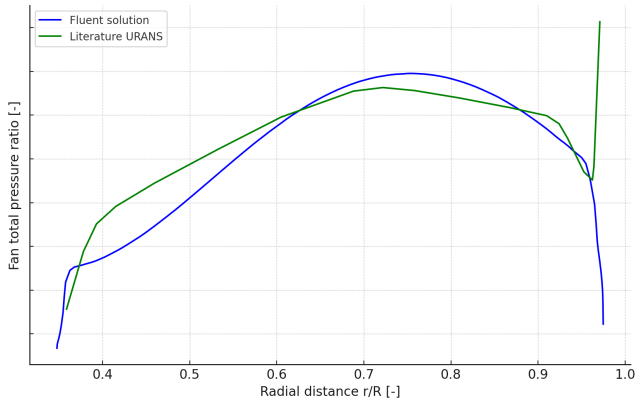

Figure 12: Comparison of the total pressure ratio distributions at station 13, directly after the fan, with literature results gathered from Spinner et al. [26].

The overall behaviour suggests that the implemented actuator disk models predict the tangential component of the airflow well for the majority of the flow, but deviate significantly from expected results compared to literature near the bypass duct walls. The tangential flow component significantly impacts the flow resistance through the downstream HEX: flow with a high swirl angle is not aligned with the path of least resistance through the porous zone, resulting in a dissipation of the flow swirl component and increasing the pressure drop as the airflow enters the HEX.

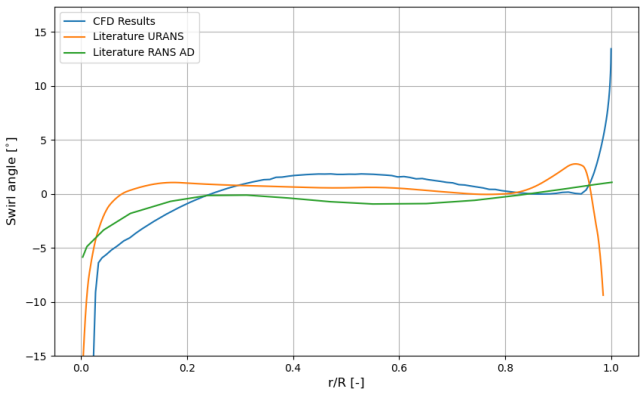

Figure 13: Comparison of the flow swirl angle at station 15, directly after the OGV, with literature results gathered from Spinner et al. [26].

The aerodynamic results and numerical stability of the CFD simulations show a high degree of sensitivity to the thrust distribution prescribed within the fan AD zone. Ansys Fluent consistently achieves a rapid convergence and a stable flow resolution when inputting a constant momentum source term value throughout the zone. In contrast, if the momentum source terms are significantly smaller near the walls compared to the middle region, vortex structures form downstream of the fan and simulation convergence times increase by a factor 3.

Consequently, the custom modified version of the Goldstein thrust distribution makes it feasible to perform an optimisation study with an acceptable aerodynamic representation of the fan and OGV. Since a degree of trial and error is required to determine a robust actuator disk thrust distribution, the AD method is best suited for studies under steady flight conditions where the loading profile remains fixed.

4.2 Impact of Heat Exchanger Integration

CFD simulations were carried out for three engine configurations to isolate the aerodynamic and thermal effects of heat exchanger integration in the bypass duct. The first configuration is the reference turbofan, with the porous zone deactivated, serving as a baseline. The second configuration represents the CC-TF concept with the condenser modelled as a porous region incorporating only momentum source terms, thereby capturing pressure losses but excluding heat transfer effects. The third configuration includes momentum and energy source terms, accounting for the full impact of the condenser by modelling both the pressure drop and thermal energy addition.

The net thrust generated by the bypass stream for each configuration is summarised in Table 4. The condenser integration into the bypass duct results in a 13.7% net thrust penalty relative to the reference engine, however this penalty is reduced to 9.29% when activating the energy source terms. Thus, the addition of thermal energy from the condenser into the duct is partially converted into kinetic energy to offset a portion of the thrust loss associated with integrating the condenser.

Engine configuration	Net Thrust [N]	% Ref. Thrust
Reference turbofan	56083	0
CC-TF, no heat added	48400	-13.7
CC-TF, heat added	50873	-9.29

Table 4: Comparison of the bypass stream net thrust across the different engine configurations.

It should be noted that the baseline engine bypass duct geometry is not optimised; it retains the same wall contours

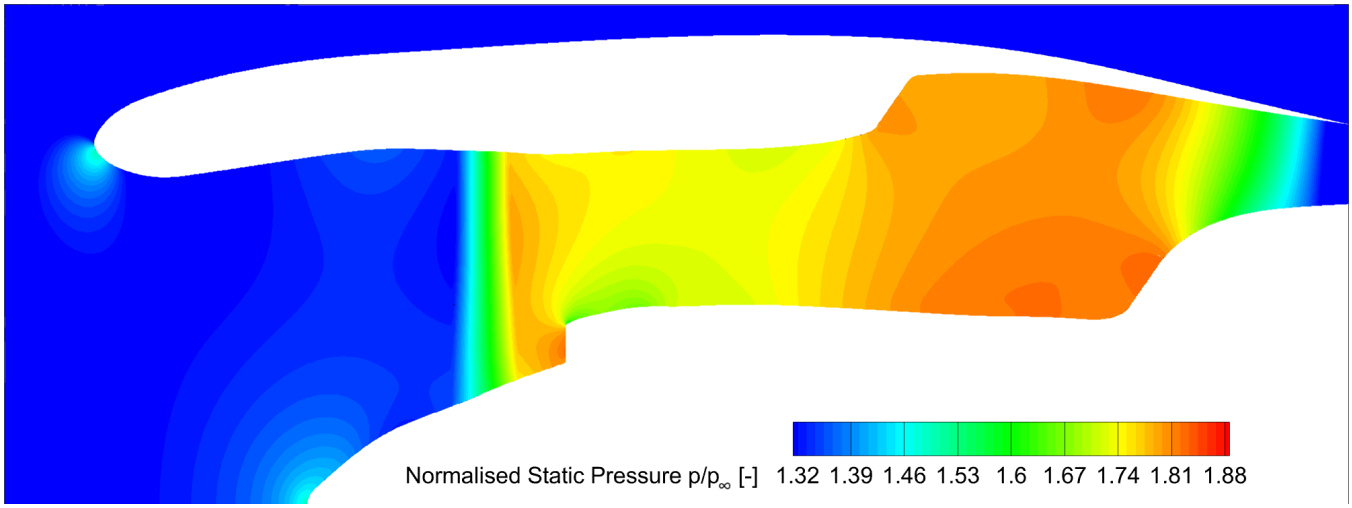

Figure 14: Normalised static pressure contour plot of the reference turbofan without an integrated condenser.

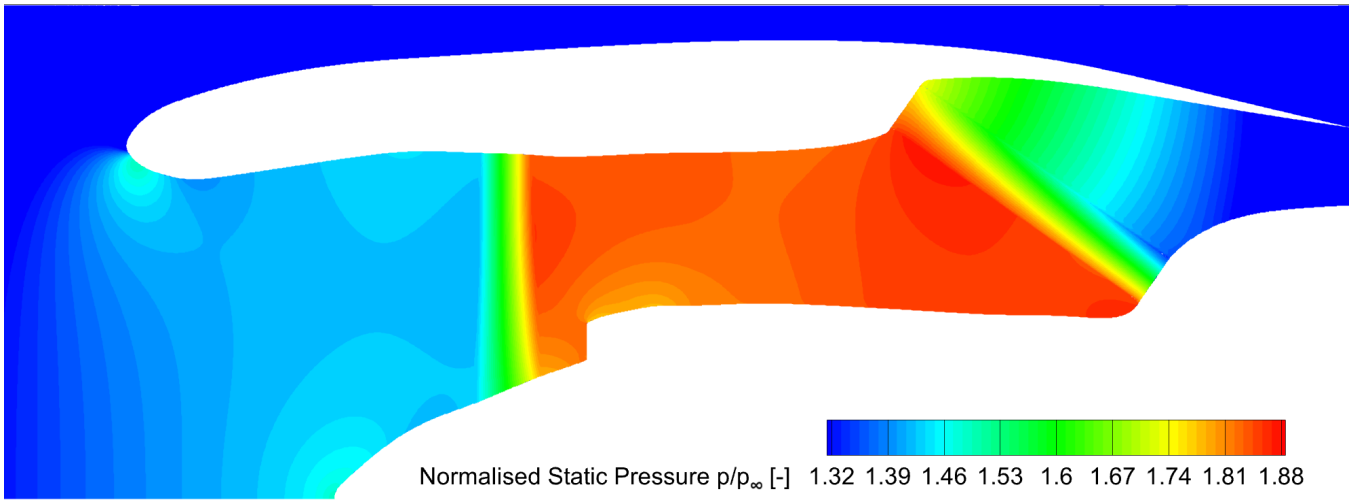

Figure 15: Normalised static pressure contour plot of the turbofan including the integrated condenser.

designed to accommodate the heat exchanger. Nonetheless, this configuration serves as a useful reference for quantifying the aerodynamic penalty associated with HEX integration.

Figures 14 and 15 present the static pressure contours in the bypass duct for the baseline turbofan and the CC-TF configuration with integrated condenser and energy source terms activated. The addition of the HEX results in a more pronounced pre-diffusion effect upstream and leading to a fan inlet pressure of $\frac{p}{p_\infty} = 1.42$. The larger static pressures are caused by the additional blockage introduced by the downstream porous zone, and this effect is also visible after the fan and inside the bypass duct.

A significant pressure drop occurs across the HEX, particularly near the lower section of the duct, where local flow velocities are higher. Directly at the exit of the porous region, a slight pressure jump is observed due to the expansion of the flow cross-sectional area as it exits the porous zone and enters the bypass duct nozzle. In both configurations, the static pressure gradually decreases along the bypass nozzle toward ambient conditions, with a larger pressure drop evident in the baseline engine configuration without the HEX.

To enhance visual clarity, the pressure contour plots in Figures 14 and 15 are truncated below $\frac{p}{p_\infty} = 1.32$ (approximately 35,000 Pa). Despite this, the flow continues to expand downstream, ultimately reaching ambient static pressures of 26436 Pa at the nozzle exit.

Figure 16 shows the total pressure contour of the CC-TF concept with source terms activated. A slight reduction in total pressure is visible on the nacelle outer surface due to shock wave formation at this location. The shock-boundary layer

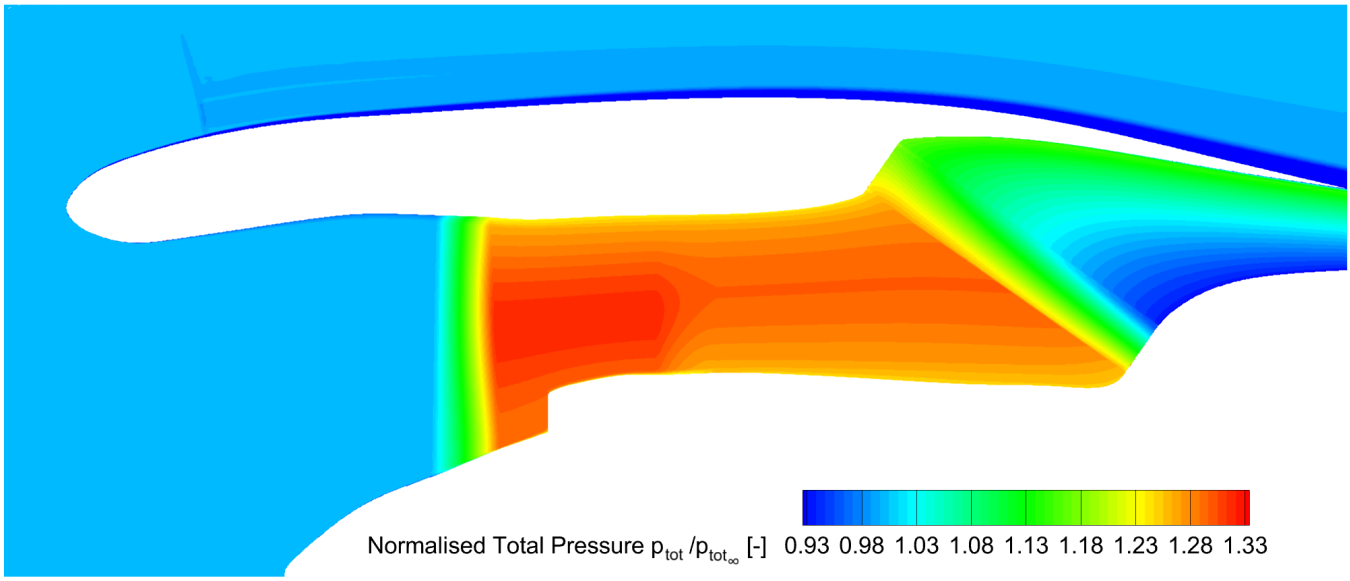

Figure 16: Normalised total pressure contour plot of the entire turbofan modelled geometry.

interaction amplifies this effect, leading to a thickening of the boundary layer downstream of the shock wave.

The total pressure increase across the fan actuator disk is gradual, more accurately reflecting the true effect of the fan compared to an actuator disk that is one element thick. The actuator disk modelling the OGVs introduces a total pressure loss equal to 1.17% of the inlet pressure. This pressure drop falls within the upper bounds of experimental data from the NASA UHB Drive Rig [56], which reports OGV total pressure losses ranging from 0.8% to 1.2% for similar thrust levels, depending on the OGV geometry.

Overall, the total pressure trends around the fan and OGV region closely align with pressure contours from literature (see Refs. [26], [61]), while the position of the shockwave matches the shock position in the axisymmetric turbofan nacelle analysed by Savelyev [55].

Figure 17 presents the static temperature contour plot of the CC-TF condenser and bypass duct outlet with heat transfer simulated. A sharp increase in temperature is observed at the HEX inlet, with closely spaced contour lines indicating a high local heat transfer rate. As the flow progresses through the HEX, the spacing between contour lines increases due to the decreasing temperature difference between HEX walls and airflow, resulting in reduced heat transfer.

The static temperature of the airflow near the upper section of the HEX approaches the working fluid condensation temperature. The airflow velocity in this section ranges between

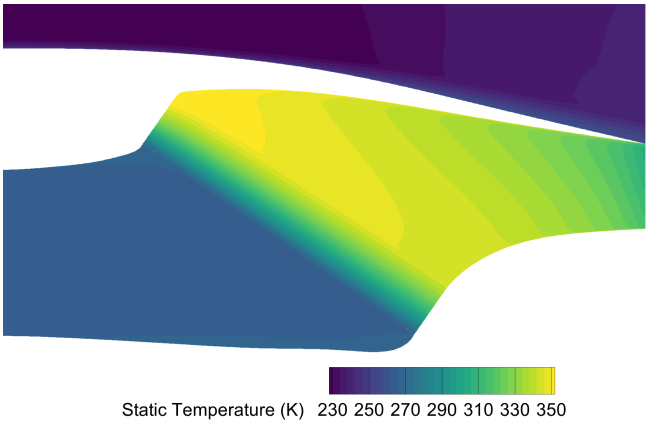

Figure 17: Static temperature contour plot of the HEX and bypass duct outlet.

20 and 40 m/s, compared to between 60 and 70 m/s at near the lower section of the duct. It is desirable to obtain a uniform temperature distribution along the HEX outlet, thereby it leaves room for the optimiser to improve the flow uniformity further. It must be noted that the upstream actuator disk modelling uncertainties influence the flow distribution entering the HEX, thereby affecting the temperature uniformity index.

Along the length of the bypass duct nozzle, the static temperature decreases by 39.1 K on average as the flow accelerates downstream. This temperature drop is due to the conversion of thermal energy into kinetic energy within the expanding duct. The resulting increase in flow momentum leads to a 2473 N increase in net thrust when energy source

terms are activated in the simulation, as observed in Table 4.

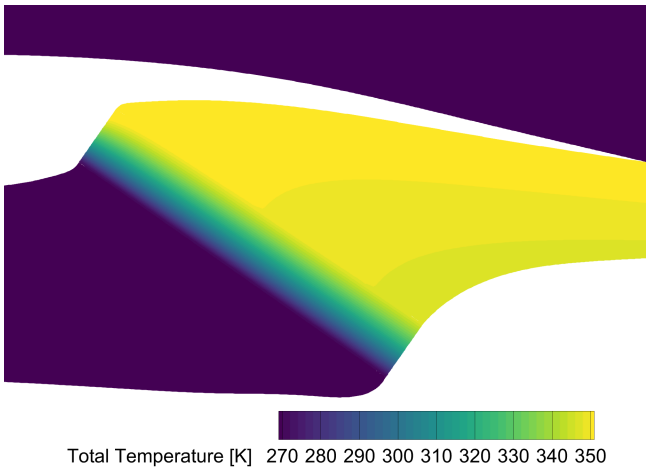

Figure 18: Total temperature contour plot of the HEX and bypass duct outlet.

Figure 18 illustrates the total temperature contour plot for flow passing through the condenser and bypass duct nozzle. The total temperature is constant along the streamlines after exiting the condenser, as expected in the absence of supersonic shocks, external heat transfer or significant viscous dissipation. This confirms that the decrease in static temperature is solely due to the acceleration of the flow in the duct.

4.3 Optimisation Results

The net thrust optimisation of the turbofan cold air stream with integrated condenser was conducted with a total of 220 iterations. The key results and performance metrics of the optimisation process are summarised in Table 5.

Parameter	Initial	Optimised	% Change
Net Thrust [N]	**50873**	**52563**	**+3.32**
HEX flow uniformity [-]	0.927	0.933	+0.65
Heat duty [kW]	8916	8726	-2.13
Outlet velocity [m/s]	287	297	+3.48

Table 5: Summary of the optimisation results. The objective function (net thrust) is highlighted in bold, with additional key performance parameters included.

The best candidate solution achieved a 3.32% increase in net thrust, demonstrating that the optimiser was successfully implemented. Overall, this results in a 6.27% thrust penalty when compared to the reference turbofan simulations with the porous zone deactivated. Previous work by Krempus [47] demonstrated that the power recovered by the ORC generator can supply up to 20% of the total electrical power demand. This indicates that, despite the aerodynamic penalty, the CC-TF configuration retains the potential for overall fuel savings through improved energy recovery.

However, the net thrust improvement comes at the cost of a 2.13% reduction in total heat dissipation, primarily due to a lower mass flow rate through the HEX. A constrained optimisation could be employed instead of the adaptive single-objective optimiser used in this study, in order to impose a pre-specified condenser heat duty.

The optimisation process terminated after reaching the maximum number of iterations rather than satisfying the 0.1% convergence criterion. Minor geometric variations in the bypass duct have a significant effect on the aerodynamic drag of the bypass duct, making it difficult for the optimiser to meet the strict convergence requirement. Despite this, thrust values stabilise after approximately 150 iterations, with the highest net thrust observed at the 165th iteration.

Figure 19 plots the net thrust optimisation progress per iteration. In the early phase of the optimisation, between iterations 1 and 66, a wide spread of net thrust values is observed. This corresponds to the initial design space exploration performed using the Optimal Space Filling DoE. Following this phase, the response surface is generated, and the optimiser begins reducing the search domain around the most promising candidates. The design space is narrowed as the optimisation progresses until the thrust variation between iterations is less than 300N.

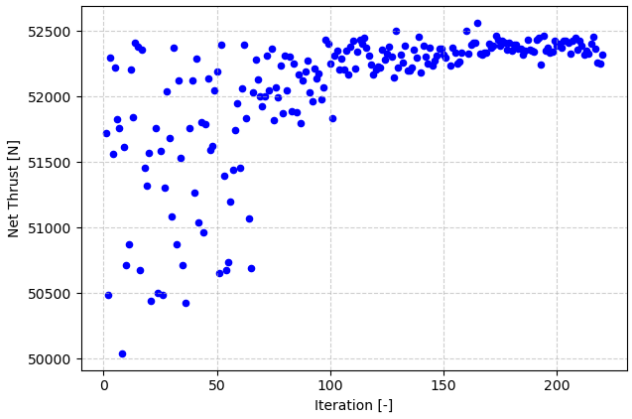

Figure 19: Evolution of the net thrust across the optimisation iterations.

During the optimisation process, four CFD simulations

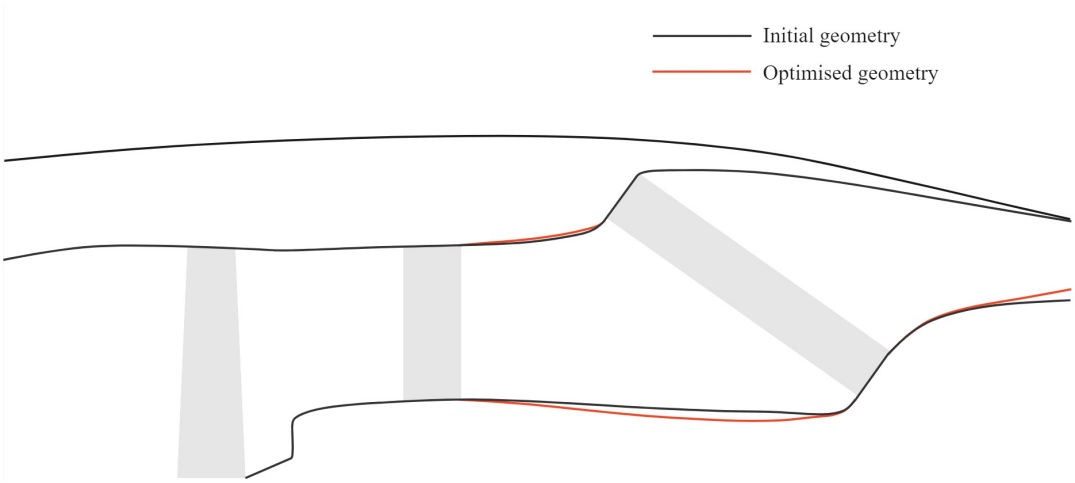

Figure 20: Comparison of the initial turbofan duct geometry with the final optimised solution.

failed to converge. These non-converged designs were treated as design space boundaries, preventing the optimiser from further exploring unstable regions. This adaptive treatment of failed cases helped guide the optimisation towards feasible and stable solutions.

Figure 20 visualises the changes to the bypass duct geometry made by the optimiser compared to the initial geometry. Immediately after the OGVs, the optimised bypass duct widens more than the initial duct, which results in earlier flow diffusion. This adjustment is made without encountering flow separation at the duct walls, maintaining a uniform smooth flow into the HEX. The upper bypass duct wall between the OGV and the HEX is slightly raised compared to the initial design. However, this modification is relatively small and provides marginal gains to the flow diffusion.

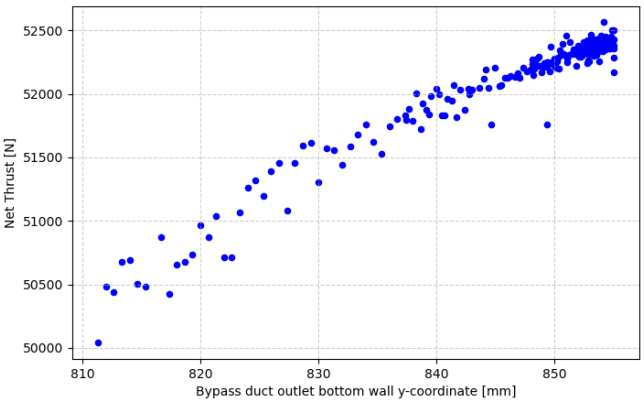

Figure 21: Variation of net thrust as a function of the lower wall height at the bypass duct outlet.

A more significant change occurs at the bypass duct outlet, where the flow passage is restricted compared to the original geometry. This design choice suggests that the thermal energy conversion into additional airflow velocity provides more significant net thrust gains than the penalty of restricting the mass flow. Figure 21 illustrates that increasing the y-coordinate of the bypass duct outlet wall directly correlates with an improved net thrust value.

A 3.48% greater outlet velocity is observed with the optimised bypass duct design compared to the initial duct geometry, most notably at the bottom wall of the bypass duct outlet, where the flow is accelerated more than in the initial design. Moreover, the optimised design slightly improves airflow velocity uniformity at the outlet from 0.971 to 0.976.

The optimisation results suggest that implementing a larger range for upper and lower bounds on the coordinates of the control points could have further increased the net thrust. However, if no constraint is placed on the heat duty, the higher thrust could be associated with a lower heat duty of the condenser. Moreover, excessively wide bounds would increase the likelihood of non-converged solutions, limiting the design space that the optimiser is able to explore. Adopting a CST parametrisation method can improve the geometric smoothness of the nozzle walls, and improving mesh resolution in the outlet region can help mitigate convergence issues.

5 Conclusion and Recommendations

This study investigates the aerodynamic simulation and optimisation of a combined-cycle turbofan (CC-TF) bypass duct to improve the net thrust of the cold air stream. The CC-TF features a condenser integrated in the bypass duct, as part of

the bottoming Organic Rankine Cycle (ORC) which harvests thermal energy from the gas turbine exhaust to improve engine efficiency. The net thrust of the cold air stream is evaluated through 2D axisymmetric Reynolds-averaged Navier-Stokes (RANS) CFD simulations performed in Ansys Fluent.

The engine air intake geometry is modelled to accurately determine the upstream flow diffusion. The change in pressure and flow velocity across the fan and outlet guide vanes (OGVs) is simulated using actuator disk (AD) zones. The condenser porosity, pressure drop and thermal performance are approximated using a porous zone with momentum and energy source terms, allowing for a computationally efficient simulation of the bypass duct flow. This enables a parametric optimisation routine to be performed in Ansys Fluent, to refine the bypass duct geometry and maximise net thrust. The Adaptive Single Objective (ASO) optimisation method, combining an Optimal Space-Filling (OSF) Design of Experiments (DoE), a Kriging response surface, and a MISQP optimiser, was employed to improve the design iteratively.

The verification and validation of the fan and OGV AD models demonstrate a reasonable approximation of the expected airflow pressure and velocity in a high-bypass turbofan. However, the accuracy of the AD models in approximating the expected airflow conditions decreases near the bypass duct walls. The porous zone used to model the condenser exhibits pressure drop and heat transfer behaviour consistent with those observed in previous research for a similar CC-TF application.

The CFD simulations show that integrating a condenser into the bypass duct of a turbofan engine results in a 13.7% net thrust penalty. However, when modelling the heat transfer from the condenser to the bypass flow, the thrust penalty reduces to 9.29%. The contour plots of the modelled domain reveal a significant decrease in static temperature and pressure as the airflow passes through the bypass duct nozzle, due to the thermal energy of the airflow being partially converted into kinetic energy to offset a portion of the thrust loss associated with integrating the condenser. The condenser inclination angle results in an uneven temperature and pressure distribution at the condenser outlet, and consequently the velocity at the bypass duct outlet is also non-uniform.

The optimisation of the bypass duct geometry results in a further 3.32% increase in net thrust, therefore the thrust reduction of the optimised CC-TF engine concept compared to the reference turbofan engine is 6.27%. The optimised duct demonstrates the potential of utilising gradient-based methods to reduce the drag impact of the condenser installation. However, this improvement is accompanied by a 2.13% reduction in heat dissipation, primarily due to a slightly lower mass flow rate through the heat exchanger. The bypass duct nozzle outlet is restricted by the optimiser to improve velocity recovery, thereby increasing the kinetic energy recovery in the nozzle. Small variations in duct geometry have a significant effect on aerodynamic performance, therefore the optimiser is not able to meet the 0.1% convergence tolerance within the set iteration limit.

The obtained results establish a framework for optimising heat exchangers, integrated within a turbofan engine, in a computationally efficient manner. The findings also have the potential to contribute to the ongoing development of several other fuel-efficient propulsion systems requiring an integrated heat exchanger, such as hybrid electric configurations, internal combustion engines using hydrogen as fuel and intercooled-recuperated turbofans. Nevertheless, several limitations remain that present opportunities for future research.

The study focuses solely on single-objective optimisation, prioritising net thrust, whereas a constrained optimisation could provide a more balanced trade-off between thrust improvements and heat transfer efficiency. Additionally, further refinement of the bypass duct outlet geometry beyond the set bounds may yield even greater performance gains.

Future work could explore alternative heat exchanger layouts, such as a V-shaped configuration, to improve the flow uniformity. Expanding this framework to calculate the power provided by the ORC unit turbogenerator would enable an assessment of potential fuel savings of the CC-TF propulsion system.

References

[1] D. McConnachie, C. Wollersheim and R. J. Hansman, "The Impact of Fuel Price on Airline Fuel Efficiency and Operations," *2018 Aviation Technology, Integration, and Operations Conference*, Aug. 2013. DOI: 10.2514/6.2013-4291. [Online]. Available: https://doi.org/10.2514/6.2013-4291.

[2] B. Owen, D. S. Lee and L. Lim, "Flying into the Future: Aviation Emissions Scenarios to 2050," *Environmental Science & Technology*, vol. 44, no. 7, pp. 2255–2260, Mar. 2010. DOI: 10.1021/es902530z. [Online]. Available: https://doi.org/10.1021/es902530z.

[3] S. Mithal and D. Rutherford, "ICAOs 2050 net-zero CO," *POLICY*, Jan. 2023.

[4] C. A. Perullo, D. N. Mavris and E. Fonseca, "An Integrated Assessment of an Organic Rankine Cycle Concept for Use in Onboard Aircraft Power Generation," in *Proceedings of ASME Turbo Expo 2013*, The American Society of Mechanical Engineers, Jun. 2013. DOI: 10.1115/gt2013-95734. [Online]. Available: https://doi.org/10.1115/gt2013-95734.

[5] C. M. De Servi et al., "Exploratory assessment of a combined-cycle engine concept for aircraft propulsion," in *Proceedings of the 1st Global Power and Propulsion Forum, Zurich, Switzerland*, 2017, pp. 16–18.

[6] J. van Dongen, "Modelling and Guidelines for Ram Air Ducts Using the Meredith Effect Applied to an Organic Rankine Cycle Waste Heat Recovery System," M.S. thesis, TU Delft, 2024.

[7] S. Kaiser et al., "The Water-Enhanced Turbofan as Enabler for Climate-Neutral Aviation," *Applied Sciences*, vol. 12, no. 23, p. 12 431, Dec. 2022. DOI: 10.3390/app122312431. [Online]. Available: https://doi.org/10.3390/app122312431.

[8] P. Kwan et al., "Minimising Loss in a Heat Exchanger Installation for an Intercooled Turbofan Engine," in *Proceedings of ASME Turbo Expo 2011*, the American Society of Mechanical Engineers (ASME), Jan. 2011, pp. 189–200. DOI: 10.1115/gt2011-45814. [Online]. Available: https://doi.org/10.1115/gt2011-45814.

[9] D. Missirlis et al, "Optimization of Heat Exchangers for Intercooled Recuperated Aero Engines," *Aerospace*, vol. 4, no. 1, p. 14, Mar. 2017. DOI: 10.3390/aerospace4010014. [Online]. Available: https://doi.org/10.3390/aerospace4010014.

[10] A. Patrao et al., "Compact heat exchangers for hydrogen-fueled aero engine intercooling and recuperation," *Applied Thermal Engineering*, vol. 243, p. 122 538, Jan. 2024. DOI: 10.1016/j.applthermaleng.2024.122538. [Online]. Available: https://doi.org/10.1016/j.applthermaleng.2024.122538.

[11] R. K. Shah and D. P. Sekulic, *Fundamentals of Heat Exchanger Design*. John Wiley & Sons, Ltd, Jul. 2003. DOI: 10.1002/9780470172605. [Online]. Available: https://doi.org/10.1002/9780470172605.

[12] I.V. Tishchenkoet al., "Mathematical modeling of plate-fin heat exchanger in aircraft environmental control system," *AIP conference proceedings*, Jan. 2019. DOI: 10.1063/1.5140174. [Online]. Available: https://doi.org/10.1063/1.5140174.

[13] Z. Liu et al., "Performance of parallel plate-fin heat exchanger for piston aero-engines with front-placed guide plate at high altitude," *Applied Thermal Engineering*, vol. 214, p. 118 829, Jun. 2022. DOI: 10.1016/j.applthermaleng.2022.118829. [Online]. Available: https://doi.org/10.1016/j.applthermaleng.2022.118829.

[14] M. Musto, "A simplified methodology to simulate a heat exchanger in an aircrafts oil cooler by means of a porous media model," *Applied Thermal Engineering*, vol. 94, pp. 836–845, 2015.

[15] S.M. Seyedpour et al., "Contaminant transport in soil: A comparison of the Theory of Porous Media approach with the microfluidic visualisation," *The Science of The Total Environment*, vol. 686, pp. 1272–1281, May 2019. DOI: 10.1016/j.scitotenv.2019.05.095. [Online]. Available: https://doi.org/10.1016/j.scitotenv.2019.05.095.

[16] S. Saneinejad, P. Moonen and J. Carmeliet, "Coupled CFD, radiation and porous media model for evaluating the micro-climate in an urban environment," *Journal of Wind Engineering and Industrial Aerodynamics*, vol. 128, pp. 1–11, Mar. 2014. DOI: 10.1016/j.jweia.2014.02.005. [Online]. Available: https://doi.org/10.1016/j.jweia.2014.02.005.

[17] N. Cancilla et al., "A porous media CFD model for the simulation of hemodialysis in hollow fiber membrane modules," *Journal of Membrane Science*, vol. 646, p. 120 219, Jan. 2022. DOI: 10.1016/j.memsci.2021.120219. [Online]. Available: https://doi.org/10.1016/j.memsci.2021.120219.

[18] H. Darcy, *Les fontaines publiques de la ville de Dijon: exposition et application des principes à suivre et des formules à employer dans les questions de distribution d'eau*. Victor dalmont, 1856, vol. 1.

[19] M. Quintard, "Introduction to heat and mass transport in porous media," *NATO, S&T Organization public release*, 2016.

[20] K. Hooman and H. Gurgenci, "Porous Medium Modeling of Air-Cooled Condensers," *Transport in Porous Media*, vol. 84, no. 2, pp. 257–273, Nov. 2009. DOI: 10.1007/s11242-009-9497-8. [Online]. Available: https://doi.org/10.1007/s11242-009-9497-8.

[21] M. Drela, "Aerodynamics of heat exchangers for high-altitude aircraft," *Journal of Aircraft 33*, vol. 176, 1996.

[22] M. R. Nichols, "Investigation of Flow through an Intercooler Set at Various Angles to the Supply Duct," *NACA Wartime Report*, Apr. 1942. [Online]. Available: https://digital.library.unt.edu/ark:/67531/metadc62653/m2/1/high_res_d/19930093676.pdf.

[23] F. W. Meredith, "Cooling of aircraft engines with special reference to ethylene glycol radiators enclosed in ducts," Aeronautical Research Committee Reports And Memoranda, Tech. Rep. No 1683, Aug. 1935. [Online]. Available: https://naca.central.cranfield.ac.uk/handle/1826.2/1425?show=full.

[24] R. G. Rajagopalan and J. B. Fanucci, "Finite difference model for vertical axis wind turbines," *Journal of Propulsion and Power*, vol. 1, no. 6, pp. 432–436, 1985.

[25] G. Stich et al., "Validation of Actuator Disk, Actuator Line and Sliding Mesh Methods within the LAVA Solver," in *The 11th International Conference on Computational Fluid Dynamics*, 2022.

[26] S. Spinner et al., "A Blade Element Theory Based Actuator Disk Methodology for Modeling of Fan Engines in RANS Simulations," *AIAA Aviation 2019 Forum*, Jun. 2020. DOI: 10.2514/6.2020-2749. [Online]. Available: https://doi.org/10.2514/6.2020-2749.

[27] F. Baratchi et al., "Assessment of blade element actuator disk method for simulations of ducted tidal turbines," *Renewable Energy*, vol. 154, pp. 290–304, 2020.

[28] S. Goldstein and L. Prandtl, "On the vortex theory of screw propellers," *Proceedings of the Royal Society of London Series A Containing Papers of a Mathematical and Physical Character*, vol. 123, no. 792, pp. 440–465, Apr. 1929. DOI: 10.1098/rspa.1929.0078. [Online]. Available: https://doi.org/10.1098/rspa.1929.0078.

[29] H. Kodama and S. Nagano, "Potential Pressure Field by Stator/Downstream Strut Interaction," *Journal of Turbomachinery*, vol. 111, no. 2, pp. 197–203, Apr. 1989. DOI: 10.1115/1.3262256. [Online]. Available: https://doi.org/10.1115/1.3262256.

[30] E. Tinoco and A. Chen, "Transonic CFD applications to engine/airframe integration," *22nd Aerospace Sciences Meeting*, Jan. 1984. DOI: 10.2514/6.1984-381. [Online]. Available: https://doi.org/10.2514/6.1984-381.

[31] H. Hoheisel, "Aerodynamic aspects of engine-aircraft integration of transport aircraft," *Aerospace Science and Technology*, vol. 1, no. 7, pp. 475–487, Oct. 1997. DOI: 10.1016/s1270-9638(97)90009-2. [Online]. Available: https://doi.org/10.1016/s1270-9638(97)90009-2.

[32] I. Goulos et al., "Civil turbofan propulsion aerodynamics: Thrust-drag accounting and impact of engine installation position," *Aerospace Science and Technology*, vol. 111, p. 106 533, Jan. 2021. DOI: 10.1016/j.ast.2021.106533. [Online]. Available: https://doi.org/10.1016/j.ast.2021.106533.

[33] C. Clemen, P. Albrecht and S. Herzog, "Systematic Optimisation of a Turbofan Bypass Duct System," in *Proceedings of ASME Turbo Expo 2012*, the Amer-

ican Society of Mechanical Engineers, Jun. 2012, pp. 1655–1666. DOI: 10.1115/gt2012-68276. [Online]. Available: https://doi.org/10.1115/gt2012-68276.

[34] R. Bajimaya et al., "Heat exchanger integration with an aero-engine bypass duct," *Aerospace Europe Conference 2023 10th EUCASS 9th CEAS*, 2023.

[35] H. Witte and C. Bode, "Gradient-based optimization of the propulsor bypass duct under the influence of functionally integrated heat transfer structures," in *AIAA SCITECH 2025 Forum*, The American Institute of Aeronautics and Astronautics, 2025, p. 2107. DOI: 10.2514/6.2025-2107. [Online]. Available: https://doi.org/10.2514/6.2025-2107.

[36] D. W. Zingg, M. Nemec and T. H. Pulliam, "A comparative evaluation of genetic and gradient-based algorithms applied to aerodynamic optimization," *European Journal of Computational Mechanics*, pp. 103–126, Aug. 2008. DOI: 10.13052/remn.17.103-126. [Online]. Available: https://doi.org/10.13052/remn.17.103-126.

[37] R. Christie et al., "The use of hybrid intuitive class shape transformation curves in aerodynamic design," *Aerospace Science and Technology*, vol. 95, p. 105 473, Oct. 2019. DOI: 10.1016/j.ast.2019.105473. [Online]. Available: https://doi.org/10.1016/j.ast.2019.105473.

[38] H. Sobieczky, "Parametric Airfoils and Wings," *Notes on Numerical Fluid Mechanics*, vol. 68, Vieweg Verlag, pp. 71–88, 1999.

[39] ANSYS Inc., *Ansys Fluent Theory Guide*. ANSYS Inc. Press, 2023.

[40] Y. Kaplan, "Aerodynamic optimization of inlet design for high bypass ratio turbofan," M.S. thesis, Middle East Technical University, 2024.

[41] A. Heidebrecht et al., "Parametric Geometry and CFD Process for Turbofan Nacelles," in *ASME Turbo Expo 2016: Turbomachinery Technical Conference and Exposition*, the American Society of Mechanical Engineers (ASME), Jun. 2016. DOI: 10.1115/gt2016-57784. [Online]. Available: https://doi.org/10.1115/gt2016-57784.

[42] F. Mund et al., "Enhanced Gas Turbine Performance Simulation Using CFD Modules in a 2D Representation of the Low-Pressure System for a High-Bypass Turbofan," *Journal of Engineering for Gas Turbines and Power*, vol. 129, no. 3, pp. 761–768, Feb. 2006. DOI: 10.1115/1.2364197. [Online]. Available: https://doi.org/10.1115/1.2364197.

[43] H. Zimmermann et al., "CFD Study of Nozzle Configurations for Ultra High Bypass Engines," in *International Gas Turbine and Aeroengine Congress and Exposition*, the American Society of Mechanical Engineers (ASME), May 1993. DOI: 10.1115/93-gt-389. [Online]. Available: https://doi.org/10.1115/93-gt-389.

[44] M. Zennaro, "Cfd simulation of a transonic fan: Mesh sensitivity study, mapping and 3d validation," M.S. thesis, Università degli Studi di Padova, 2020.

[45] A. Peters et al., "Ultrashort Nacelles for Low Fan Pressure Ratio Propulsors," *Journal of Turbomachinery*, vol. 137, no. 2, Aug. 2014. DOI: 10.1115/1.4028235. [Online]. Available: https://doi.org/10.1115/1.4028235.

[46] J. Kirz, A.R. Hübner and S. Spinner, "Systematic numerical investigations of heat exchangers integrated behind propellers of hybrid-electric propulsion aircraft configurations," in *Deutscher Luft- und Raumfahrtkongress 2023*, 2023. DOI: 10.25967/610201.

[47] D. Krempus, "Organic Rankine Cycle Waste Heat Recovery Systems for Aircraft Engines," Ph.D. dissertation, Delft University of Technology, 2025. DOI: 10.4233/uuid:5e565f99-a9f4-4208-95e9-2c542fd720f8. [Online]. Available: https://doi.org/10.4233/uuid:5e565f99-a9f4-4208-95e9-2c542fd720f8.

[48] F. Beltrame et al., "Reduced Order Modelling of Optimized Heat Exchangers for Maximum Mass-Specific Performance of Airborne ORC Waste Heat Recovery Units," in *Proceedings of the 7th International Seminar on ORC Power Systems*, Jan. 2024, pp. 563–573. DOI: 10.12795/9788447227457_93. [Online]. Available: https://doi.org/10.12795/9788447227457_93.

[49] E. N. Sieder and G. E. Tate, "Heat Transfer and Pressure Drop of Liquids in Tubes," *Industrial Engineering Chemistry*, vol. 28, no. 12, pp. 1429–1435, Dec. 1936. DOI: 10.1021/ie50324a027. [Online]. Available: https://doi.org/10.1021/ie50324a027.

[50] W. Sutherland, "LII. The viscosity of gases and molecular force," *The London Edinburgh and Dublin Philosophical Magazine and Journal of Science*, vol. 36, no. 223, pp. 507–531, Dec. 1893. DOI: 10.1080/14786449308620508. [Online]. Available: https://doi.org/10.1080/14786449308620508.

[51] F. C. Mund and P. Pilidis, "Performance simulation of a high-bypass turbofan with a 2D representation of the intake and fan components," *The Aeronautical Journal*, vol. 112, no. 1137, pp. 673–682, Nov. 2008. DOI: 10.1017/s0001924000002645. [Online]. Available: https://doi.org/10.1017/s0001924000002645.

[52] S. Ahlinder, "On Modelling of Compact Tube Bundle Heat Exchangers as Porous Media for Recuperated Gas Turbine Engine Applications," Ph.D. dissertation, BTU Cottbus-Senftenberg, 2006.

[53] F. Menter, "Improved two-equation k-omega turbulence models for aerodynamic flows," *NASA STI/Recon Technical Report N*, vol. 93, pp. 22 809–, Oct. 1992. [Online]. Available: https://ntrs.nasa.gov/api/citations/19930013620/downloads/19930013620.pdf.

[54] F. Menter, "Zonal Two Equation k-w Turbulence Models For Aerodynamic Flows," *23rd Fluid Dynamics, Plasmadynamics, and Lasers Conference*, Jul. 1993. DOI: 10.2514/6.1993-2906. [Online]. Available: https://doi.org/10.2514/6.1993-2906.

[55] A. Savelyev et al., "Nacelle design and optimization for ultra high bypass ratio turbofan," in *Proc., Greener Aviation Conf. Melville, NY: AIP Publishing LLC*, 2016.

[56] C. Hughes, "Aerodynamic performance of scale-model turbofan outlet guide vanes designed for low noise," in *40th AIAA Aerospace Sciences Meeting & Exhibit*, Jan. 2002. DOI: 10.2514/6.2002-374. [Online]. Available: https://doi.org/10.2514/6.2002-374.

[57] D. B. Spalding, "A Single Formula for the Law of the Wall," *Journal of Applied Mechanics*, vol. 28, no. 3, pp. 455–458, Sep. 1961. DOI: 10.1115/1.3641728. [Online]. Available: https://doi.org/10.1115/1.3641728.

[58] B. C. Mandal and H. P. Mazumdar, "The importance of the law of the wall," *International Journal of Applied Mechanics and Engineering*, vol. 20, no. 4, pp. 857–869, Dec. 2015. DOI: 10.1515/ijame-2015-0055. [Online]. Available: https://doi.org/10.1515/ijame-2015-0055.

[59] B. J. McKeon et al., "Friction factors for smooth pipe flow," *Journal of Fluid Mechanics*, vol. 511, pp. 41–44, Jul. 2004. DOI: 10.1017/s0022112004009796. [Online]. Available: https://doi.org/10.1017/s0022112004009796.

[60] Airbus, *A320/321 Flight Crew Training Manual*, 2008.

[61] A. Piccoli, "A body force method implementation in a computational fluid dynamics solver," M.S. thesis, Università degli Studi di Padova, 2020.

Appendix A: Additional Contour Plots

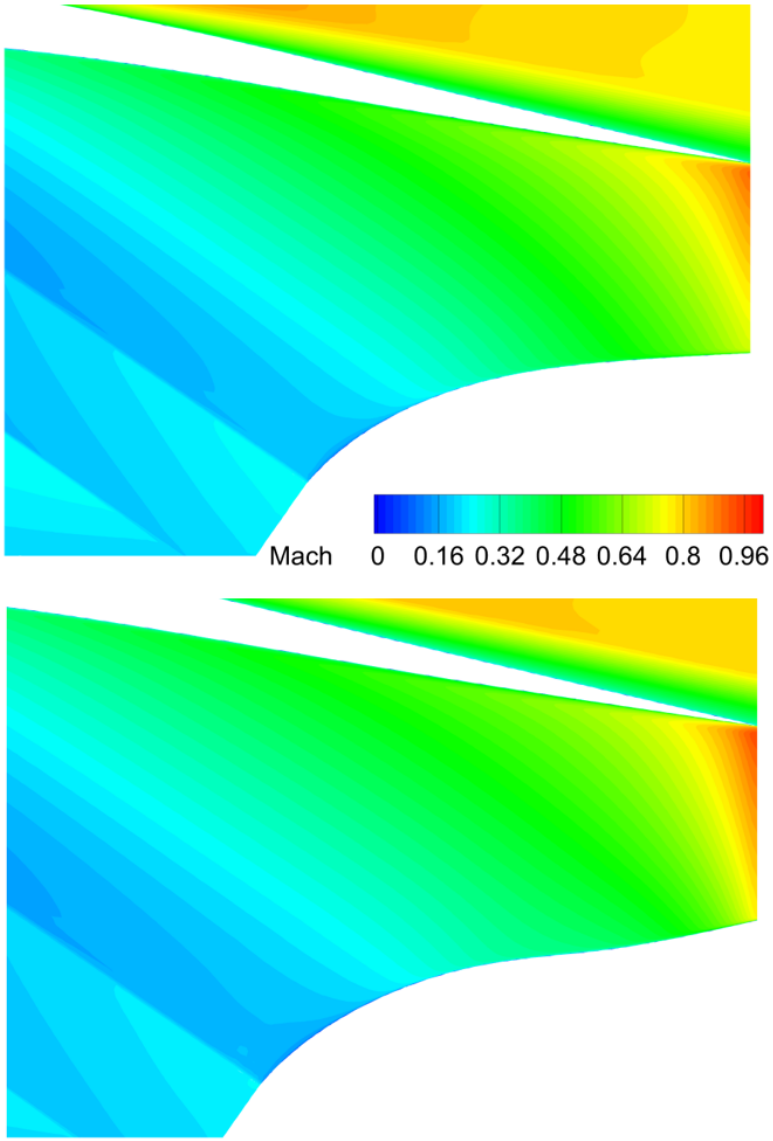

Figure 1: Mach contour plot of the bypass duct outlet for the initial (top) and optimised (bottom) CC-TF bypass duct geometries.

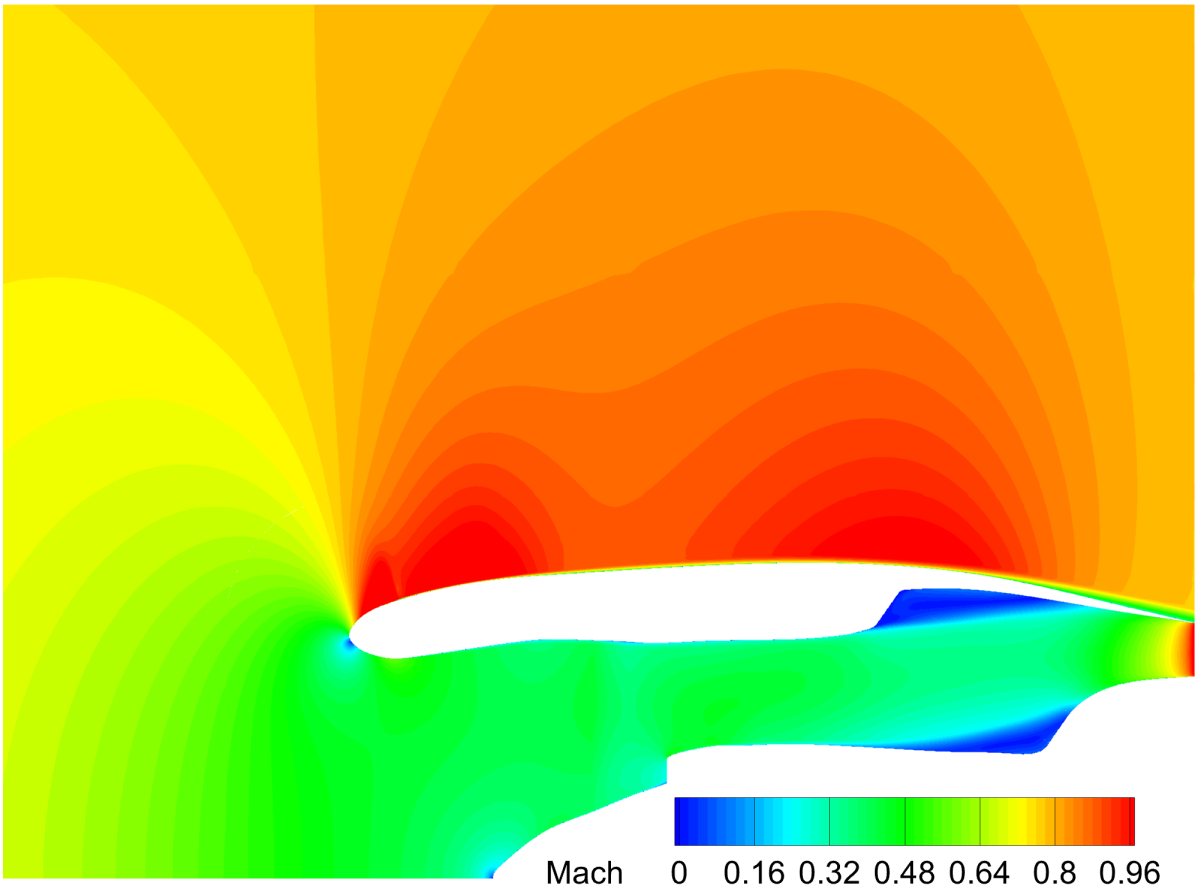

Figure 2: Mach number contour plot for the reference turbofan geometry.

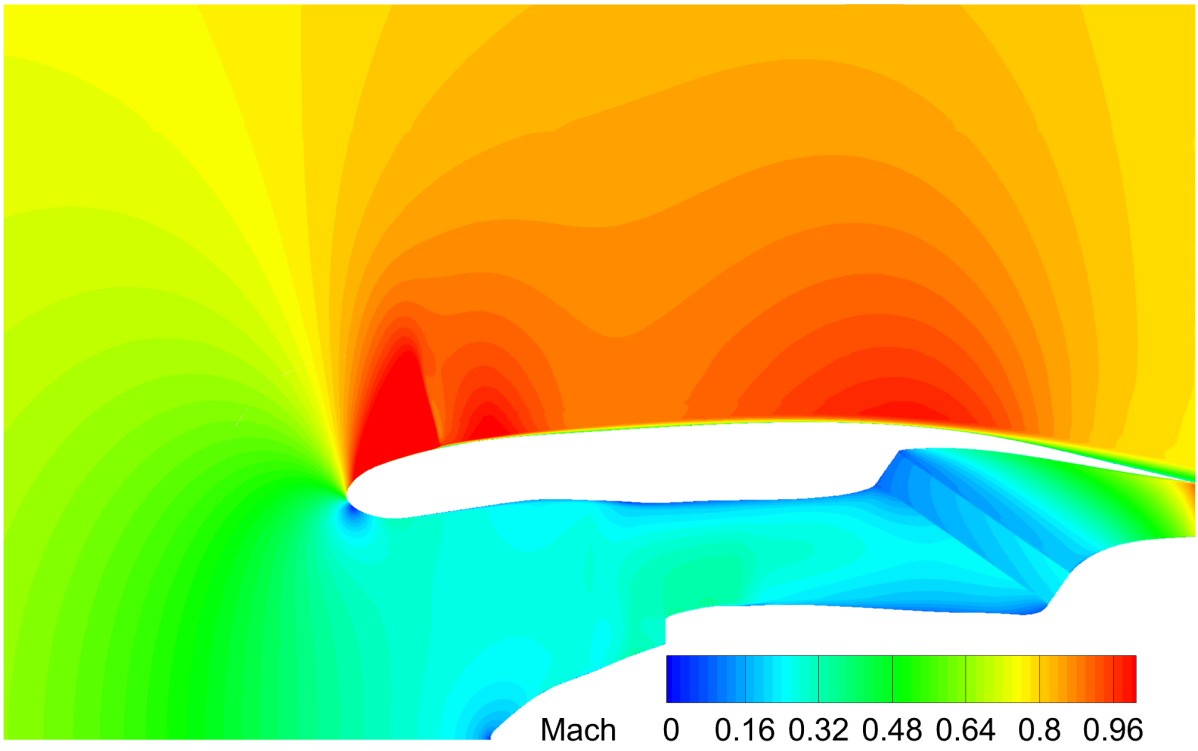

Figure 3: Mach number contour plot for the initial CC-TF geometry.

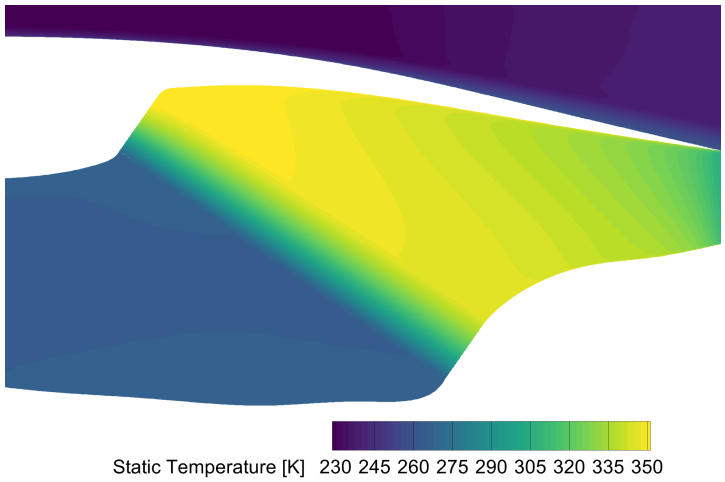

Figure 4: Static temperature contour plot for the optimised CC-TF geometry.

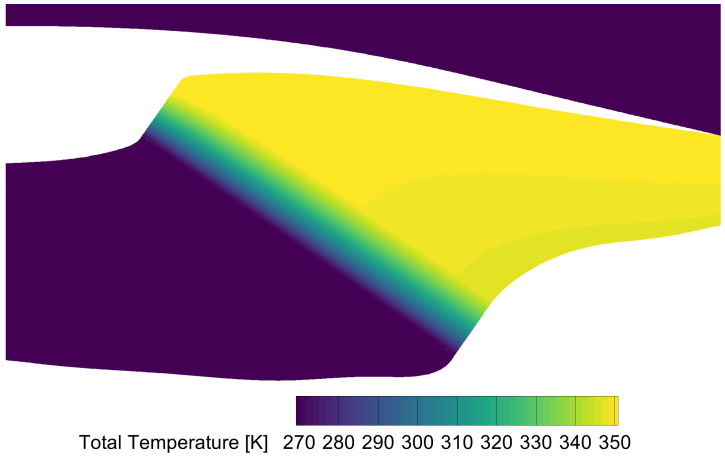

Figure 5: Total temperature contour plot for the optimised CC-TF geometry.

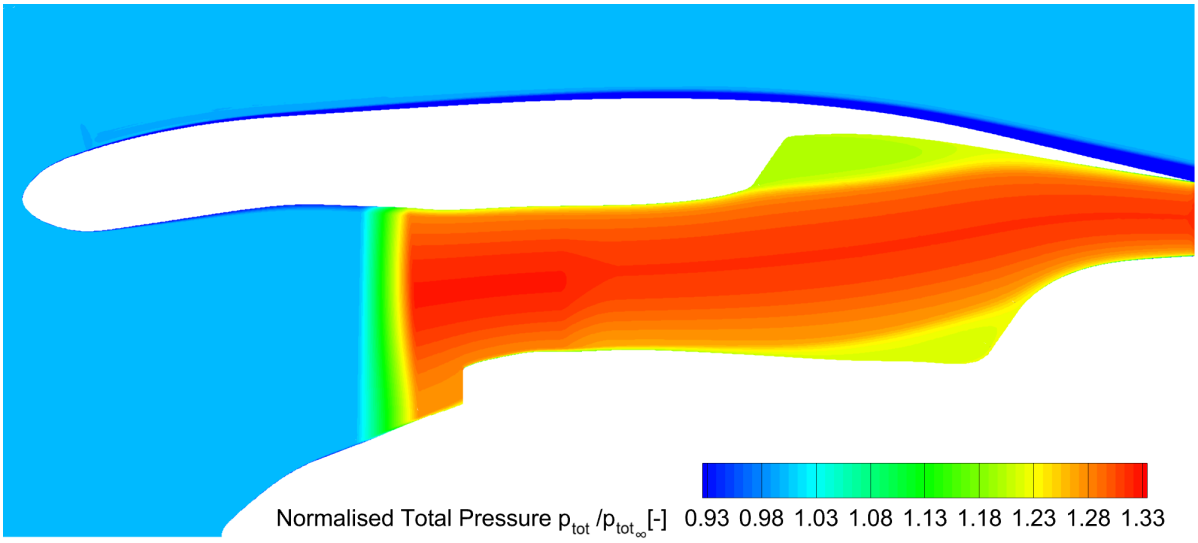

Figure 6: Normalised total pressure contour plot for the reference turbofan geometry.

Aerodynamic Optimisation of a Turbofan Bypass Duct with a Heat Exchanger Modelled as a Porous Zone

AE4020: Literature Study

by

Kalyan Wessendorp

Daily Supervisor:	F. Beltrame
Responsible Supervisor:	M. Pini
Submission Date:	23 May 2025
Faculty:	Faculty of Aerospace Engineering, Delft

Cover: Turbofan engine cross-sectional view (iStock photo)

TU Delft

Summary

The long-term goal of achieving net-zero carbon emissions from aviation by 2050, as set by the International Civil Aviation Organization (ICAO), has spurred the design of new fuel-efficient jet engine configurations. Among promising propulsion systems stand out hybrid electric configurations, internal combustion engines using hydrogen as fuel, intercooled-recuperated turbofans and combined cycle turbofan (CC-TF) concepts. Among the CC-TF configurations, this thesis focuses on a gas turbine with a bottoming Organic Rankine Cycle (ORC) unit that harvests the thermal energy in the exhaust and converts it into useful work. The waste heat recovery (WHR) system necessitates the integration of a condenser rejecting thermal energy to the freestream airflow. This research investigates the effect of integrating the condenser within the bypass duct of a turbofan engine, with the aim of optimising the net thrust of the cold air stream and thereby contributing to industry efforts to achieve net-zero carbon emissions. The use of simplified computational fluid dynamics (CFD) techniques in ANSYS Workbench, such as a porous media model to simulate the presence of a heat exchanger (HEX) within the computational domain, reduces the total simulation time and makes the optimisation practical. Therefore, this literature study analyses relevant research to set up and perform the CC-TF simulations.

In order to accurately simulate the flow features within the HEX core, its important features and assumptions must first be identified. A flat-tube microchannel HEX with louvred fins is chosen as the condenser topology due to the high level of heat transfer area compactness. The wall temperature of the porous zone is assumed constant due to the small influence of the desuperheating zone on the overall weighted average value. However, in cases where desuperheating and/or subcooling may be significant, the constant wall temperature assumption may be too limiting.

The introduction of momentum and energy source terms in the Reynolds-averaged Navier–Stokes (RANS) equations enables the simulation of the HEX pressure drop and heat transfer using a porous zone in CFD simulations. The momentum source term is based on the Darcy-Forchheimer equation, a quadratic function of the air velocity with coefficients determining the pressure drop and using a representative porosity of $\varepsilon = 0.77$. The energy source term is based on the local Nusselt number, which is determined through an empirical correlation that relates it to the Reynolds and Prandtl numbers. A porous zone efficiently simulates the effect of the presence of the HEX core on the airflow while reducing computational cost and can be adapted to various HEX designs by adjusting its coefficients and porosity.

The geometry and placement of the condenser within the bypass duct can considerably affect the aerodynamic efficiency. The use of an annular HEX allows for a 2D axisymmetric simulation to be performed, simplifying the CFD setup and reducing the required computational resources. The annular design also maximises the heat exchanger frontal area, although a drawback is that annular designs are more challenging to produce and maintain in practice. Higher HEX inclination angles result in more space-efficient integration, although beyond a 70° angle, the airflow pressure losses increase greatly. The thermal energy rejected by the condenser to the bypass duct airflow can be partially converted into kinetic energy through careful tuning of the bypass duct nozzle geometry. The reduction of the drag penalty introduced by the presence of the HEX by means of accelerating the heated airflow is referred to as the Meredith effect. This effect has been employed previously to reduce the drag contribution of a ducted HEX, most notably in the P51 Mustang introduced in the 1940s.

The LEAP-1A high-bypass ratio engine is chosen as the baseline testcase for this study, as its geometry and performance characteristics are available in the open literature. The fan and outlet guide vanes (OGVs) can be effectively simplified in CFD simulations using actuator disk models, which impose a momentum source term to increase the pressure of the flow. For RANS simulations, this can be seen as a time-averaged solution of the airflow through the fan and OGVs. The actuator disks can be set up following Blade Element Momentum (BEM) theory, but this requires detailed fan geometry information that is unavailable to the author. Therefore, a custom loading profile is inputted into ANSYS Fluent based on the Goldstein load distribution, as it has been shown in literature to represent the real-life

thrust distribution of a turbofan engine adequately.

The axisymmetric CFD model neglects the aerodynamic effect of the engine pylon and the wing, as it is assumed that these components have minimal impact on the bypass duct flow and the resulting duct optimisation outcome. Circumferential pressure and flow velocity fluctuations are also not captured, although methods are available to model these effects in future 3D simulations. The CFD model includes the upstream airflow, air intake geometry and engine nacelle to account for the pre-diffusion of the flow entering the engine and its effects on the downstream airflow. A hybrid structured-unstructured CFD mesh is identified as a robust grid for optimisation geometry changes, although it can result in increased computational time compared to a structured mesh. The turbulence models considered for this study are k-ω SST, k-ε and Spalart-Allmaras (S-A), of which the k-ω SST model is preferred for its superior accuracy in resolving flow both inside the porous zone and in the rest of the CFD domain.

Next, methods to verify the chosen mesh size are identified, namely through a grid convergence study and analysis of the y^+ and u^+ values in the turbulent boundary layer. The correct implementation of the porous zone is verified in a straight duct section, where the pressure drop and temperature increase can be more easily observed. The actuator disk implementation can be compared against total pressure and velocity distributions obtained from other CFD studies and experimental data collected by NASA's UHB Drive Rig. Lastly, a sensitivity analysis assesses the robustness of the actuator disk implementation: the thrust distribution is varied to analyse its effects on both thrust and flow dynamics within the bypass duct. The verification and validation procedures identified in this literature study are crucial for achieving a more accurate representation of the condenser and fan modelling, thereby enhancing the reliability of the simulations.

With the essentials of setting up the CFD model covered, the available optimisation routines are compared. While it is common in previous research to use genetic algorithms and other derivative-free methods for duct optimisation, gradient-based methods are identified as the preferred approach due to faster convergence and easy implementation within ANSYS Fluent. The Adaptive Single-Objective routine is chosen as the preferred approach, as it is a hybrid of the Design of Experiments (DoE) method and a gradient-based routine called Mixed-Integer Sequential Quadratic Programming (MISQP). A significant advantage of combining the DoE and gradient-based approaches is that the risk of landing on a local solution minimum is reduced, allowing the routine to sample a larger design space. The parametrisation method of the bypass duct geometry is narrowed down to two approaches: using control points with splines or through Class Shape Transformation (CST) functions. A control points method using cubic splines is preferred for this research, with fixed axial positions and a range in which the radial position can vary. The size and shape of the original LEAP-1A engine nacelle constrain the bounds of the control points.

The available literature currently lacks studies on the CFD-based geometric optimisation of turbofan engines that incorporate a heat exchanger in the bypass duct. A porous zone and actuator disk model can be used in place of the HEX and fan, respectively, to reduce the computational time associated with the geometric optimisation. The research question for this thesis has been formulated accordingly:

"How can integrating a condenser within the bypass duct of a turbofan engine be optimised to maximise the net thrust using a computationally efficient CFD optimisation framework?"

The scope of the research is also defined:

"**Assessing the suitability of a gradient-based CFD optimisation framework to determine the optimal bypass duct geometry of a Combined-Cycle turbofan**
by
employing a porous zone to simulate the heat exchanger and an actuator disk to model the fan and outlet guide vanes to significantly reduce the computational cost of the problem."

Contents

Nomenclature

Abbreviations

Abbreviation	Definition
ASO	Adaptive Single-Objective
BEM	Blade Element Momentum
BHP	Brake Horsepower
BPR	Bypass Ratio
BWB	Blended-Wing Body
CAD	Computer-Aided Design
CC-TF	Combined-Cycle Turbofan
CFD	Computational Fluid Dynamics
CST	Class Shape Transformation
DES	Detached Eddy Simulation
DNS	Direct Numerical Simulation
DoE	Design of Experiments
ECS	Environmental Control System
FPR	Fan Pressure Ratio
GA	Genetic Algorithm
HEX	Heat Exchanger
ICAO	International Civil Aviation Organization
LEAP	Leading Edge Aviation Propulsion
LES	Large Eddy Simulation
LHS	Left-Hand Side
MISQP	Mixed-Integer Sequential Quadratic Programming
NASA	National Aeronautics and Space Administration
NLPQL	Nonlinear Programming by Quadratic Lagrangian
NSGA-II	Natural Search Genetic Algorithm II
OGV	Outlet Guide Vanes
ORC	Organic Rankine Cycle
RANS	Reynolds-Averaged Navier–Stokes
RHS	Right-Hand Side
rpm	Revolutions per Minute
S-A	Spalart-Allmaras
SQP	Sequential Quadratic Programming
SST	Shear Stress Transport
UHBPR	Ultra-High Bypass Ratio
URANS	Unsteady Reynolds-Averaged Navier–Stokes
WHR	Waste Heat Recovery

Symbols

Symbol	Definition	Unit
A	Area	m^2
a	Velocity reduction factor through heat exchanger	-
a_i	Shape function coefficient	-
$B_i(x)$	Bernstein polynomial	-

Symbol	Definition	Unit
b	Velocity reduction factor at duct exit	-
$C(x)$	Class function	-
C_D	Drag coefficient	-
CD_{kw}	Cross diffusion	-
C_L	Lift coefficient	-
C_M	Moment coefficient	-
C_Q	Torque coefficient	-
C_T	Thrust coefficient	-
C_1	Viscous resistance coefficient	-
C_2	Inertial resistance coefficient	-
D	Diameter	m
$\mathbf{D}$	Viscous resistance coefficient matrix	-
D_{eq}	Hydraulic diameter	m
D_{HEX}	Heat exchanger drag	-
E	Energy	J
F	Force	N
$\mathbf{F}$	Inertial resistance coefficient matrix	-
F_1	SST Blend Function 1	-
F_2	SST Blend Function 2	-
g	Gravity	m/s^2
h	Heat transfer coefficient	$W/m^2 \cdot K$
h	Height	m
$\dot{H}$	Heat rejection rate	W
I	Identity matrix	-
k	Turbulent kinetic energy	m^2/s^2
k	Thermal conductivity	$W/m \cdot K$
k_h	Hydraulic conductivity	m/s
K	Specific permeability	m^2
l	Microchannel length scale	m
L	Heat exchanger length	m
m	Mass	kg
m	Nusselt number relation coefficient	-
M	Mach number	-
N	Class function exponent	-
n	Nusselt number relation coefficient	-
Nu	Nusselt number	-
P	Power	W
P	Pressure	Pa
p	Pressure	Pa
Pr	Prandtl number	-
q	Heat flux	W/m^2
q	Freestream dynamic pressure	Pa
Q	Heat	J
$\dot{Q}$	Heat transfer rate	W
r	Radial distance	m
Re	Reynolds number	-
R	Gas constant	$J/kg \cdot K$
rpm	Revolutions per minute	min^{-1}
S_e	Energy source term	-
S_m	Momentum source term	-
$S(x)$	Shape function	-
T	Temperature	K
T	Thrust	N
t	Heat exchanger thickness	m

Symbol	Definition	Unit
t	Time	s
u	Velocity	m/s
u_a^*	Induced axial velocity	m/s
u_t^*	Induced tangential velocity	m/s
v	Velocity	m/s
V	Velocity	m/s
V_p	Volume of pores	m^3
V_t	Total volume	m^3
x, y, z	Cartesian coordinates	m
α	Angle of attack	deg
β	Coefficient for fluid phase in heat exchanger	-
β	Compactness	m^{-1}
β	Blade angle	deg
β^*	Turbulent dissipation constant	-
γ	Specific heat ratio	-
δ	Boundary layer thickness	m
δ_{ij}	Kronecker delta	-
ϵ	Dissipation rate of turbulent kinetic energy	m^2/s^3
ϵ	Porosity	-
η	Efficiency	-
Γ	Circulation	m^2/s
λ	Thermal conductivity	W/m·K
μ	Dynamic viscosity	Pa·s
μ_t	Turbulent (eddy) viscosity	Pa·s
ν	Kinematic viscosity	m^2/s
ϕ	Scalar constant to be blended (turbulence equation)	-
ϕ	Pitch angle	deg
ψ	Stream function	m^2/s
ρ	Density	kg/m^3
σ	Coefficient for solid phase in heat exchanger	-
τ	Shear stress	Pa
ω	Specific dissipation rate of turbulence	s^-1
ω	Rotational velocity/vorticity	s^-1

Subscripts and Superscripts

Subscript	Definition
a	Axial direction
abs	Absolute
β	Fluid phase
$casing$	Turbofan nacelle inner casing
c	Cold side
D	Drag
d	Drag
e	Energy
e	Turbofan exit
eff	Effective
eq	Equivalent
f	Fluid
HEX	Heat exchanger
$HEXcore$	Heat exchanger core
h	Hydraulic
h	Hot side
hub	Turbofan hub
i	Induced
i	i-th element
i	Tensor notation spatial direction
j	Tensor notation spatial direction
k	Tensor notation spatial direction
l	Lift
m	Mean

Subscript	Definition
m	Momentum
M	Mach number
max	Maximum value
min	Minimum value
o	Outlet
p	Pores
$prop$	Propulsive
ref	Reference condition
rel	Relative
rms	Root mean square
r	Radial direction
s	Solid
σ	Solid phase
t	Tangential direction
t	Time
t	Turbulent
th	Thermal
τ	Shear
w	Wall
x	Axial direction
z	Swirl direction
∞	Freestream
0	External (outside turbofan)

Superscript	Definition
$*$	Non-dimensional parameter
$'$	Fluctuating quantity
$+$	Wall units (e.g., y^+)
$-$	Time-averaged value

1

Introduction

Jet engine design is rapidly evolving, driven by the imperative to enhance the fuel efficiency of passenger aircraft. While this can be partially attributed to the significant increase in fuel prices over the past 20 years [1], these efficiency improvements are essential for minimising environmental impact of the aviation industry, currently contributing around 3% of total greenhouse gas emissions [2]. The International Civil Aviation Organization (ICAO) member states adopted a long-term target of reaching net zero carbon dioxide emissions from international aviation by 2050 [3]. A potential solution for mitigating these greenhouse emissions is the develoment of emerging new propulsion systems, such as hybrid electric configurations, internal combustion engines using hydrogen as fuel, intercooled-recuperated turbofans and combined-cycle turbofans (CC-TF). The CC-TF configuration combines the gas Brayton cycle with a bottoming Organic Rankine Cycle (ORC), which harvests thermal energy from the hot exhaust of the gas turbine and converts it into additional power to improve engine efficiency.

To meet the heat rejection requirements associated with a CC-TF engine concept, a solution can be to place the condenser after the fan in the bypass duct to receive a large quantity of cool airflow serving as a heat sink [4]. Studies have shown that this process not only has the potential to increase the efficiency of the engine but also reduce fuel consumption and lower emissions [5]. Figure 1.1 shows a simplified process flow diagram of the ORC bottoming unit.

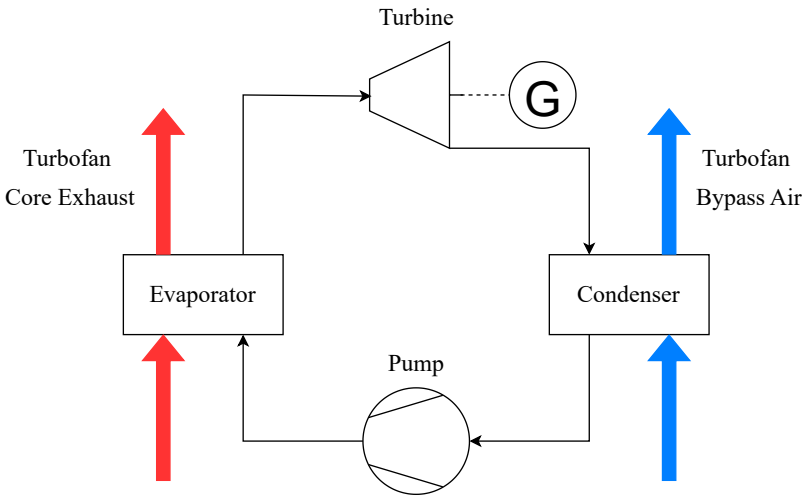

Figure 1.1: Simplified process flow diagram of the ORC unit of the CC-TF engine concept.

The main challenge associated with integrating a heat exchanger (HEX) within the bypass duct of the engine is designing the HEX and duct in such a way to introduce the lowest drag penalty possible,

to maximise the propulsive efficiency and reduce fuel consumption. The research by van Dongen [6] used a lumped parameter model to assess the aerodynamic performance of a HEX in a ram-air duct, specifically the condenser of a CC-TF. The model was compared with CFD simulations of the HEX and ducts. However, the study only focuses on the internal aerodynamics of the duct and does not incorporate the effects of the upstream air intake and fan. Similarly, other studies have also explored the possibility of integrating a HEX in the bypass duct using CFD simulations [7, 8, 9, 10]. Despite the insights provided by these studies, none have simulated the the airflow around an engine that features a HEX placed inside the ram air duct.

Therefore, ANSYS Fluent CFD simulations of the turbofan geometry will be performed with an integrated HEX in the bypass duct to determine and optimise its aerodynamic performance. The heat exchanger is modelled using a porous media model, which approximates the flow resistance and pressure drop caused by the HEX matrix without explicitly resolving its detailed fin structure. The fan is modelled using an actuator disk approach, simulating the pressure jump across the fan plane without resolving individual blade geometries. The computational domain is illustrated diagrammatically in Figure 1.2.

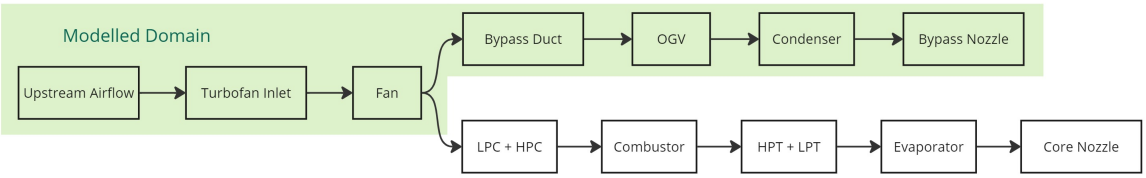

Figure 1.2: The components of a CC-TF modelled within CFD domain for this analysis.

This literature study aims to present up-to-date, relevant research regarding the setup of these CFD simulations and identify the knowledge gap. Chapter 2 focuses on the theory and setup of porous media models in literature and HEX integration effects. Chapter 3 summarises different approaches to modelling the turbofan geometry and flow interaction. Chapter 4 provides an overview of different optimisation and parametrisation methods that can be employed in the CFD simulations. With these topics covered, the findings are summarised and the research question and thesis scope are outlined in the Conclusion.

2

Heat Exchanger Modelling in CFD

CFD has become an important tool for modelling heat exchangers. These simulations predict pressure drops, heat transfer and turbulence, reducing the need for costly wind tunnel simulations. This chapter explores the fundamentals of HEX modelling in CFD, first identifying the type of HEX to be modelled, then focusing on the porous media method to simulate the presence of the HEX in a simplified manner and its assumptions, benefits and limitations. Finally, the effects of integrating the HEX in the bypass duct are considered.

2.1. Introduction to Aircraft Heat Exchangers

As a first step, it is important to determine the exact HEX thermal and geometrical properties to be used as inputs in the CFD model. Aircraft deploy different types of HEX depending on the coolant medium, the airflow velocity, and other parameters. This section categorically deduces the type of condenser required and explains the physics involved.

2.1.1. Types of Heat Exchangers

The HEX analysed in this literature study is a condenser of the CC-TF engine, and in this application the heat transfer happens primarily through convection of the cold bypass air rather than through radiation. The working fluid in the condenser undergoes a phase change and does not mix with the cold air. Three classifications further specify the characteristics of the considered HEX [11]:

Surface compactness: This is the ratio of heat transfer surface area over the HEX volume and is defined by the parameter β, which has units $[m^2/m^3]$. Due to the space constraints of fitting the condenser inside the bypass duct, it is advantageous to have a compact HEX since this reduces the required cross-sectional area and HEX thickness. A compact HEX also ensures sufficient structural support and can result in reduced overall weight, although it often comes with the penalty of increased airflow pressure losses. A HEX is defined as compact when $\beta \geq 700\, m^2/m^3$.

Construction features: Various condenser constructions can be employed to obtain an efficient, compact design. Extended surface heat exchangers use fins to increase surface area without significantly increasing the occupied volume. The fins increase the heat transfer surface area exposed to the bypass airflow, which in turn increases heat transfer. Due to their suitability for this application, different extended surface heat exchanger geometries can fulfil the objectives of a CC-TF condenser.

Plate-fin heat exchangers (PF-HEXs) have a core consisting of rows of plates or parting sheets separated by fins. The plates are connected at either end by sidebars or headers, where heat can be transferred from the working fluid. The design of PF-HEXs can be highly customisable to match the airflow velocity and direction; as such, they are commonly used for aircraft environmental control systems (ECS) and oil cooler applications [12] [13].

Tube-fin heat exchangers (TF-HEXs), on the other hand, use round or rectangular tubes to transport the working fluid, while extended surfaces (fins) surround the tubes to increase heat transfer. An advantage

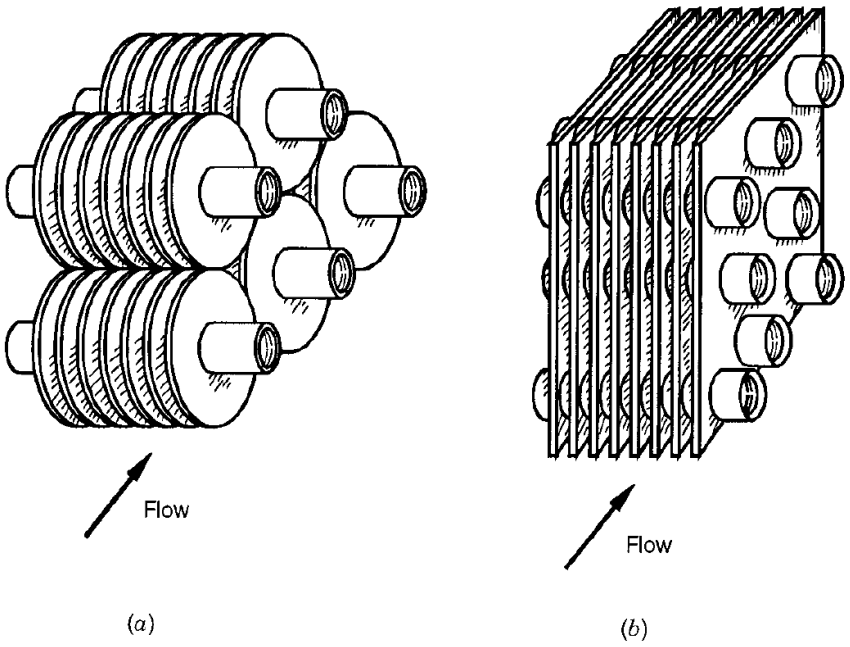

Figure 2.1: Geometries comparison between (a) tube-fin and (b) plate-fin heat exchangers, from [11].

of this heat exchanger is that many different fin geometries and sizes can be chosen to optimise heat transfer or minimise pressure losses. TF-HEXs can also handle large flow volumes of the working fluid and are relatively easy to manufacture, and so are also employed in the aviation industry [11] [9].

Flat-tube heat exchangers (FT-HEXs) are similar in that they are comprised of extended surfaces but utilise flattened tubes where coolant can flow through instead of rounded or square tubes. The flat tubes maximise the heat transfer area on the hot fluid side while minimising obstruction to the air-side flow. Hence, this type of heat exchanger is commonly used in automotive and aerospace radiators and condensers [14] [11].

Microchannel heat exchangers are an advanced solution for high-efficiency heat exchange. The tubes are composed of tiny, parallel channels to maximise the heat transfer surface area while minimising size and weight. Microchannel designs are characterised by their ability to offer excellent thermal performance in a compact footprint. This makes microchannel HEXs ideal for aerospace applications, particularly when space constraints and weight reduction are top priorities.

While other types of heat exchangers, such as shell-and-tube heat exchangers, have also been successfully employed as condensers and modelled using porous media in CFD [15], these are less practical to implement inside a turbofan bypass duct and are therefore not considered for this research.

Due to its advantages, the flat-tube microchannel heat exchangers (FT-MC-HEXs) are particularly suited for applications in CC-TF engines, where thermal efficiency and weight minimisation are paramount. FT-MC-HEXs can achieve a compactness of $\beta = 1000\, m^2/m^3$ and higher while suiting the phase change of the working fluid. Using louvred fins can promote the flow mixing and boundary layer disruption, leading to a two- to fourfold increase in the heat transfer coefficient with respect to a conventional fin geometry [11]. Therefore, the chosen heat exchanger type is a flat-tube microchannel heat exchanger with louvred fins. Figure 2.2 illustrates this geometry and the direction of airflow passing through.

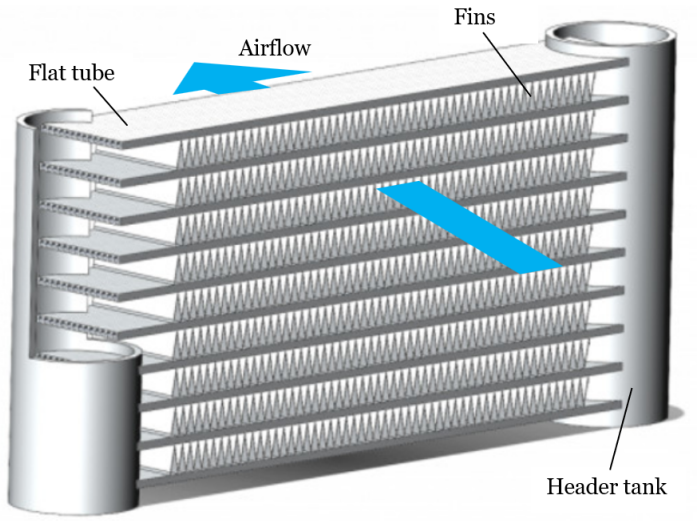

Figure 2.2: A flat tube microchannel heat exchanger geometry, adapted from [16].

Flow arrangement: The final classification criterion for heat exchangers is the relative flow directions of the fluids involved. In this study, the airflow of the bypass duct must pass straight through the heat exchanger to the bypass duct nozzle and out of the engine with as little pressure loss as possible to effectively produce thrust. However, there are multiple options for working fluid flow arrangements. In a multi-pass HEX, the working fluid flows through one full length of the heat exchanger after which the flow reverses and traverses in the opposite direction again. If the fluid only travels the length of the heat exchanger once and exits through the opposite header tank, it is called a single-pass heat exchanger. A multi-pass arrangement results in a greater pressure drop on the working fluid side, but this is accompanied by a slight increase in total heat transfer compared to a single-pass arrangement due to the increased working fluid flow velocity through the condenser.

The flow arrangement between the airflow and the working fluid of the condenser is of the cross-flow type. In the case of a pure condenser where the working fluid temperature remains constant during the phase change, this cross-flow configuration does not result in significant temperature non-uniformities at the outlets of either flow stream.

2.1.2. Working Principles of Condensers

Condensers are HEXs in which the working fluid enters the core in the vapour state and exits as a liquid. Due to this phase change, different modelling equations apply compared to single-phase working fluids. Condensers have larger working fluid-side heat transfer coefficients compared to single-phase HEXs thanks to latent heat transfer during the phase change.

Figure 2.3 illustrates a temperature-entropy (T-S) diagram of the working fluid passing through the condenser. In pure condensers, the working fluid enters as saturated vapour at point B and exits as a saturated liquid at point C, represented by a horizontal line on the graph. The working fluid analysed in this study exhibits no temperature glide, therefore the temperature remains constant during the phase change while entropy decreases due to latent heat removal.

If the working fluid enters the condenser in a superheated state – point A in Figure 2.3 – it requires an initial desuperheating stage to reduce its temperature to the saturation point. Once condensation is complete, some degree of subcooling may also occur as the working fluid exits as a liquid below its saturation temperature.

Changes in the thermodynamic state of the working fluid directly impact the local heat transfer coefficient. During the condensation phase, the release of latent heat enables high heat transfer rates. However, the desuperheating and subcooling phases rely more heavily on sensible heat transfer, resulting in lower heat transfer coefficients. Furthermore, in condensers the temperature pinch point often occurs at the beginning of the condensation process of the saturated liquid, potentially limiting the rate of

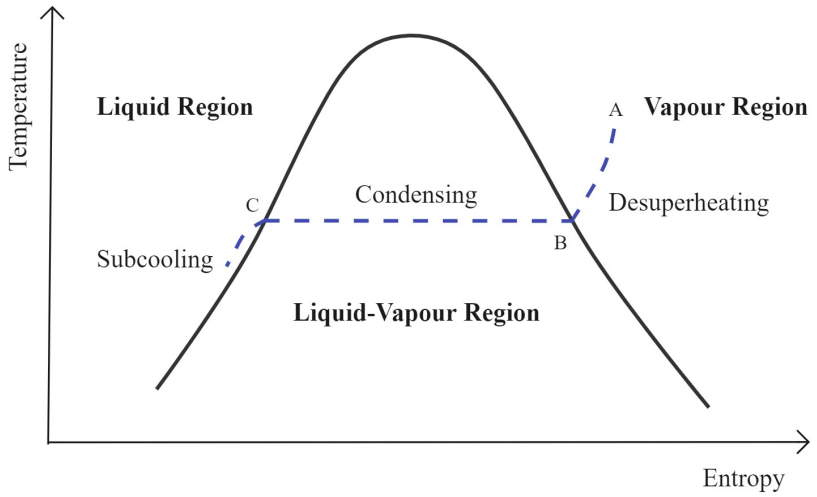

Figure 2.3: The T-S diagram of the working fluid passing through the condenser

heat transfer at this point [11]. At the temperature pinch point, the temperature difference between the bypass air and the working fluid is formulated as

$$(T_h - T_c) \ll (T_{h,i} - T_{c,o}) \text{ or } (T_{h,o} - T_{c,i})\,. \tag{2.1}$$

Figure 2.4 plots the temperature profiles of the hot and cold side fluids, as well as the temperature pinch point.

A critical assumption made in the modelling of condensers is that the wall temperature remains constant throughout the heat exchanger. The uncertainty of the results introduced by this assumption depends primarily on the degree of desuperheating observed in the condenser. Figure 2.5 illustrates the variation in wall temperature along the length of the condenser. During the desuperheating phase, the wall temperature is higher, reflecting the higher temperatures of the superheated vapour. As condensation begins, the wall temperature temporarily dips due to a delay in heat conduction caused by the coolant flow and wall material properties. This "catch-up" effect results in a slight positive temperature gradient along the wall before stabilising.

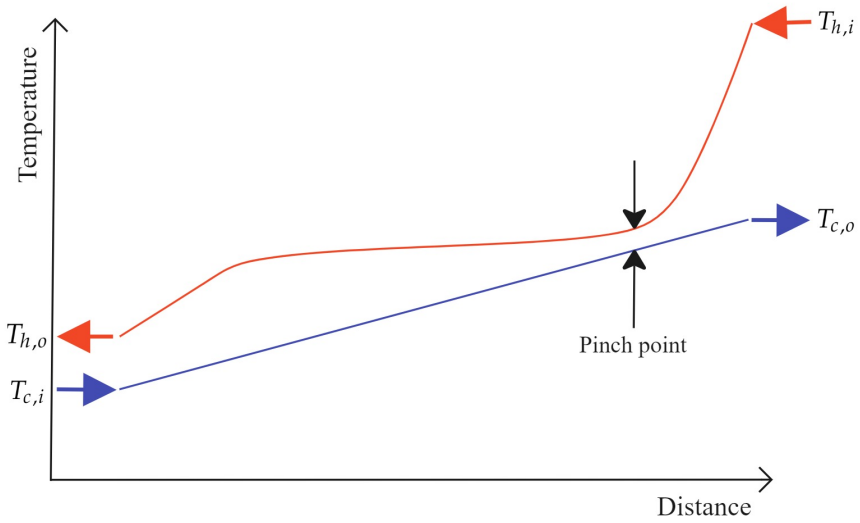

Figure 2.4: Sketch of the hot and cold side fluid temperature profiles and the resulting pinch point.

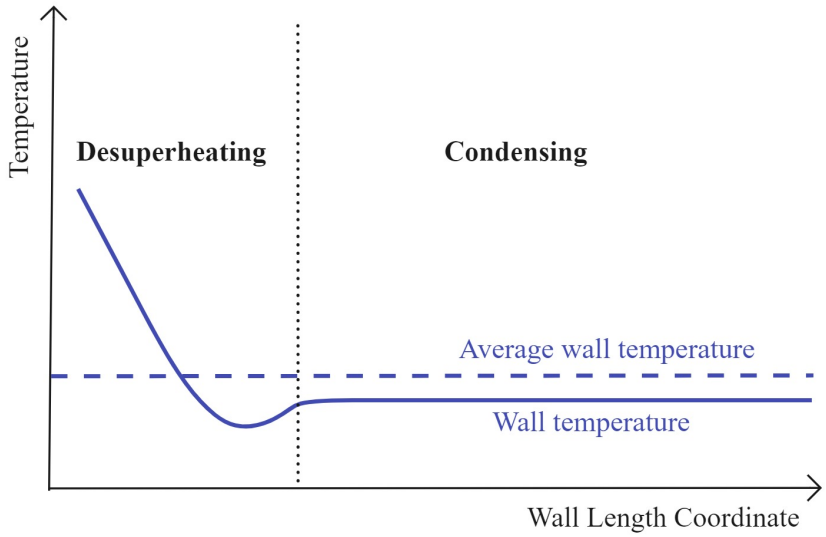

Figure 2.5: Variation of the condenser wall temperature along the path travelled by the working fluid

In this study, the wall temperature is assumed as an average value for modelling purposes, considering the desuperheating, condensation, and subcooling phases. While the desuperheating phase can significantly affect the temperature profile due to larger temperature reductions, the subcooling phase generally has a smaller effect, as the temperature drop in this region is less pronounced.

2.2. Porous Media Model of the Heat Exchanger

The accurate modelling of heat exchanger geometries in CFD is challenging due to the intricate geometries of small tubes and fins, resulting in a large number of mesh elements. A common approach to simplifying the detailed geometry of a HEX is to use a porous media model (PMM) in the volume that the HEX would otherwise occupy. The use of a PMM is an efficient method to replicate the flow and heat transfer characteristics of the HEX without resolving every small feature of the physical geometry, such as the individual fins and tubes, which would otherwise result in a highly complex and computationally expensive mesh.

A porous medium is any material that contains pores or voids for a fluid to occupy and flow through. Several studies have used porous media modelling in CFD to analyse soil, fences, and filtration devices. However, the presence of HEXs has also been successfully modelled previously, and this section will elaborate on the method used to approximate the airflow characteristics inside a HEX core.

Porosity ε is a fundamental property of porous media, describing the fraction of the total volume of a material that consists of void space. It is a dimensionless quantity crucial for understanding fluid flow through a porous media. Mathematically, porosity is defined as

$$\varepsilon = \frac{V_p}{V_t} \tag{2.2}$$

where V_p is the volume occupied by pores while V_t is the total volume of the porous zone. As the flow passes through the porous material will experience a reduction in cross-sectional area to pass through and therefore increase in velocity. This velocity increase is inversely proportional to ε and is expressed as

$$\vec{v}_{\text{physical}} = \frac{\vec{v}_{\text{superficial}}}{\varepsilon} \tag{2.3}$$

where $\vec{v}_{\text{physical}}$ is the airflow velocity occurring inside the porous media, while $\vec{v}_{\text{superficial}}$ is the velocity the flow would have had without the solid matrix present. The physical velocity-based formulation is

used for subsequent porous zone calculations in Ansys Fluent, as it captures the acceleration of flow through the HEX core resulting in a better approximation its influence on the upstream and downstream flow fields. Since the entrance and exit effects are strongly dependent on the local flow velocity, the physical velocity formulation enables a more accurate representation of those phenomena. Additionally, the pressure loss calibration for the porous zone is based on the flow velocity through the HEX core, as described in more detail in Subsection 2.2.2.

2.2.1. Modelling of Porous Zones in CFD

Inside the porous zone, the momentum and energy equations are modified to account for the pressure losses and heat transfer through the use of source terms.

Momentum Equation Source Term

To accurately simulate the heat exchanger pressure drop, the conservation of momentum equation must be adjusted to include additional source terms simulating the presence of the heat exchanger. The conservation of momentum equation can be formulated as

$$\frac{D}{Dt}(\rho\vec{v}) = -\nabla p + \nabla\cdot\bar{\bar{\tau}} + \rho\vec{g} \tag{2.4}$$

where the terms on the right-hand side (RHS) of the equation represent the three main types of forces acting on a fluid element: pressure, viscous and body forces, respectively. The viscous term is calculated using the stress tensor $\bar{\bar{\tau}}$, which is given by

$$\bar{\bar{\tau}} = \mu\left[\left(\nabla\vec{v} + \nabla\vec{v}^{T}\right) - \frac{2}{3}\nabla\cdot\vec{v}I\right]. \tag{2.5}$$

The additional source term $\vec{S}_m$ representing the momentum loss of the airflow through the heat exchanger is now introduced on the RHS of Equation 2.4. Next to that, the rate of change of momentum per unit volume on the left-hand side (LHS) of the equation is split into a local change of momentum with time and a change due to convection:

$$\frac{\partial}{\partial t}(\rho\vec{v}) + \nabla\cdot(\rho\vec{v}\vec{v}) = -\nabla p + \nabla\cdot\bar{\tau} + \rho\vec{g} + \vec{S}_m\,. \tag{2.6}$$

The momentum equation can be applied to a 2D axisymmetric simulation by using a cylindrical coordinate system, resulting in a set of two equations [17]:

$$\begin{aligned}\frac{\partial}{\partial t}\left(\rho v_x\right) + \frac{1}{r}\frac{\partial}{\partial x}\left(r\rho v_x v_x\right) + \frac{1}{r}\frac{\partial}{\partial r}\left(r\rho v_r v_x\right) = &-\frac{\partial p}{\partial x} + \frac{1}{r}\frac{\partial}{\partial x}\left[r\mu\left(2\frac{\partial v_x}{\partial x} - \frac{2}{3}(\nabla\cdot\vec{v})\right)\right] \\ &+ \frac{1}{r}\frac{\partial}{\partial r}\left[r\mu\left(\frac{\partial v_x}{\partial r} + \frac{\partial v_r}{\partial x}\right)\right] + S_{m_x}\end{aligned} \tag{2.7}$$

$$\begin{aligned}\frac{\partial}{\partial t}\left(\rho v_r\right) + \frac{1}{r}\frac{\partial}{\partial x}\left(r\rho v_x v_r\right) + \frac{1}{r}\frac{\partial}{\partial r}\left(r\rho v_r v_r\right) = &-\frac{\partial p}{\partial r} + \frac{1}{r}\frac{\partial}{\partial x}\left[r\mu\left(\frac{\partial v_r}{\partial x} + \frac{\partial v_x}{\partial r}\right)\right] \\ &+ \frac{1}{r}\frac{\partial}{\partial r}\left[r\mu\left(2\frac{\partial v_r}{\partial r} - \frac{2}{3}(\nabla\cdot\vec{v})\right)\right] \\ &- 2\mu\frac{v_r}{r^2} + \frac{2}{3}\frac{\mu}{r}(\nabla\cdot\vec{v}) + \rho\frac{v_z^2}{r} + S_{m_r}\end{aligned} \tag{2.8}$$

where v_x, v_r, and v_z are the flow velocities in axial, radial, and swirl directions, respectively.

The momentum source term is expressed in terms of force per unit volume $[N/m^3]$ and captures the pressure losses of the flow across the porous zone. The key governing equation for fluid flow in porous media is derived from Darcy's law [18], which expresses the water pressure gradient over a section with length L as

$$\frac{\nabla P}{L} = \left(\frac{1}{k_h}\right)v \tag{2.9}$$

where the LHS of the equation is the pressure gradient per unit length travelled by the flow through the porous media, while k_h is the hydraulic conductivity.

While this equation is valid for water and other incompressible and isothermal flows, the equation must be modified to be valid for air. Therefore, the dynamic viscosity μ is employed, resulting in

$$\frac{\nabla P}{L} = \left(\frac{\mu}{K}\right) v \,. \tag{2.10}$$

Equation 2.10 is known as the Hazen-Darcy equation, and introduces the specific permeability K of the porous zone. However, the relation only holds for flows with a very small velocity, and for velocities above around $1m/s$ the Darcy-Forchheimer equation is relevant which introduces a quadratic term that is proportional to velocity squared:

$$\frac{\nabla P}{L} = \left(\frac{\mu}{K}\right) v + \left(\frac{c_F}{\sqrt{K}}\right) \rho |v| v \,. \tag{2.11}$$

The coefficient c_F is the Forchheimer coefficient, also known as the inertial coefficient.

Equation 2.11 can be reformulated as

$$\vec{S}_m = \frac{\nabla P}{L} = \mu \mathbf{D} \vec{v} + \frac{\rho}{2} \mathbf{F} |\vec{v}| \vec{v} \tag{2.12}$$

for a 3D anisotropic porous zone, where the elements of matrices **D** and **F** are adjusted to vary the pressure gradient of the flow in each direction.

Energy Equation Source Term

Similar to the momentum equation, a source term can be added to the energy equation to simulate heat exchange due to the condenser. The energy equation is formulated as

$$\frac{\partial}{\partial t} \left(\rho E\right) + \nabla \cdot \left(\vec{v} \left(\rho E + p\right)\right) = \nabla \cdot \left(k \nabla T + \left(\bar{\tau} \cdot \vec{v}\right)\right) \,. \tag{2.13}$$

The terms on the LHS of the equation are:

- $\frac{\partial}{\partial t}(\rho E)$: Rate of change of energy density
- $\nabla \cdot (\vec{v}(\rho E + p))$: Convective transport of energy, including pressure work.

Meanwhile, on the RHS of the equation, the following terms are present:

- $\nabla \cdot (k \nabla T)$: Heat conduction, with k as the thermal conductivity of the fluid.
- $\nabla \cdot (\bar{\tau} \cdot \vec{v})$: Viscous dissipation, representing the work done by internal friction forces.

Quintard [19] introduces the nomenclature for different phases, with a β-phase being the fluid travelling through the σ-phase structure. Therefore, in the case of a heat exchanger, the β-phase is the airflow passing through it, while the σ-phase is the solid metal structure of the heat exchanger itself. The equation can be split into the contribution of each phase to the energy balance, resulting in Equation 2.14. At this step, the energy source term $\vec{S}_e$ is added to the RHS of the equation, resulting in

$$\frac{\partial}{\partial t} \left(\varepsilon \rho_\beta E_\beta + (1-\varepsilon) \rho_\sigma E_\sigma\right) + \nabla \cdot \left(\vec{v} \left(\rho_\beta E_\beta + p\right)\right) = \nabla \cdot \left[k_\beta \nabla T + \left(\bar{\bar{\tau}} \cdot \vec{v}\right)\right] + \vec{S}_e \,. \tag{2.14}$$

The rate of change of energy density has contributions from both the σ and β phases, while the convective term is dependent solely on the β-phase since the solid phase does not contribute to bulk convection.

The heat conduction term on the RHS of the equation is dependent on the fluid thermal conductivity k_β. By contrast, Musto [14] introduces the thermal conductivity to be a weighted average of the solid thermal conductivity k_σ and fluid thermal conductivity k_β according to

$$k_{\text{eff}} = \varepsilon k_\beta + (1-\varepsilon) k_\sigma \,. \tag{2.15}$$

However, if this is implemented into the energy equation and employed in a CFD simulation, the thermal conduction will be greatly overestimated by the CFD software, resulting in heat from the condenser conducting upstream. In reality, the thermal conductivity of the solid is highly localised within the porous media itself, and the overall thermal conductivity is determined almost exclusively by the fluid. Hence, only the fluid conductivity k_β is introduced in the energy equation while the solid thermal conductivity k_σ is neglected.

The energy source term is equivalent to the local volumetric heat flux

$$q_{\text{local}} = h_{\text{local}} \, (T_{\text{wall}} - T) \, \beta_{\text{HEX}} \tag{2.16}$$

where h_{local} is the local heat transfer coefficient, T_{wall} is the temperature of the heat exchanger wall in contact with the airflow, T is the local airflow temperature and β_{HEX} refers to the heat exchanger surface area density, defined as

$$\beta_{\text{HEX}} = \frac{A_s}{V_{\text{HEX}}} \, . \tag{2.17}$$

As explained in Section 2, T_{wall} is assumed to be constant for the whole porous zone. This assumption does not introduce significant errors, as the HEX being analysed is a condenser. β_{HEX} is also assumed constant over the volume of the condenser since the small local changes in geometry are neglected. The local heat transfer coefficient h_{local} depends on the local flow conditions and thermal properties of the fluid according to

$$h_{\text{local}} = \frac{k_\beta \, Nu}{D_{\text{eq}}} \tag{2.18}$$

reformulated from the definition of the Nusselt number Nu. In Equation 2.18, D_{eq} is the hydraulic diameter of the louvred fin geometry, calculated through

$$D_{\text{eq}} = \frac{4A_0}{P} \tag{2.19}$$

where A_0 is the cross-sectional flow area of the air conduit bounded by the louvred fins and flat tubes, while P is the wetted perimeter of the conduit.

As established, the Nusselt number Nu represents the convective to conductive heat transfer ratio. However, Nu can also be found using an empirical relation of the form

$$Nu = a \, Pr^m \, Re_{D_{\text{eq}}}^n \, . \tag{2.20}$$

The Reynolds number Re is based on the hydraulic diameter length scale D_{eq}, while the coefficients a, b and n are selected to approximate the thermohydraulic performance of the HEX core.

Linking Equations 2.16 – 2.20 together results in an expression for the energy source term solely in terms of predefined coefficients and local flow properties, expressed as

$$S_e = q_{\text{local}} = \frac{k_\beta a Pr^m Re_{D_{\text{eq}}}^n \, (T_{\text{wall}} - T) \, \beta_{\text{HEX}}}{D_{\text{eq}}} \, . \tag{2.21}$$

2.2.2. Key Parameters and Assumptions

The porous media model of the condenser requires several input parameters. The porosity of the heat exchanger ε significantly affects the pressure drop and aerodynamic efficiency of the system. For this study, a porosity value of 0.77 is chosen, obtained from the optimised condenser of a CC-TF engine concept from the research of Krempus [20].

To calibrate the pressure drop characteristics of the porous media, the matrices **D** and **F** from the momentum source term in Equation 2.22 are determined using HeXaCode, an in-house developed tool for the rating and sizing of heat exchangers. HeXaCode has been successfully verified through comparison with commercial code and has been employed in prior research, such as the work by Beltrame et al. [21]. The heat exchanger rating function is relevant for this research, for which HeXaCode calculates the temperature and pressure of both the hot stream and cold stream at the exit of the

condenser for a fixed heat exchanger area and geometry. HeXaCode generates a quadratic calibrated pressure drop relation, which is inputted into Ansys Fluent using a viscous resistance coefficient C_1 and an inertial resistance coefficient C_2 according to

$$\vec{S}_m = C_1\vec{v} + C_2\frac{\rho}{2}|\vec{v}|\vec{v}\,. \tag{2.22}$$

The coefficients a and n, used in the Nusselt number relation in Equation 2.20, are calibrated through the HeXaCode sizing function for a CC-TF condenser. The coefficient m is set to 0.33, a commonly used value found in the research by Sieder and Tate [22].

A key assumption made in the formulation of the porous media model is that the pore-scale characteristic lengths l_β and l_σ are much smaller than the length of the heat exchanger L. This assumption is based on the geometry of the flat-tube microchannel louvred fins, where the individual fins are comparatively small. Therefore, the flow travels across the entire porous medium with localised effects at the millimetre scale averaged out in the model. This simplification enables efficient computation without sacrificing accuracy in predicting the aerodynamic and thermal performance of the heat exchanger.

2.2.3. Advantages and Limitations

The porous media model offers several advantages, particularly when modelling complex systems such as turbofan engines where detailed meshing of the heat exchanger geometry would be impractical. Three main advantages of a well-calibrated model are discussed here.

Reliable and Accurate Results: Previous studies from Musto [14], Missirlis [9] and Hooman [23] among others, have validated that reliable results can be obtained for a heat exchanger integrated within an aero engine, with good correlation to heat exchanger modelling software and experimental results.

Reduced Computational Cost: By simplifying the detailed microchannel and fin geometry, the porous media model significantly lowers the mesh element count and the computational resources required. Research by Halim et al. [24] found that simulating the coolant flow around a tube bundle as a porous zone reduced computational time by factor 9.

Reduced Modelling Time: The porous media model aims to capture the macro behaviour of the flow without needing resolution on the millimetre length scale. Therefore a detailed geometric CAD file or drawing of the condenser does not need to be made.

Flexibility: The model can be easily adjusted to represent different types of HEX by modifying the porosity and inertial loss coefficients. This flexibility makes it a powerful tool for simulating various heat exchanger designs in varying flow conditions [8, 14, 23] especially for a future optimisation study where multiple porosities are considered.

While the porous media model provides an efficient approach to simulating heat exchangers, several limitations must be taken into account. The model relies on certain assumptions, including a homogeneous distribution of resistance throughout the HEX and a simplified representation of heat transfer mechanisms. These assumptions may not fully capture the local variations in flow and temperature that occur within the detailed structure of the HEX core, particularly in regions of high complexity or where strong flow separation occurs.

Moreover, the porous media model relies on accurate and sufficient calibration data in order to replicate the flow behaviour through the HEX over a range of air mass flow rates, temperatures and pressures. This large amount of calibration data must be processed to extract the accurate porous zone momentum and energy source term parameters.

2.3. Heat Exchanger Integration in the Bypass Duct

The placement of the condenser inside the bypass duct can significantly affect the propulsive efficiency of the engine and the frontal area of the condenser. According to Drela [25], large drag penalties can occur when a HEX is not optimally installed in high-altitude aircraft. On the other hand, a well-designed HEX duct system can contribute positively to the net thrust produced by the engine using the Meredith effect [26]. These integration phenomena are discussed in this section.

2.3.1. Condenser Placement

The integration of the condenser into the bypass duct presents several design challenges. To balance aerodynamic performance, heat transfer efficiency, and practicality requires careful consideration of the placement and geometry of the condenser.

One of the primary design considerations is the geometry of the heat exchanger. Two configurations are possible: a segmented design and an annular design. The segmented configuration is straightforward to manufacture and facilitates easier maintenance and replacement. Its modular nature allows for rapid component swapping, making it advantageous from a servicing perspective. Missirlis [9] incorporates a segmented design into a porous media CFD analysis, with the turbofan exhaust nozzle divided into four quarters. This required a 3D axisymmetric simulation, with a quarter of the whole domain modelled, to capture the aerodynamics.

In contrast, the annular design provides superior aerodynamic performance, as it conforms to the circular geometry of the bypass duct, thus making better use of the bypass duct area and maximising the HEX frontal area. The disadvantages are mainly practical, with an annular design proving harder to manufacture and maintain. Patrao [10] considers an annular design and is therefore able to perform the analysis completely within a 2D axisymmetric domain, significantly reducing computational costs. Given the advantages of a simplified model and improved heat exchanger performance, the annular design is selected for this study.

Another critical factor in the integration of the condenser is its inclination angle within the bypass duct. This angle influences both the heat duty of the HEX and the aerodynamic characteristics of the flow. Tilting the heat exchanger allows for increasing its frontal area without affecting the diameter of the turbofan engine nacelle. However, beyond a 70-degree tilt, the pressure losses of the airflow through the condenser increase substantially [27]. Figure 2.6 illustrates the effect of the HEX inclination angle on the air-side pressure losses.

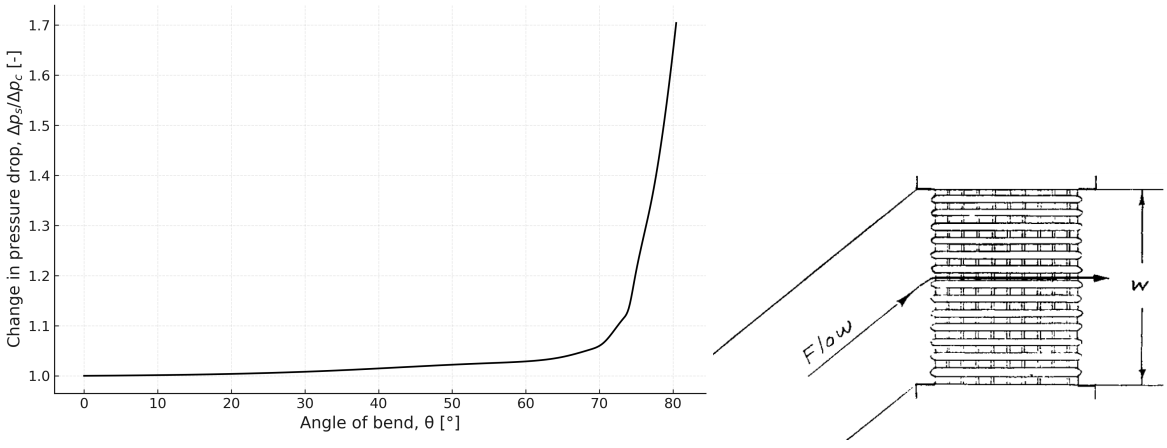

(a) Change in pressure drop with increasing heat exchanger angle

(b) Diagram of the airflow test case

Figure 2.6: Effect of changing the incoming flow orientation on the airflow pressure drop through a heat exchanger. Adapted from [27].

Practical constraints also play a role in defining the final design. These constraints include the positioning and orientation of other components within the turbofan engine, which impose spatial limitations and must be addressed when choosing the position of the condenser. These components include the thrust reverser system, air turbine starter, engine control module, fuel and air control systems, as well as the evaporator placed before the core airflow nozzle. Figure 2.7 shows a cross-sectional sketch of the CC-TF engine concept and highlights the spatial limitations of the bypass duct imposed by the surrounding key components.

2.3.2. Meredith Effect

The rejection of thermal energy into the cold air stream by means of a HEX increases the enthalpy of the flow. If the airflow is accelerated through a nozzle, part of the drag introduced by the HEX can be

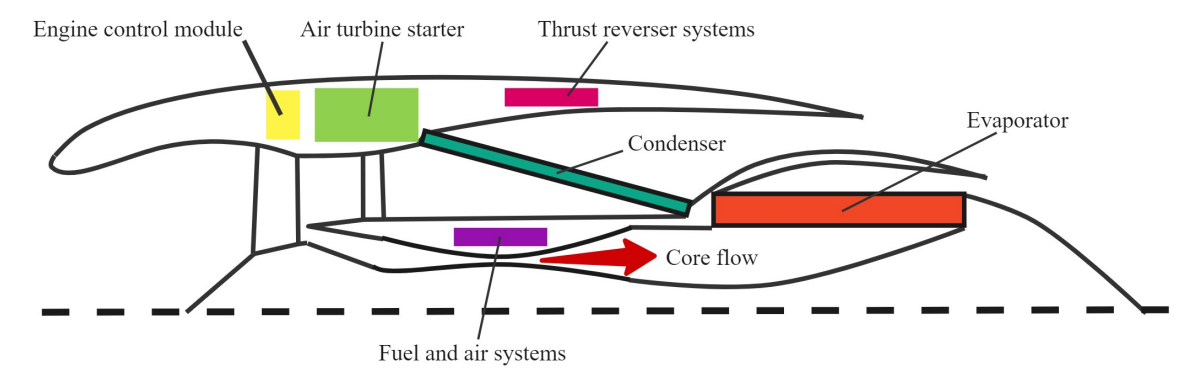

Figure 2.7: Illustration of a CC-TF engine concept, with the approximate positions of key turbofan components. Adapted from [20].

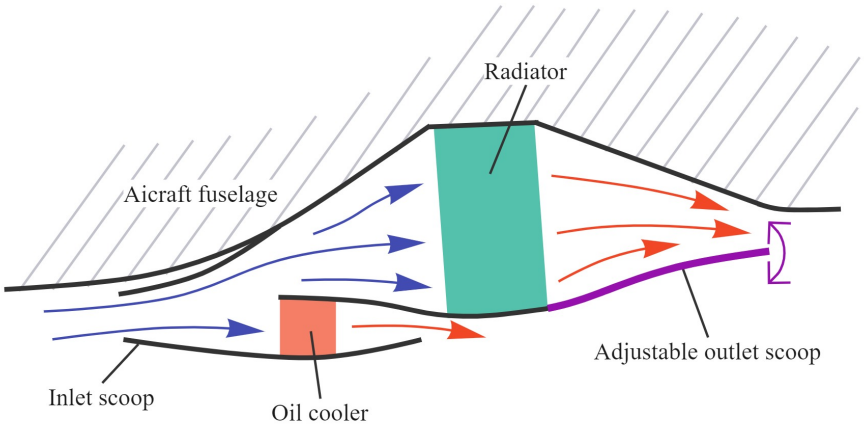

Figure 2.8: Diagram of the cooling solution of the P-51 Mustang. Adapted from [28].

recovered. This effect was studied by Meredith [26] in 1935 and most famously implemented in the North American Aviation P-51 Mustang, built in the 1940s. The aircraft has a ducted radiator placed underneath the body of the aircraft, which dissipates the heat produced by the piston engines. Figure 2.8 includes a diagram of the ducted radiator, featuring an adjustable outlet scoop in order to optimise the cooling performance for different aircraft speeds; at low speed, the outlet scoop is fully open to maximise airflow for cooling, while at cruise, the scoop moves upward to constrict the outlet and utilise the Meredith effect.

In a more recent example, Kaiser et al. [7] analysed an ultra-high bypass ratio (UHBPR) turbofan employing a Cheng cycle - a combination of a Brayton and Rankine cycle - for reduction of engine contrails, CO_2 and NO_x emissions. In this research, a condenser is also placed in the bypass duct in an annular configuration, with a similar integration to that shown in Figure 2.7. The study claims that the Meredith effect allows for producing enough thrust to compensate for the heat exchanger pressure drop during cruise conditions. The working fluid is water, resulting in condensation temperatures of around 373 K and approximately 1-2 MW of heat rejected to the bypass air [7, 29]. The potential for HEX drag recovery is promising, although it should be noted that the nacelle length had to be increased by 40% in the study by Kaiser et al. [7] to incorporate the condenser while retaining enough length for the bypass nozzle. This suggests that integrating the components for a combined-cycle turbofan into an existing nacelle design without adjusting its dimensions can prove to be one of the primary challenges of this research.

The fundamental equations modelling the Meredith effect are derived by Meredith [26] for incompressible flow through a ducted heat exchanger with no temperature increase. If A is the frontal area of the radiator with fixed thickness, V_∞ is the freestream airflow velocity, $V_\infty(1-a)$ is the velocity of the

airflow travelling through the heat exchanger, then the volume flow F is defined as

$$F = A\,V_\infty\,(1-a)\,. \tag{2.23}$$

Next, Δp_{HEX} is defined as the pressure drop through the heat exchanger and consequently, the power loss associated with this pressure drop is

$$E = F\,\Delta p_{\mathrm{HEX}} = \Delta p_{\mathrm{HEX}}\,A\,V_\infty\,(1-a)\,. \tag{2.24}$$

The pressure drop through the heat exchanger can be linked to the wake conditions. For this, the velocity of the duct exit flow rejoining the free airflow is introduced as $V_\infty(1-b)$. The pressure drop is expressed as

$$\Delta p_{\mathrm{HEX}} = q_\infty(1-(1-b)^2) \tag{2.25}$$

which can be rearranged to form the relation

$$\frac{\Delta p_{\mathrm{HEX}}}{q_\infty} = 2b(1-\frac{b}{2})\,. \tag{2.26}$$

Equation 2.26 demonstrates that $\Delta p_{\mathrm{HEX}}/q_\infty$ is equal to 1 when $b = 1$; in other words, the outlet wake velocity is equal to zero. For the equations describing the Meredith effect to be valid, there must be some airflow out of the duct exit and therefore $\Delta p_{\mathrm{HEX}}/q_\infty < 1$.

Meredith showed that the drag can be computed as the rate of change of momentum:

$$D = 2q_\infty Ab(1-a) \tag{2.27}$$

Thus, the power lost overcoming drag becomes:

$$E_D = 2q_\infty AV_\infty b(1-a) \tag{2.28}$$

Combining Equations 2.24 and 2.28 yields the following duct efficiency definition.

$$\eta_{duct} = \frac{E}{E_D} = \frac{\Delta p_{\mathrm{HEX}}}{2q_\infty b} \tag{2.29}$$

At this point, Equation 2.26 can be utilised to eliminate b and obtain:

$$\eta_{\mathrm{duct}} = \frac{1}{2}\frac{\frac{\Delta p_{\mathrm{HEX}}}{q_\infty}}{1-\left(1-\frac{\Delta p_{\mathrm{HEX}}}{q_\infty}\right)^{\frac{1}{2}}} \tag{2.30}$$

Figure 2.9 displays the variation in duct aerodynamic efficiency η_a as a function of $\frac{\Delta p_{\mathrm{HEX}}}{q_\infty}$ according to Equation 2.30. A small ratio of $\frac{\Delta p_{\mathrm{HEX}}}{q_\infty}$ results in improved duct aerodynamic efficiency. Meredith also showed that this efficiency is about 50% greater for a ducted radiator than a freely exposed radiator.

If the airflow compressibility and the heat addition are also factored into account, the duct efficiency can be positively affected. At the heat exchanger, the thermal energy is added at pressure p, after which the flow is expanded to the static pressure of the freestream airflow p_0. A portion of this thermal energy is converted to the kinetic energy of the airflow. This process can be measured according to the efficiency definition

$$\zeta = 1-\left(\frac{p_0}{p}\right)^{\frac{\gamma-1}{\gamma}} \tag{2.31}$$

The thermal energy recovery efficiency, therefore, increases if the heat is added at a higher pressure p or if the ambient static pressure p_0 is lower. It is advantageous to fly at a higher altitude, such that p_0 is reduced. The effect of altitude on the Meredith effect kinetic energy recovery can be found in Figure 2.10.

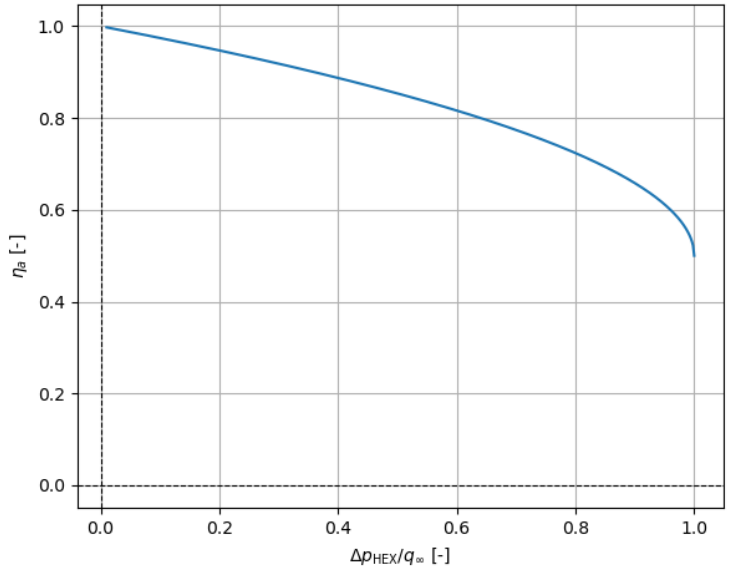

Figure 2.9: Induction efficiency of the duct as a function of the pressure drop to dynamic pressure ratio

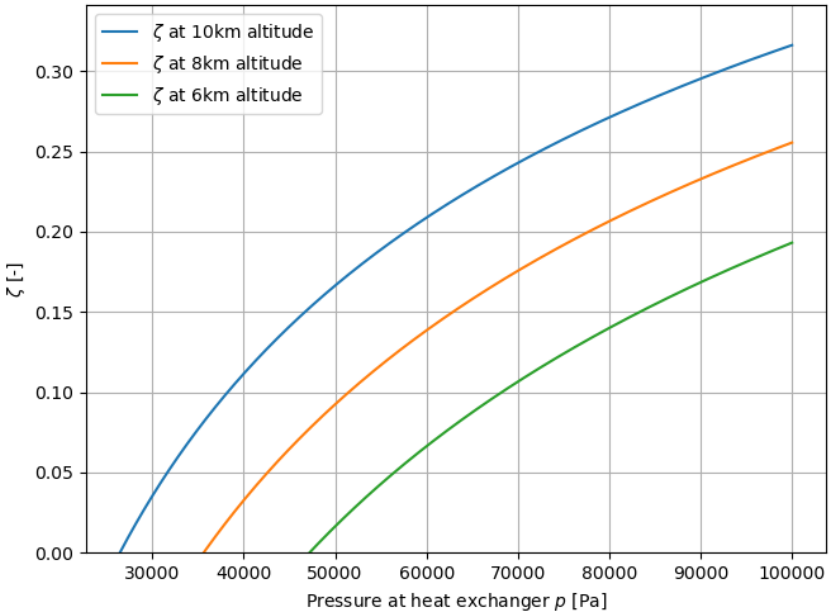

Figure 2.10: Kinetic energy recovery efficiency for different cruise altitudes

Meredith applied Equations 2.30 and 2.31 to a generic piston-powered aircraft to derive a relation of the heat recovered as kinetic energy E′ as a function of outside temperature T, engine brake horsepower (BHP), airspeed V_∞ and minimum airspeed to ensure sufficient cooling V_0. The resulting relation is

$$\mathrm{E}' = 0.16 \left(\frac{V\infty\,[\mathrm{mph}]}{100} \right)^2 \frac{288}{T} \left(1 - \frac{4}{3} \frac{V_0^2}{V^2} \right) \frac{\mathrm{BHP}}{100} \,. \tag{2.32}$$

In order to link the heat dissipated by the heat exchanger to the resulting drag of the heat exchanger core, Drela [25] devised a relation that takes into account the Meredith effect, formulated as

$$D_{\text{HEXcore}}\, V_\infty \simeq \frac{\dot{m}}{2} V_\infty^2 \frac{\Delta p_{\text{HEX}}}{q_1} \left(\frac{V_1}{V_\infty} \right)^2 - \dot{H} \frac{\gamma - 1}{2} M_\infty^2 \tag{2.33}$$

where $\dot{H}$ is the heat rejection rate, $\dot{m}$ is the air mass flow into the heat exchanger, and subscript 1 denotes conditions directly in front of the heat exchanger. Equation 2.33 highlights the benefit of slowing down the flow from V_∞ to a low V_1 to reduce the drag contribution due to the HEX air-side pressure drop. If $\dot{H}$ is made as large as possible, it is even possible to obtain a negative value for $D_{\text{HEXcore}}\, V_\infty$ as postulated by Meredith. The underlying assumption is that the duct shape is smooth to prevent flow separation, as the vorticity caused by separation would increase the apparent drag of the heat exchanger setup.

The research by Drela [25] aimed to successfully incorporate a heat exchanger into the wing of a subsonic aircraft. Consequently, the relations derived are not completely applicable to the case of a heat exchanger inside a turbofan engine as the pressure rise caused by the upstream fan must be taken into consideration. However, Equation 2.33 is still helpful as it highlights the parameters of importance and suggests that during the optimisation routine that will be performed in this research, the optimiser will seek to adjust the duct wall geometry to maximise the heat dissipation term and minimise the pressure drop term. Similarly to how the outlet scoop of the P-51 Mustang moves upward to increase the kinetic energy recovery of the hot air during cruise conditions, the optimised turbofan bypass duct nozzle will likely also have a narrower outlet opening with respect to the original geometry.

3

Turbofan and Flow Modelling in CFD

This section discusses the fundamentals of turbofan engine design and the modelling of the turbofan within the CFD environment. The actuator disk model is used for the simulation of the flow characteristics through the fan and OGVs and is presented in the following sections. The external aerodynamics phenomena around the engine nacelle are also introduced, which aids in creating a mesh and selecting CFD flow settings. Finally, methods for verifying and validating the turbofan model are discussed.

3.1. Turbofan Theory and Baseline Model

Turbofan engines are the most popular propulsion system choice in modern commercial aviation due to their high efficiency and ability to generate significant thrust while maintaining relatively low noise levels. One way of categorising these engines is by their bypass ratio, which refers to the amount of air bypassing the engine core compared to the air passing through the core. To understand the influence of bypass ratio on the engine performance, the propulsive efficiency definition [30] is introduced as

$$\eta_{\text{prop}} = \frac{2}{1 + \frac{v_e}{v_0}} \,. \tag{3.1}$$

Equation 3.1 illustrates that efficiency is maximised when the turbofan engine exhaust velocity v_e is as close as possible to the external airflow velocity v_0.

At the same time, designers aim to extract as much thrust from the engine as possible, expressed as

$$F = \dot{m}\,(v_e - v_0) \,. \tag{3.2}$$

In order to maximise both of these equations, an ample airflow $\dot{m}$ through the engine with a small flow acceleration $v_e - v_0$ is needed.

A practical solution to achieving a large $\dot{m}$ with a small $v_e - v_0$ is to increase the bypass ratio (BPR). A higher BPR indicates that a greater portion of the air flows through the bypass duct relative to the engine core, enabling a smaller acceleration of a larger mass flow. This design improves propulsive efficiency while simultaneously reducing noise emissions due to the lower exhaust velocity.

Historically, the bypass ratio has increased steadily in turbofan engines since their inception. Early turbofan engines, such as the Pratt & Whitney JT3D developed in the 1960s, featured a bypass ratio of approximately 1:1, categorising them as low-bypass engines. Modern high-bypass turbofans, such as the CFM LEAP-1A, achieve bypass ratios as high as 11:1, resulting in significant efficiency and environmental performance advancements. Figure 3.1 illustrates the progression of bypass ratio trends over the decades, emphasising the continual focus on optimising turbofan performance for both economic and ecological benefits.

To successfully incorporate the condenser into the bypass duct, the BPR is particularly relevant. A high-bypass ratio or UHBPR engine will provide enough airflow to meet heat dissipation targets while

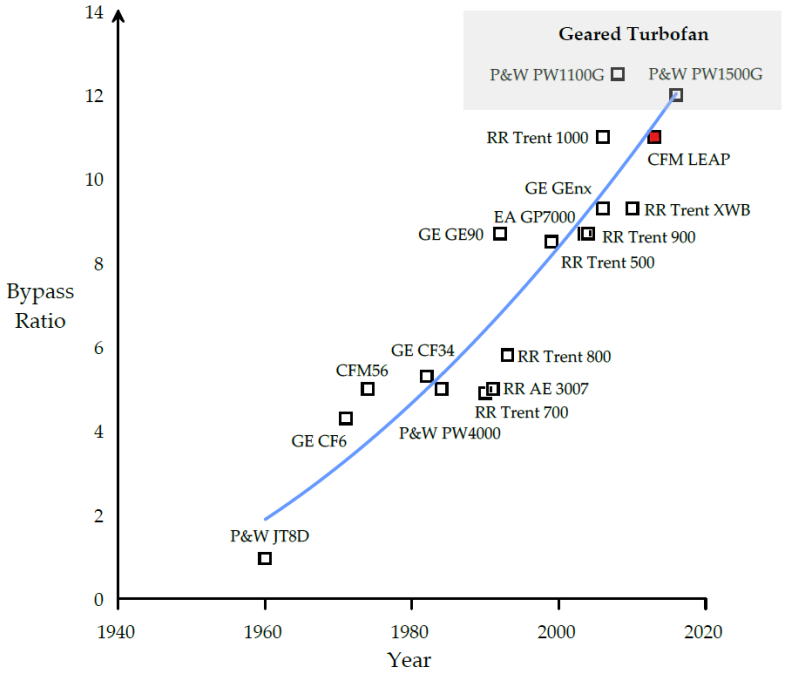

Figure 3.1: Historical trends in bypass ratio for turbofan engines from the 1960s to the present day, with the CFM LEAP engines highlighted in red. Adapted from [31]

maximising propulsive efficiency. The effect of the bypass ratio, as well as the other factors that influence the turbofan bypass flow performance and HEX integration, are summarised in Table 3.1 [32, 33].

Table 3.1: Important design considerations for a turbofan engine bypass duct.

Design Factor	Details and Implications
Bypass Ratio (BPR)	Ratio of air bypassing the core to air passing through the core. A Higher BPR increases bypass duct airflow, improving fuel efficiency and reducing noise.
Fan Pressure Ratio (FPR)	Ratio of fan discharge pressure to inlet pressure. A Higher FPR can enhance specific thrust but can result in increased bypass duct noise.
Geared vs. Direct-Drive Fans	**Geared Fans**: Allow the fan to rotate slower while the low-pressure turbine rotates faster, optimising bypass flow for efficiency. **Direct-Drive Fans**: Simpler design but less efficient at higher BPRs, as the bypass duct flow is not optimised.
Noise Reduction (Rotors, OGVs, Chevrons)	The rotor and outlet guide vanes (OGVs) blade design in the bypass duct significantly can significantly affect noise. Chevrons at the bypass duct exit can reduce jet mixing noise.
Aerodynamic Design of the Duct	The shape and size of the bypass duct influence flow efficiency and pressure losses. Minimising flow separation and turbulence improves fuel efficiency and reduces noise.

When selecting the baseline turbofan engine design to adapt into a CC-TF, the goal is to choose a modern turbofan engine for an aircraft serving short to medium-range aircraft. Additionally, information must be available on the geometry of the engine, as well as information on the design factors mentioned in

Table 3.1 and other performance metrics.

Ultimately, the LEAP-1A engine that serves the Airbus A320 series aircraft was chosen. It is a high bypass ratio engine that suitably represents current turbofan technology, and its performance characteristics are well documented. Important operating conditions for the LEAP-1A engine are listed in Table 3.2.

Table 3.2: Operating conditions and performance of the LEAP-1A Engine

Parameter	**Value**
Bypass Ratio	11:1
Cruise Altitude	10000 m
Cruise Mach Number	Mach 0.78
Maximum Thrust	147 kN (LEAP-1A Engine)

This engine offers a 15% fuel efficiency increase compared to the previous generation of aircraft engines, making it a suitable baseline model for adaptation to a CC-TF engine.

3.2. Actuator Disk Models

In the aerodynamic modelling of turbofan engines, accurately capturing the effects of the fan and OGVs on the airflow is crucial for understanding the overall performance of the engine. However, modelling the detailed geometry of the fan blades and outlet guide vanes can be computationally expensive, particularly in large-scale CFD simulations. To address this challenge, the actuator disk approach is often employed as a simplified method for modelling the fan and stator sections of a turbofan engine while capturing the essential flow effects, namely the pressure rise and velocity change of the airflow.

The actuator disk approach simulates the fan and OGVs as thin, permeable disks that exert forces on the passing airflow without explicitly resolving the geometric details of the blades or vanes. This method assumes that the fan and stator primarily impart momentum to the flow through a pressure discontinuity rather than through otherwise complex 3D flow interactions. The actuator disk method applied to steady-state CFD simulations simulates the flow behaviour of a hypothetical engine with infinite fan blades without time-dependent discontinuities. Although this is not the case in practice, it can be seen as a time-averaged representation of the flow through a real rotor or stator of an engine. Therefore, it is applicable to RANS CFD simulations [34]. This modelling method was used as early as 1920 by Froude [35] and has been improved upon since.

There are two approaches for an actuator disk model: adding source terms to the actuator disk region or imposing pressure jump as a boundary condition to the flow. Rajagopalan and Fanucci [36] first implemented the former method to model wind turbines, modelling the volume occupied by the spinning blades as a porous cylinder in which these momentum source terms are applied. The method can be used for both a disk of one control volume width and a wider region, allowing the entire rotor width to be modelled by an actuator disk and spreading the pressure rise over this volume. This more accurately portrays the actual behaviour of a fan and is therefore preferred over a pressure jump boundary condition, which is easier to implement but may lead to strong discontinuities in the flow [34]. The source term method is also more robust than imposing a pressure jump when introducing a swirl component to the airflow.

The momentum source terms are introduced to the flow similarly to the momentum loss in the porous media, as described in Equations 2.6, 2.7 and 2.8. Various methods are available to model the forces exerted on the flow by the rotor and OGVs; these are described in the Subsections 3.2.1 and 3.2.2 below.

3.2.1. Actuator Disk based on Blade Element Momentum theory

The first method of modelling the fan blades and OGVs stems from Blade Element Momentum (BEM) theory, in which a propeller or fan blade is broken down into a finite amount of airfoils stacked together. The inputs for this model are the airfoil geometries along several sections of the fan blade. For each airfoil section, the lift and drag coefficients C_L and C_D are computed over a range of angles of attack α. The forces are then integrated along the fan blade length to produce a force distribution, which can be converted to a momentum source term. The induced axial velocity u_a^* and tangential velocity u_t^* of

the blade are calculated using momentum theory, and the resulting airfoil cross-sectional analysis is shown in Figure 3.2. In this figure, v_∞ is the freestream velocity of the aircraft, and ωr is the tangential

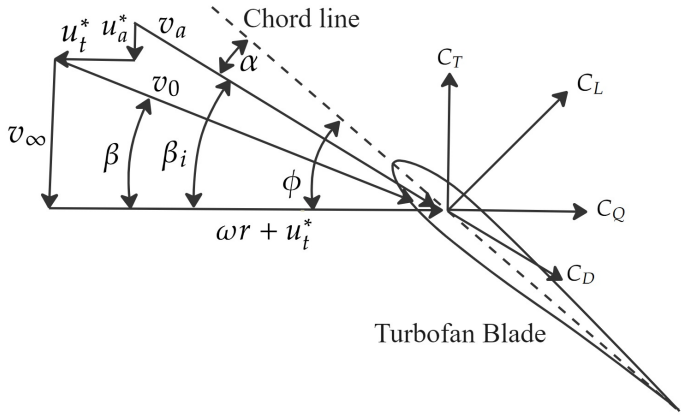

Figure 3.2: Velocity diagram of a fan blade according to BEM theory

velocity caused by the blade rotational velocity ω. The resulting airfoil velocity v_a is the addition of all these contributions, and as such, the force coefficients C_L and C_D are based on this reference axis, while the thrust coefficient C_T and torque coefficient C_Q utilise the aircraft frame of reference. β is the blade angle, β_i is the induced angle while ϕ is the pitch angle.

This method has been recently applied by Baratchi [37] to model a ducted tidal turbine using a 3D Detached Eddy Simulation (DES) setup. Similarly, Spinner et al. [38] incorporated this method to model a UHBPR fan and compare the source term actuator disk method to a full unsteady Reynolds-averaged Navier–Stokes (URANS) simulation. In their work, there was good agreement between the actuator disk method and the URANS simulations. However, the total pressure ratio $p_t/p_{t,\infty}$ and airflow swirl angles were underestimated towards the outer radial sections after the fan and OGVs. Towards the tip of the fan blade, the local flow velocity can approach or exceed transonic speeds, and the resulting compressibility effects are not considered. Additionally, tip vortices that form at the blade ends are not modelled, resulting in further uncertainties in the actuator disk model.

Another disadvantage of this model is that sufficient airfoil data is needed as an input, requiring a 3D geometry file of the fan and OGV blades. The airfoil geometries can be complex, and the twist introduced in the blade means that detailed geometric information is needed, while often data is only available on general engine parameters such as the fan pressure ratio. As this thesis aims to form a holistic method of modelling turbofan components, alternative modelling methods are considered.

3.2.2. Actuator Disk based on a Custom Disk Loading Profile

The thrust and tangential forces produced in the actuator disk zone can also be user-prescribed to fit a custom loading profile, varying along the blade radial position. This method is used by Stich et al. [34] to model the fan of NASA's Glenn Ultra High Bypass Drive Rig, a 1:5 scale jet turbofan model. The research compares different axial and moment loading profiles as a function of the blade radial distance. The first is a constant loading profile, representing the most simple actuator disk setup where the volumetric source term is the same everywhere in the disk. Next, a Goldstein thrust loading profile is considered, established in the work of Goldstein and Prandtl [39] and illustrated in Figure 3.3. This distribution of circulation along a propeller blade minimises the energy lost in the propeller slipstream, serving as a good foundation for modelling the thrust distribution. Lastly, custom load profiles generated from detailed URANS results are inputs for the simplified actuator disk method. Stich et al. [34] showed that all three methods can predict the overall mass flow rate, total pressure ratio, and total temperature ratio to within 1% accuracy. However, the exact velocity distributions at the OGV exit can differ from the experimental results. Their research also applied the same method to model the tangential momentum source terms according to different load distributions. Ultimately, this approach has been chosen since it can be applied more quickly to any turbofan engine by adjusting polynomial

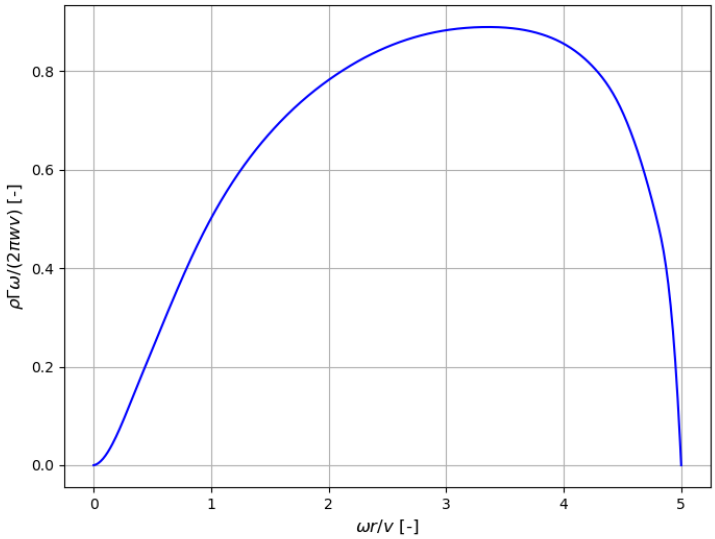

Figure 3.3: The Goldstein load distribution, showing the non-dimensional circulation as a function of the dimensionless rotational velocity ratio for a 4-bladed propeller. Adapted from [39]

Figure 3.4: NASA's Glenn UHBPR engine 1:5 scale model, from [40].

coefficients to achieve different loading distributions. Using polynomial equations as a function of the normalized radial distance

$$R = \frac{y - y_{\text{hub}}}{y_{\text{casing}} - y_{\text{hub}}} \tag{3.3}$$

allows Ansys Fluent users to define an expression of the momentum source term. In Equation 3.3, y is the y-coordinate of the cell element, y_{hub} is the y-coordinate where the fan blade attaches to the hub, and y_{casing} is the y-coordinate of the nacelle casing near the fan blade tip.

A drawback of modelling the fan and OGV using an axisymmetric RANS actuator disk model is that fluctuations in the thrust are not captured in the model. The thrust loading is not constant with the circumferential position; this is often because the turbofan inlet lip is more prominent on the bottom to prevent stalled flow at high angles of attack. This asymmetry affects the flow in a manner that cannot be captured in an axisymmetric simulation. Additionally, any time-wise fluctuations resulting from complex fan-nacelle interactions are not properly captured through RANS simulations. These limitations are deemed acceptable since the goal is to represent typical steady cruise conditions of the engine rather than model detailed flow phenomena.

3.3. External Aerodynamics

In addition to the internal flow within the turbofan engine, the external aerodynamics must be modelled accurately to ensure reliable simulation results. The aerodynamics of the turbofan intake can significantly affect the flow quality entering the engine; thus, the inlet and upstream effects are incorporated into the simulation. Several assumptions and simplifications of the airflow are made in the CFD environment, which also influences the accuracy of the results. These factors are discussed in this section.

3.3.1. Assumptions and Simplifications

As previously mentioned, a 2D axisymmetric geometry will be analysed to simplify the turbofan geometry. However, in reality the turbofans on commercial aircraft are not fully symmetric since the engine pylon and wing mounting affect the aerodynamics around the engine nacelle. The large bypass ratios of modern-day engines result not only in increased nacelle drag but also a bigger drag contribution from interference with the wing; previously, the engine installation drag penalty was estimated at 14% of the total aircraft drag [41], but this proportion increases as bypass ratios increase. Several works have investigated the precise influence of engine integration on flow uniformity and overall drag using CFD methods [41, 42, 43]. The critical assumption is made, however, that these asymmetrical effects will have little effect on the optimisation process of a turbofan bypass duct for heat exchanger integration since they primarily influence the external nacelle shape and placement of vortex generators. Therefore, these effects are not considered.

The engine pylon also extends inside the engine cowling, blocking a portion of the bypass duct airflow. Struts distribute the loads from the rotating components and add extra support to the engine structure. These struts are placed behind the OGVs in the bypass duct. Kodama and Nagano [44] investigate the effect of the pylon and struts on the fluctuations in pressure in the circumferential direction. Their research showed that it is possible to use an actuator disk to model the effect of the struts and pylon on the flow field by creating an equivalent influence through the OGVs, thereby reducing the computational time needed to model the struts and pylon. Figure 3.5 shows the effect of these struts, with more than 1% fluctuation from the average static pressure at an upstream location near the fan. While the actuator disk model can capture this effect well, it still requires a 3D computational domain and knowledge of the strut positions and geometry. Parry [45] similarly discovered that by varying the OGV shape along the circumferential direction, the effect of fluctuations can be reduced, once again needing a 3D simulation. While the effect cannot be captured in this research using an axisymmetric geometry, it is an important consideration for future 3D simulations of a bypass duct or when simulating noise generated by the turbofan.

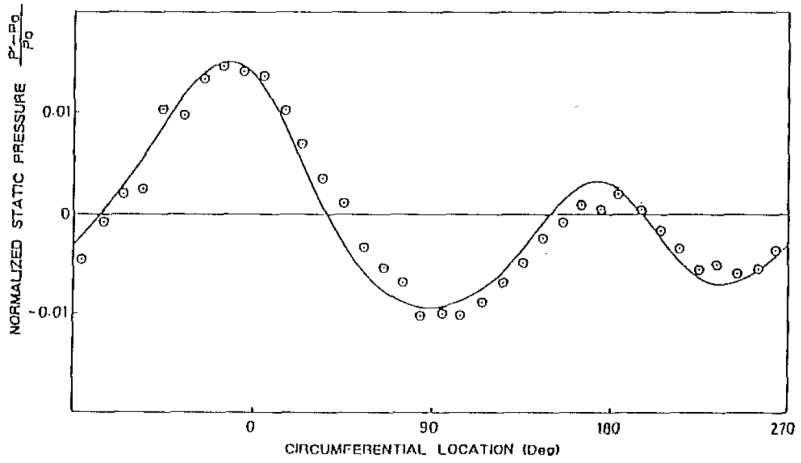

Figure 3.5: Perturbations in static pressure upstream of the struts, with measurements marked with dots and actuator disk calculations marked with the solid line. [44]

Another assumption that must be made is that the angle of attack of the turbofan engine, often referred to as inclination or incidence angle, is 0°. Typically, a turbofan engine is mounted at a slight negative angle with respect to the longitudinal axis of the aircraft to counteract the positive angle of attack of the

aircraft during cruise. However, there may still be a slight incidence angle with the airflow observed. In the simulations made by Spinner [38] an incidence angle of 3° is taken for cruise conditions, while Savelyev [46] utilises a −3° inclination for engines mounted on top of a blended-wing body (BWB) aircraft. Other studies like that of Mund and Pilidis [47] assume a 0° inclination angle since they also employ an axisymmetric CFD domain. These small angles should also not considerably influence optimisation results and can be considered an acceptable simplification.

3.3.2. Air Intake

The primary objective of the turbofan inlet is to condition the incoming airflow to achieve uniformity while minimising pressure losses. For a real turbofan engine, this involves balancing performance across various operating conditions, particularly between take-off, where the angle of attack can exceed 10°, and cruise. To prevent airflow stalling at high angles of attack, the bottom lip of the inlet is typically shorter and rounder than the top lip. However, due to the axisymmetric constraints of this study and a focus on cruise conditions, these anti-stall features are neglected. Instead a constant inlet shape is assumed, based on the shape at the top of the LEAP-1A engine nacelle.

During cruise, supersonic flow may develop on the exterior surface of the inlet, as demonstrated by the CFD results of Savelyev [46]. This region is particularly sensitive to geometrical variations, thus constructing the nacelle geometry in CFD using splines connected by sparse geometrical coordinates may not be accurate enough to represent the nacelle geometry. Robinson [48] proposed using CST coefficients to optimise the engine air intake design before performing further aerodynamic analyses of the engine. However, this method significantly increases the number of optimisation variables and is not central to integrating a heat exchanger in the bypass duct. Alternatively, Kaplan [49] employed a NACA 1-series airfoil profile to approximate the external surface of the turbofan inlet, producing sufficiently accurate results for the supersonic flow behaviour observed over the nacelle exterior surface.

Proper upstream modelling of the airflow is also critical for accurate intake aerodynamics. The engine captures a stream tube of air, where external diffusion occurs prior to the internal diffusion within the engine. Figure 3.6 illustrates how external diffusion reduces the Mach number while increasing the static pressure, making it essential to capture this process accurately. To achieve this, the computational domain must extend sufficiently upstream of the engine. The requirements for domain length and other related parameters are further detailed in Section 3.4.

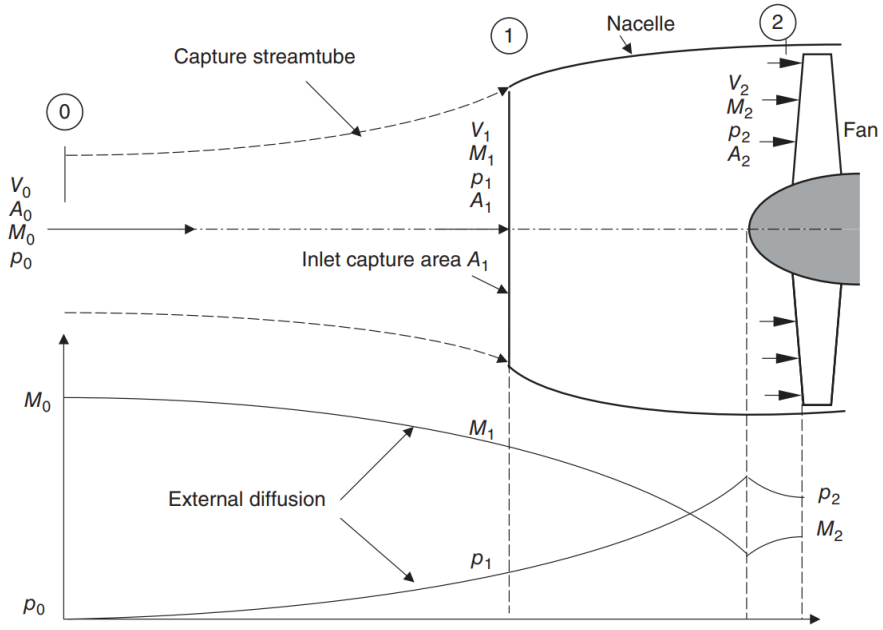

Figure 3.6: Illustration of the stream tube entering the turbofan inlet and the effect on Mach number and static pressure. Adapted from [50].

3.4. Turbofan CFD Domain and Meshing

The computational domain around and upstream of the engine must be large enough to prevent boundary conditions at the domain walls from influencing the flow behaviour within the simulation. Inadequate domain sizing can lead to distorted results and reduced reliability of the thrust results.

Downstream modelling of the exhaust also plays a role in net thrust calculations. Namely, Zimmermann [51] demonstrated that the outlet distribution affects propulsive efficiency due to flow interactions downstream of the nozzle, and that up to 1% improvement in thrust was achieved by carefully tailoring the velocity distribution at the bypass duct outlet. However, the downstream bypass air and core stream exhaust will not be modelled in this study as doing so would require simulating the core flow temperature and pressure distributions, complicating the model and substantially increasing the domain size. Other works, such as Zennaro [52], similarly omit downstream bypass air and core exhaust modelling.

The placement of domain boundaries relative to the turbofan engine is guided by recommendations from various studies. For instance, Baratchi [37] used boundaries extending $5D_n$ upstream, a radial distance of $4D_n$ from the turbine axis, and $10D_n$ downstream, where D_n is the engine nacelle maximum diameter. Kaplan [49] instead used the definition of the engine length L as a reference and modelled a domain spanning $10L$ upstream and $12.5L$ downstream, with a conical far-field boundary tapering from $10L$ upstream to $12.5L$ downstream. Smaller domains are also reported in the literature, such as in Mund [53], which suggests that a domain height of $4D_n$ to $5.5D_n$ is sufficient for cruise conditions.

Turbofan engine simulations employ various meshing techniques to balance accuracy and computational efficiency. The majority of studies, including those performed by Stich et al. [34], Spinner et al. [38], Heidebrecht et al. [54], and Mund and Pilidis [53], utilise a 3D structured quadrilateral grid, with the highest mesh density concentrated near the actuator disk and nozzle outlet. Kwan et al. [8] and Kaplan [49] adopted an unstructured mesh, incorporating triangular or tetrahedral elements in most regions and quadrilateral elements in the boundary layer to improve aerodynamic accuracy.

In optimisation studies, mesh robustness becomes particularly critical. Patrao et al. [10] optimised the duct shape for a turbofan intercooler and recuperator, utilising an unstructured mesh comprising quadrilateral and triangular elements. This approach generates a mesh shown in Figure 3.7 that has sufficient mesh element quality across various duct geometries. The dense mesh near the walls, known as the inflation layer, is still composed of structured quadratic elements. Unstructured grids are especially advantageous in CFD geometry optimisation, as they enhance grid generation robustness and enable the exploration of a broader range of duct shapes while maintaining good element quality. However, this flexibility comes with the trade-off of increased computational time between iterations.

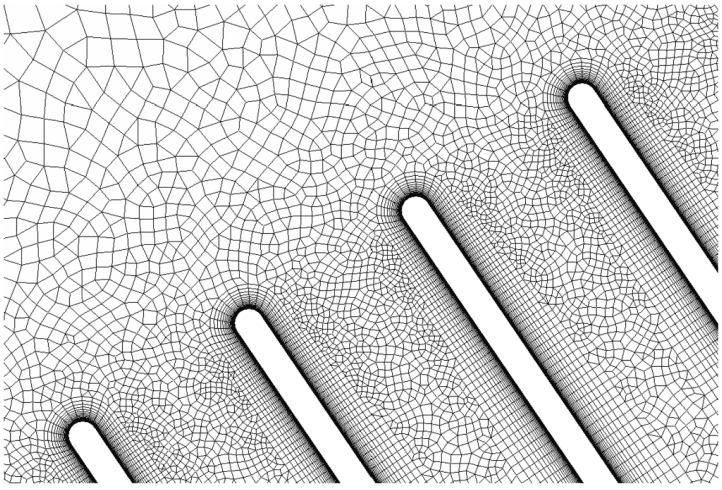

Figure 3.7: The unstructured mesh used by Patrao et al. [10], combining quadrilateral and triangular mesh elements in an unstructured grid while employing a structured quadrilateral grid near the walls.

3.5. Turbulence Model

Reynolds-Averaged Navier-Stokes (RANS) simulations are employed to analyse the thermal performance of heat exchangers. While higher-fidelity turbulence models such as Large Eddy Simulation (LES) or Direct Numerical Simulation (DNS) offer better-defined turbulent flows, they come with significant computational demands for an optimisation process. RANS, on the other hand, balances accuracy and computational efficiency, making it the preferred approach for this analysis.

With Reynolds averaging, the variables in the momentum and continuity equations are divided into a mean component and a fluctuating component. For the velocity components, this is expressed as

$$v_i = \bar{v}_i + v_i' . \tag{3.4}$$

For a 2D cartesian coordinate reference, the momentum equation tensor form can be written out as [17]

$$\frac{\partial}{\partial t}\left(\rho v_i\right) + \frac{\partial}{\partial x_j}\left(\rho v_i v_j\right) = -\frac{\partial p}{\partial x_i} + \frac{\partial}{\partial x_j}\left[\mu\left(\frac{\partial v_i}{\partial x_j} + \frac{\partial v_j}{\partial x_i} - \frac{2}{3}\delta_{ij}\frac{\partial v_l}{\partial v_l}\right)\right] + \frac{\partial}{\partial x_j}\left(-\rho\overline{v_i' v_j'}\right) \tag{3.5}$$

where $-\rho\overline{u_i' u_j'}$ represents the apparent stress due to a fluctuating velocity field, also designated as τ_{ij}. This is known as the Reynolds stress term and must be modelled in order to solve the momentum equation. The Boussinesq hypothesis can be used to formulate the stress term in terms of the mean velocity gradients [17], formulated as

$$-\rho\overline{v_i' v_j'} = \tau_{ij} = \mu_t\left(\frac{\partial v_i}{\partial x_j} + \frac{\partial v_j}{\partial x_i}\right) - \frac{2}{3}\left(\rho k + \mu_t\frac{\partial v_k}{\partial x_k}\right)\delta_{ij} \tag{3.6}$$

where μ_t is the turbulent viscosity, k is the turbulent kinetic energy, and the subscript k refers to the spatial direction in tensor notation. The Boussinesq hypothesis allows for a computationally inexpensive way to calculate μ_t as it only requires one or two more transport equations, depending on which turbulence model is used. Three options employ this hypothesis: the Spalart-Allmaras (S-A), k-ε and k-ω models. These are the three most utilised turbulence models in the literature relating to CFD simulations of turbofans and porous zones, and Table 3.3 provides a summary of the turbulence model employed in the most relevant works.

Authors	**Turbofan Analysis**	**Porous Media Model**	**k-ε**	**k-ω SST**	**S-A**
Heidebrecht et al.	X			X	
Hooman & Gurgenci		X	X		
Kwan et al.	X	X	X		
Missirlis et al.	X	X		X	
Musto et al.		X		X	
Patrao et al.	X			X	
Spinner et al.	X				X
Stich et al.	X				X
Zhu et al.		X		X	

Table 3.3: Summary of turbulence models used in various literature sources

The table shows that the k-ω Shear-Stress Transport (SST) model is a popular model for both turbofan and porous zone modelling. First proposed by Menter [55], it utilises the k-ω method near the walls of the model and blends into the k-ε method in the freestream of the flow, combining the strengths of both and making it a suitable model for many CFD applications. It requires two additional transport equations; the first is to solve for the turbulence kinetic energy k

$$\frac{\partial \rho k}{\partial t} + \frac{\partial \rho v_j k}{\partial x_j} = \tau_{ij}\frac{\partial v_i}{\partial x_j} - \beta^*\rho\omega k + \frac{\partial}{\partial x_j}\left[\left(\mu + \sigma_k\mu_t\right)\frac{\partial k}{\partial x_j}\right] \tag{3.7}$$

where σ_k is the turbulent Prandtl number for k, μ_t is the turbulent eddy viscosity, μ is the dynamic viscosity, and β^* is a constant. The second additional equation solves for the specific dissipation rate ω, making use of the empirical constants γ and β as well as the turbulent Prandtl numbers σ_ω and $\sigma_{\omega 2}$ and expressed as

$$\frac{\partial \rho\omega}{\partial t} + \frac{\partial \rho v_j \omega}{\partial x_j} = \frac{\gamma}{\nu_t}\tau_{ij}\frac{\partial v_i}{\partial x_j} - \beta\rho\omega^2 + \frac{\partial}{\partial x_j}\left[\left(\mu + \sigma_\omega \mu_t\right)\frac{\partial \omega}{\partial x_j}\right] + 2\left(1 - F_1\right)\rho\frac{\sigma_{\omega_2}}{\omega}\frac{\partial k}{\partial x_j}\frac{\partial \omega}{\partial x_j}. \tag{3.8}$$

Equations 3.7 and 3.8 present the unsteady and convection terms on the LHS of the equation and the production, dissipation and diffusion terms on the RHS of the equation, respectively. However, a noteworthy addition to Equation 3.8 is the final term, representing the cross-diffusion term. This term is the same one present in the k-ε transport equations, except it includes the blending function F_1 to enable a smooth transition from the k-ω to the k-ε models. By using the cross-diffusion term, the accuracy of turbulence modelling in the freestream is maintained from a k-ε model and the prediction of separation in adverse pressure gradients is leveraged from a k-ω model [56]. The term F_1 is a hyperbolic tangent function, dependent on the distance to the closest wall d and formulated as

$$F_1 = \tanh\left(\arg_1^4\right) \tag{3.9}$$

$$\arg_1 = \min\left[\max\left(\frac{\sqrt{k}}{\beta^*\omega d}, \frac{500\nu}{d^2\omega}\right), \frac{4\rho\sigma_{\omega 2}k}{CD_{k\omega}d^2}\right]. \tag{3.10}$$

The cross-diffusion correction $CD_{k\omega}$ accounts for any interaction between k and ω gradients in the airflow, and is maintained above 10^{-20} for numerical stability. It is defined as

$$CD_{k\omega} = \max\left(2\rho\sigma_{\omega 2}\frac{1}{\omega}\frac{\partial k}{\partial x_j}\frac{\partial \omega}{\partial x_j}, 10^{-20}\right). \tag{3.11}$$

Next to its implementation in the transport equation, the term F_1 also blends the constants of the k-ω and k-ε models. A constant ϕ can be blended according to

$$\phi = F_1\phi_1 + \left(1 - F_1\right)\phi_2. \tag{3.12}$$

Even with these equations implemented, Menter noticed that the separation behaviour was still not predicted accurately, and to solve this, the turbulent eddy viscosity μ_t is limited according to the function

$$\mu_t = \frac{\rho a_1 k}{\max\left(a_1\omega, \Omega F_2\right)} \tag{3.13}$$

where Ω is the vorticity magnitude while a_1 is an empirical constant. Once again, a blending function F_2 is used, this time defined according to a different hyperbolic tangent argument, which restricts the application of the k-ω model near the wall and can be formulated as

$$F_2 = \tanh\left(\arg_2^2\right) \tag{3.14}$$

$$\arg_2 = \max\left(2\frac{\sqrt{k}}{\beta^*\omega d}, \frac{500\nu}{d^2\omega}\right). \tag{3.15}$$

Overall, these equations are implemented by the ANSYS Fluent software to simulate realistic flow behaviour both near the wall and in the freestream, with only the empirical constants as inputs. These fixed values have been determined in the research by Menter [55].

When considering which turbulence model to implement, it is important to remember the simplifications of using an actuator disk to simulate the fan and OGVs, and the porous zone to model the heat exchanger. While these simplifications can capture the general trends of flow behaviour, including pressure, temperature and flow velocity, accurately modelling the turbulent intensity is challenging. Ahlinder [57] used a porous media model to simulate the intercooler and recuperator in a gas turbine engine. The HEX cores are of the tube bundle types. The research states that the turbulence viscosity is over-estimated inside the porous zone compared to simulations modelling the heat exchanger geometry,

as mentioned in Subsection 2.2.3. This overestimation is especially the case for flows with a high Reynolds number, and consequently, it limits the overall accuracy of turbulence modelling within the porous zone. The drag coefficient of the porous zone, however, is not significantly affected by the turbulence intensity [57].

Similarly, the actuator disk model relies on data of the total pressure increase, flow rate, velocity profiles and efficiency data, but detailed data on turbulence behind the fan and OGVs is often unavailable. The research of Grace et al. [58] compared turbulence intensity, length scale and dissipation rate of a Lattice-Boltzmann-based software with experimental data to produce plots of the turbulence values at different turbofan stations. However, the turbulence length scale results deviated from experimental results and showed a slight under-prediction of the turbulent dissipation rate. In addition, this would add significant complexity to the simulations and increase the computational time per iteration, while the effects on the optimisation process may not be evident.

The Spalart–Allmaras (S-A) turbulence model is considered as an alternative option and has been successfully applied in turbofan bypass duct CFD simulations, including studies by Spinner et al. [38] and Stich et al. [34]. The S-A model is a one-equation model, saving computational time, and it requires a less refined CFD mesh near the walls of the turbofan model. Although the S–A model is commonly used in turbofan flow simulations, Ahlinder [57] recommends a two-equation turbulence model for simulations involving porous media models to strike a balance between flow resolution inside the porous zone and in the rest of the CFD domain. Therefore, the k-ω SST model is preferred for this research.

3.6. Verification and Validation

Verification and validation studies are performed to assess the reliability and accuracy of the CFD results. Verification focuses on whether the numerical model correctly solves the governing equations, free from any errors introduced by discretisation, grid resolution, or algorithmic implementation, while validation is done to see if the model accurately represents the real-world flow behaviour by comparing the simulation results to experimental and/or analytical data. Several literature sources are available to perform the verification and validation, which are discussed in this section.

The validation of HeXaCode, the program used to determine the heat transfer of the condenser, has been performed independently by Beltrame et al. [59] through comparison with the program EchTherm. Additionally, using energy source terms in a porous zone CFD based on these HeXaCode calculations has been implemented previously to verify a quasi-1D model of a ram air duct [21]. Therefore, the validation efforts in this research will focus on correctly implementing the actuator disk model for the fan and OGVs.

3.6.1. Verification of the CFD Model

Focusing first on verification, the quality of the generated mesh can be determined partially through a mesh sensitivity study. When analysing the porous media model of a CC-TF condenser, van Dongen [6] observes the effect of grid refinement on the total pressure change, the total temperature change and the effective area fraction of the diffuser outlet. For the analysis performed in this research, the effect of the grid resolution on net thrust is also an important factor that should be included. Celik et al. [60] indicate that a refinement ratio of 1.3 between different mesh resolutions is sufficient to determine the effect on the CFD results properly. Through this process, a suitable compromise can be found between accuracy in results and reduction in the time needed for the optimisation.

Verification can also incorporate wall treatment analysis by comparing y^+ and u^+ values. The parameter y^+ is a non-dimensional way of measuring how close the first computational grid point is to the wall in relation to the viscous sublayer, while u^+ is a dimensionless velocity using the wall shear velocity u_τ as a scaling factor. These parameters are defined as

$$y^+ = \frac{\rho u_\tau y}{\mu} \tag{3.16}$$

$$u^+ = \frac{u}{u_\tau} \tag{3.17}$$

while u_τ is defined according to the wall shear stress as.

$$u_\tau = \sqrt{\frac{\tau_w}{\rho}}. \tag{3.18}$$

For a CFD simulation employing a k-ω SST model, the plot comparing y^+ and $u+$ at the walls should follow the trend in Figure 3.8. When $y^+ < 5$, the flow is treated as being in the viscous sublayer, which is dominated by viscous forces and has a linear velocity profile, $u^+ = y^+$. In a wall-resolving turbulence model, like k-ω SST, this region must be resolved, and therefore, the value of y^+ should always be smaller than 1 at the walls. In the buffer layer, $5 < y^+ < 30$, both viscous and turbulent forces affect the flow behaviour, and as such the velocity profile begins to deviate from its linear behaviour. Above $y^+ = 30$, the flow is dominated by turbulent behaviour, and the non-dimensional flow velocity follows the logarithmic equation in Figure 3.8. The coefficients are empirically found to be $k = 0.4187$ and $B \approx 5.2$ in most cases.

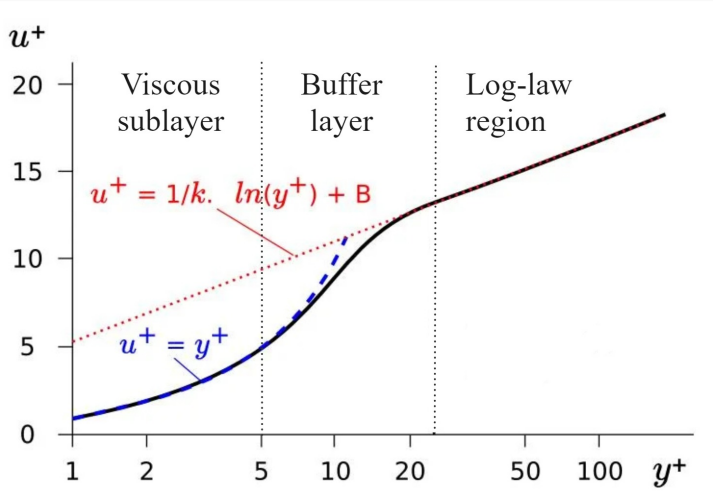

Figure 3.8: The turbulent boundary layer (TBL) plot comparing y^+ and u^+ values. Adapted from [61].

The numerical schemes employed in the simulations must also be verified to ensure accuracy. If a first-order accurate scheme is used for the convection and diffusion terms, it results in increased numerical diffusion and dissipation, which is not representative of the real-life flow behaviour. Therefore, second-order schemes should be used for these terms.

Furthermore, a test case involving a straight duct section can verify correct implementation of the porous zone. Pressure losses, flow redistribution, and heat transfer predicted by the porous media model should align with theoretical expectations and empirical data. A simple test to ensure correct porosity implementation is to activate only the porosity, neglect the momentum and energy source terms, and check that the velocity increase matches expectations. As previously mentioned in Equation 2.3, the physical velocity occurring in the porous zone is related to the superficial velocity by the porosity ε, so proper implementation can be checked by observing if the velocity increases by $1/\varepsilon$ throughout the entire porous zone. By verifying the porous media implementation in a simplified geometry, the results can be analysed more easily than a porous media model in a bypass duct, where the duct geometry introduces more flow complexity.

To verify the implementation of the actuator disk model, the total pressure distribution immediately downstream of the fan can be compared to results from Spinner et al. [38] and Mund and Pilidis [47], while axial, radial, and tangential velocity profiles can be evaluated against the research of Stich et al. [34]. These comparisons ensure that the actuator disk accurately replicates the aerodynamic impact of the fan. External aerodynamics, particularly around the nacelle and inlet, can be verified against contour data from Savelyev et al. [46]. The inlet flow behaviour is crucial to determine accurate mass flow and flow conditioning into the fan and bypass duct. Additionally, net thrust calculated in the

simulation is compared to expected thrust values of the LEAP-1A during cruise to ensure that the propulsive performance aligns with realistic scenarios.

An additional layer of verification is achieved through a sensitivity analysis, which evaluates the behaviour of the model with variations in input parameters. These include changes in the thrust distribution across the bypass duct and fan, adjustments to boundary conditions, modifications of the porous media properties such as porosity, and variations in pressure loss coefficients. Assessing how sensitive the model is to these inputs gives an indication of the robustness of the CFD setup. Finally, the behaviour of the CFD model is verified through visualisation techniques; streamlines are used to examine flow patterns to spot any separation, recirculation, and flow acceleration within the bypass duct. Contour plots of temperature and pressure provide insight into the thermal and aerodynamic behaviour of the porous media model and the bypass duct nozzle and can help to visually identify any gross anomalies.

3.6.2. Validation of the Fan Actuator Disk Model

Figure 3.9 plots the experimental results from the NASA UHB Drive Rig [40] for a high bypass turbofan engine. This dataset includes key performance metrics, such as the relationship between the fan speed as a percentage of maximum rpm and the corrected mass flow rate, which can then, in turn, be used to derive the fan total pressure ratio. The fan model accuracy can be evaluated by comparing the fan pressure ratios and air mass flow rates obtained in CFD to this plot.

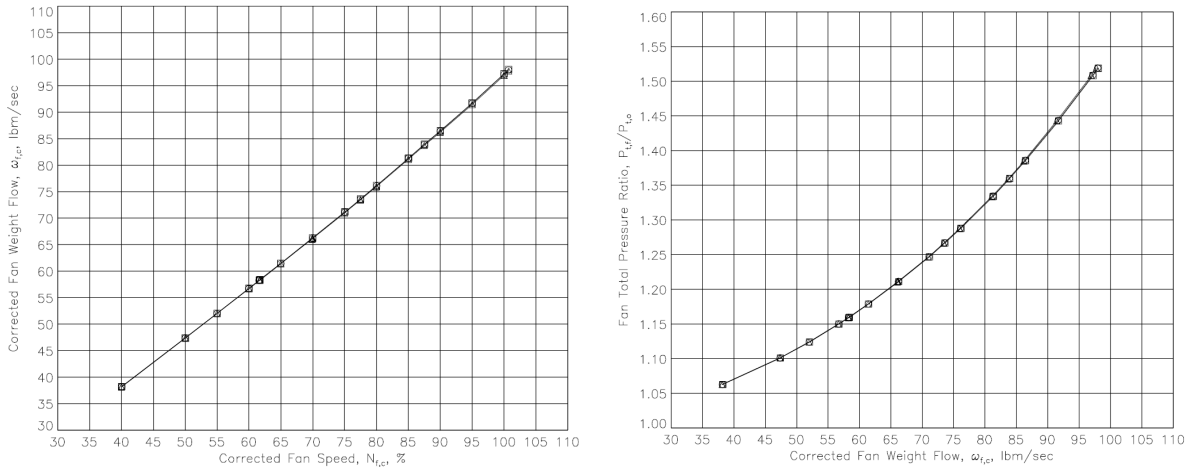

(a) Corrected mass flow rate (fan weight flow) versus fan speed.

(b) Fan total pressure ratio vs. corrected mass flow rate.

Figure 3.9: Experimental data from a high bypass turbofan, from Hughes [40].

The performance of a compressor can be visualised with a compressor map, an example of which is shown in Figure 3.10. For every rpm setting of the fan, an optimal mass flow rate and total pressure ratio exist to achieve maximum fan efficiency, and the contours in Figure 3.10 illustrate that maximum efficiency often occurs near the middle of the map. If the mass flow rate is too low and passes the stall line, the angle of attack of the airflow on the blades exceeds the stall angle of attack, causing separation and disrupting the compression process. In extreme cases, it can lead to a surge where the flow direction reverses and generates significant oscillations in the compressor. On the other hand, mass flow rates that are too high will cause the compressor to choke, so any additional airflow will not result in a higher total pressure ratio. Therefore, in order to maintain a realistic flow scenario, it is important that the fan pressure ratio observed in CFD does not vary much with respect to the curve in Figure 3.9b.

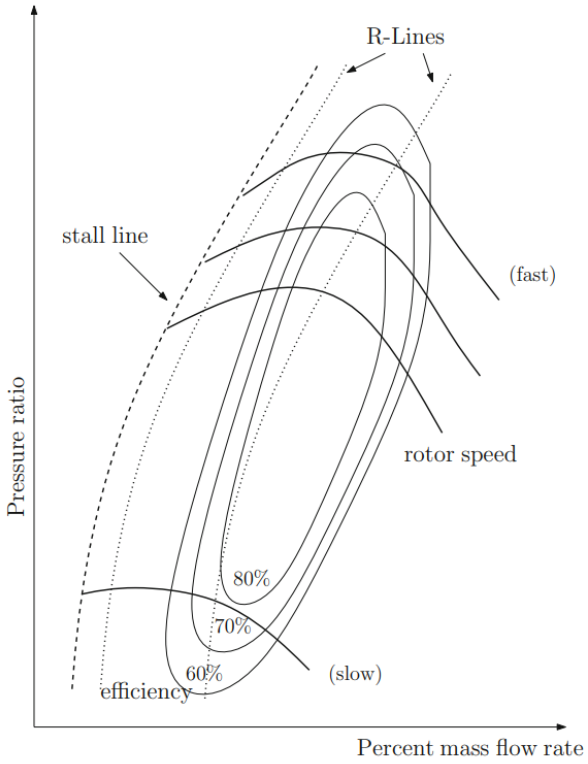

Figure 3.10: Compressor map, with lines of constant efficiency and constant rotor speed. Adapted from [30]

.

4

Optimisation of the Bypass Duct Geometry

Adding a condenser in the bypass duct adds complexity to the resulting airflow behaviour thus affecting the overall engine performance, especially the net thrust. Optimisation of bypass duct can reduce the drag penalty introduced by the condenser and maximise net thrust. This chapter focuses on different optimisation methods for achieving the best duct shapes, particularly in the areas immediately upstream and downstream of the condenser, to decrease drag and ensure effective flow management. The optimisation process is conducted entirely within the ANSYS Workbench environment, requiring a precise and robust parametrisation of the duct geometry.

4.1. Summary of different optimisation methods

Several optimisation techniques are available for adjusting geometries in ANSYS Workbench, broadly categorised into gradient-based methods and derivative-free methods. Both approaches can be considered depending on the complexity of the problem and the nature of the design space.

4.1.1. Derivative-free Methods

Derivative-free methods, which do not depend on gradient information, are used in objective functions that are noisy or highly non-linear. Among these methods, genetic algorithms (GAs) are a popular choice and are based on the principles of natural selection and evolution. These algorithms evaluate a population of potential solutions and employ processes like mutation, crossover, and selection to evolve towards an optimal design. Genetic algorithms are effective at exploring complex, non-convex design spaces and are good at avoiding local optima. However, a significant drawback is their high computational cost, which arises from the need to evaluate numerous candidate solutions. In the context of turbofan duct shaping, Patrao et al. [10] and Clemen et al. [62] both chose to employ the Natural Search Genetic Algorithm NSGA-II to optimise turbofan duct and OGV geometries, with the former using a population size of 100 individuals over 100 different generations and the latter using 80 individuals over 60 generations to optimise the OGV shape.

Another approach to derivative-free optimisation is the Design of Experiments (DoE) method, which systematically samples the design space to explore relationships between design variables and performance metrics. Bajimaya et al. [63] employed a full factorial DoE approach to study the integration of a ducted HEX within the bypass duct while varying both the length and height of the HEX. A DoE is particularly well-suited for initial design exploration and allows the researchers to create plots of the design space like that shown in Figure 4.1. A downside is that this can also become computationally expensive when applied to high-dimensional problems due to the large number of simulations required. This approach is therefore not as well suited for complex variations in duct geometries.

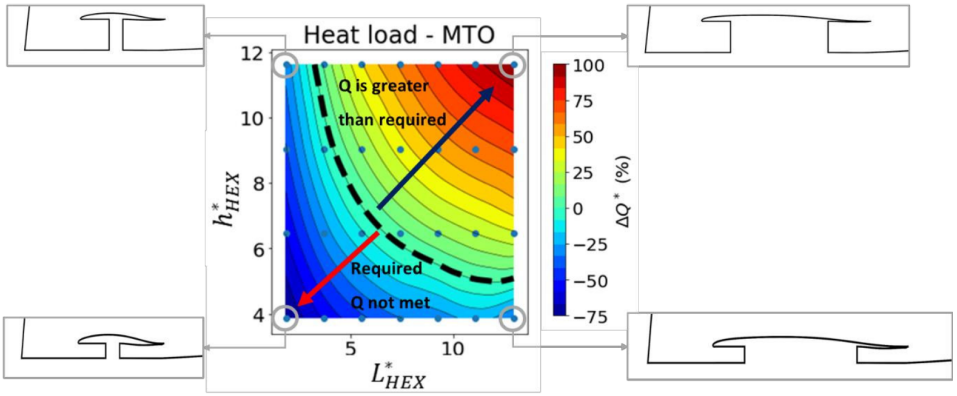

Figure 4.1: Results of a DoE methodology to explore possible duct geometries, showing the heat load for different ducted HEX designs. From [63].

4.1.2. Gradient-based Methods

Gradient-based methods utilise derivative information to locate the optimal solutions, making them particularly well-suited for problems with smooth and differentiable objective functions. These methods generally converge faster than derivative-free approaches and are widely used for aerodynamic and thermal optimisation [64].

Witte and Bode [65] use a gradient-based method to optimise a simplified bypass duct geometry to integrate heat transfer structures that contribute to aerodynamic efficiency. The cost functions of the optimisation methodology were the pressure drop and heat transfer, allowing for the creation of a Pareto front in the 2D space of these parameters. With this Pareto front, a trade-off analysis is possible in which multiple design solutions can be considered, some with greater emphasis on aerodynamic efficiency and others emphasising improved heat transfer. The results demonstrated how gradient-based methods can effectively balance competing objectives.

Although gradient-based optimisation methods are computationally efficient for problems with a large number of design variables, they are susceptible to convergence issues. Namely, they may converge to local minima and require accurate gradient estimations which may be challenging for highly non-linear or noisy problems. Within ANSYS Workbench, two gradient-based methods are particularly suitable for duct optimisation:

Nonlinear Programming by Quadratic Lagrangian (NLPQL): NLPQL is a sequential quadratic programming (SQP) algorithm designed for continuous-variable optimisation problems [66]. The NLPQL routine works by iteratively solving a quadratic approximation of the Lagrangian function to update the design variables. This method works effectively for single-objective problems with smooth constraints and objectives, accepting equality, inequality and bound constraints. However, the NLPQL routine struggles with noisy functions and is unsuitable for discrete design variables.

Adaptive Single-Objective (ASO) Method: This method combines aspects from a DoE method with the gradient-based Mixed-Integer Sequential Quadratic Programming (MISQP) optimisation algorithm. The algorithm employs a response surface combining advantages of both derivative-free and gradient-based methods [67]. The ASO method is efficient for single-objective problems and straightforward to implement within the ANSYS framework while also avoiding local minima more than other gradient-based methods. The optimisation inputs are the number of initial samples to create a response surface, the maximum number of total iterations and the convergence tolerance.

This method is particularly suitable for a duct optimisation problem where the primary focus lies on the aerodynamic optimisation of the bypass duct and maximisation of net thrust. The ASO routine allows for automatic adjustment of the step size for a more strategic search strategy and can be performed within acceptable time frames. However, the ASO routine does not allow for a trade-off comparison between heat transfer and aerodynamic efficiency through a Pareto front due to its single-objective nature. Nevertheless, this method is chosen as the preferred optimisation routine for this research.

4.2. Parametrisation of the ducts

The parametrisation method chosen to vary the bypass duct geometry can affect the chosen optimisation routine, the computational time, and the flexibility of adjusting the geometry. One approach of geometric parameterisation involved using control points to guide smooth Bezier curves, cubic splines or B-splines, and by adjusting the coordinates of the control points, the geometry of the duct is automatically updated. Patrao et al. [10] use Bezier curves and control points to parametrise a HEX and duct geometry. Cartesian coordinates define control points of the ducts and variables to define the HEX inclination and centroid location. Clemen et al. [62] also use control points to define the bypass duct walls. However, these 5 points are axially fixed and allowed to vary only in the radial direction. The advantage of this method is that it reduces the number of variables needed by half, making it a simple yet effective method of defining geometry. The bypass duct inlet and exit axial positions are kept constant; in this way, the overall turbofan length is not affected, which would require extensive redesign of the entire engine. Using cubic splines instead of B-splines of Bezier curves ensures the curves pass through the control points, making it simpler to set the constraints for the control points.

An alternative parametrisation method employs Class Shape Transformation (CST) functions. This method is commonly used in aerospace engineering to define airfoils or other aerodynamic surfaces with great flexibility. The CST method combines a class function $C(x)$ and a shape function $S(x)$ to generate smooth geometries, with the class function defining the general geometric features and the shape function capturing finer geometric details. The CST functions can be expressed through Cartesian coordinates as

$$y(x) = C(x)\,S(x) + x\,\Delta y\,. \tag{4.1}$$

The last term is optional, and it allows for offset adjustments to the geometry. Generally, the class function is defined using two exponents, N and M, as

$$C(x) = x^N(1-x)^M \tag{4.2}$$

while the shape function $S(x)$ expresses surface details using a combination of shape coefficients a_i and Bernstein polynomials $B(x)$ to make the curves transition smoothly. This is expressed as

$$S(x) = \sum_{i=0}^{n} a_i B_i(x) \tag{4.3}$$

$$B_i(x) = \binom{n}{i} x^i (1-x)^{n-i}\,. \tag{4.4}$$

The y-coordinate can therefore be expressed through the x-coordinate as

$$y(x) = \left[x^N(1-x)^M\right] \cdot \left[\sum_{i=0}^{n} a_i \binom{n}{i} x^i (1-x)^{n-i}\right] \tag{4.5}$$

The CST method has previously been implemented successfully for bypass duct nozzle design [43] and optimisation. The CST method can also be combined with other methods to provide even greater control over aerodynamic design. Namely, Christie et al. [68] use a combination of the CST method and PARSEC method, developed by Sobieczky [69], to give even more control over aerodynamic design, called the iCST method. This method is also suitable for turbofan bypass duct design, as shown by Bajimaya et al. [63].

While CST methods provide more refined geometrical control, they do not necessarily reduce the number of variables compared to a method employing axially fixed control points. Given the simplicity of implementing a control point method into ANSYS Fluent, it is preferred for initial optimisation studies.

5

Conclusion and Research Question

The information presented in this study builds upon relevant literature to establish a comprehensive framework for analysing and optimising the bypass duct geometry of a Combined-Cycle Turbofan (CC-TF) engine with an integrated heat exchanger (HEX) using CFD. The research encompasses several key topics necessary for developing the CFD model.

Chapter 2 discussed the type, design and integration of HEX in the bypass duct using CFD. By using HEX classification categories from literature [11], the design of the condenser was narrowed down to a flat-tube microchannel heat exchanger employing louvred fins, resulting in a high HEX compactness β and heat transfer coefficient. Previous research showed that a porous media model can be used to successfully approximate the presence of a HEX in an aerospace application [8, 9, 14], using momentum source terms to approximate the air-side pressure drop and energy source terms to approximate the heat transfer to the airflow. The factors affecting the successful integration of the HEX were discussed, primarily to identify the optimal HEX inclination and the use of the Meredith effect to minimise the drag.

Chapter 3 introduced the trends in turbofan bypass ratios in order to select the LEAP-1A engine as a baseline model for the CFD analysis. Next, the actuator disk model was presented as a method used in literature to simulate the aerodynamic effect of the fan and outlet guide vanes (OGVs) using a custom thrust loading profile [34, 38, 47]. Relevant phenomena of external aerodynamics are covered, followed by the modelling and meshing of the CFD domain in the relevant literature. The k-ω SST model was chosen as the turbulence model for the analysis, owing to its realistic flow modelling both in the freestream and near the turbofan walls. The chapter also presented various methods that can be employed to verify and validate the CFD simulations.

Finally, Chapter 4 provided an overview of the available optimisation methods, deducing that the Adaptive Single-Objective algorithm is a suitable gradient-based scheme for optimisation. Parametrisation through control points and cubic splines was preferred over the Class Shape Transformation (CST) approach.

A key knowledge gap identified in current research is the lack of effective combinations of simplified CFD models to represent a turbofan engine with an integrated condenser while staying computationally efficient. Specifically, the combination of a porous media model for the heat exchanger and an actuator disk model for the fan and outlet guide vanes has not been explored in the context of optimising the bypass duct aerodynamics. Therefore, this research aims to address this knowledge gap.

Consequently, the central research question guiding this study is formulated as:

"How can integrating a condenser within the bypass duct of a turbofan engine be optimised to maximise the net thrust using a computationally efficient CFD optimisation framework?"

The scope of the research can be defined as:

"**Assessing the suitability of a gradient-based CFD optimisation framework to determine the optimal bypass duct geometry of a Combined-Cycle turbofan**
by
employing a porous zone to simulate the heat exchanger and an actuator disk to model the fan and outlet guide vanes to significantly reduce the computational cost of the problem."

Addressing this research question, the study aims to assess the practicality of using simplified CFD methods to model heat exchangers in a bypass duct and offer valuable insights that could benefit the wider fields of combined-cycle propulsion and aerodynamic optimisation.

References

[1] D. McConnachie, C. Wollersheim, and R. J. Hansman. "The Impact of Fuel Price on Airline Fuel Efficiency and Operations". In: *2018 Aviation Technology, Integration, and Operations Conference* (Aug. 2013). DOI: 10.2514/6.2013-4291. URL: https://doi.org/10.2514/6.2013-4291.

[2] B. Owen, D. S. Lee, and L. Lim. "Flying into the Future: Aviation Emissions Scenarios to 2050". In: *Environmental Science & Technology* 44.7 (Mar. 2010), pp. 2255–2260. DOI: 10.1021/es902530z. URL: https://doi.org/10.1021/es902530z.

[3] S. Mithal and D. Rutherford. "ICAO's 2050 net-zero CO". In: *POLICY* (Jan. 2023).

[4] C. M. De Servi et al. "Exploratory assessment of a combined-cycle engine concept for aircraft propulsion". In: *Proceedings of the 1st Global Power and Propulsion Forum, Zurich, Switzerland*. 2017, pp. 16–18.

[5] C. A. Perullo, D. N. Mavris, and E. Fonseca. "An Integrated Assessment of an Organic Rankine Cycle Concept for Use in Onboard Aircraft Power Generation". In: *Proceedings of ASME Turbo Expo 2013*. The American Society of Mechanical Engineers, June 2013. DOI: 10.1115/gt2013-95734. URL: https://doi.org/10.1115/gt2013-95734.

[6] J. van Dongen. "Modelling and Guidelines for Ram Air Ducts Using the Meredith Effect Applied to an Organic Rankine Cycle Waste Heat Recovery System". MA thesis. TU Delft, 2024.

[7] S. Kaiser et al. "The Water-Enhanced Turbofan as Enabler for Climate-Neutral Aviation". In: *Applied Sciences* 12.23 (Dec. 2022), p. 12431. DOI: 10.3390/app122312431. URL: https://doi.org/10.3390/app122312431.

[8] P. Kwan et al. "Minimising Loss in a Heat Exchanger Installation for an Intercooled Turbofan Engine". In: *Proceedings of ASME Turbo Expo 2011*. the American Society of Mechanical Engineers (ASME), Jan. 2011, pp. 189–200. DOI: 10.1115/gt2011-45814. URL: https://doi.org/10.1115/gt2011-45814.

[9] D. Missirlis et al. "Optimization of Heat Exchangers for Intercooled Recuperated Aero Engines". In: *Aerospace* 4.1 (Mar. 2017), p. 14. DOI: 10.3390/aerospace4010014. URL: https://doi.org/10.3390/aerospace4010014.

[10] A. Patrao et al. "Compact heat exchangers for hydrogen-fueled aero engine intercooling and recuperation". In: *Applied Thermal Engineering* 243 (Jan. 2024), p. 122538. DOI: 10.1016/j.applthermaleng.2024.122538. URL: https://doi.org/10.1016/j.applthermaleng.2024.122538.

[11] R. K. Shah and D. P. Sekulić. *Fundamentals of Heat Exchanger Design*. John Wiley & Sons, Ltd, July 2003. DOI: 10.1002/9780470172605. URL: https://doi.org/10.1002/9780470172605.

[12] I.V. Tishchenkoet al. "Mathematical modeling of plate-fin heat exchanger in aircraft environmental control system". In: *AIP conference proceedings* (Jan. 2019). DOI: 10.1063/1.5140174. URL: https://doi.org/10.1063/1.5140174.

[13] Z. Liu et al. "Performance of parallel plate-fin heat exchanger for piston aero-engines with front-placed guide plate at high altitude". In: *Applied Thermal Engineering* 214 (June 2022), p. 118829. DOI: 10.1016/j.applthermaleng.2022.118829. URL: https://doi.org/10.1016/j.applthermaleng.2022.118829.

[14] M. Musto. "A simplified methodology to simulate a heat exchanger in an aircraft's oil cooler by means of a Porous Media model". In: *Applied Thermal Engineering* 94 (2015), pp. 836–845.

[15] J. Yang et al. "A comparison of four numerical modeling approaches for enhanced shell-and-tube heat exchangers with experimental validation". In: *Applied Thermal Engineering* 65.1-2 (Jan. 2014), pp. 369–383. DOI: 10.1016/j.applthermaleng.2014.01.035. URL: https://doi.org/10.1016/j.applthermaleng.2014.01.035.

[16] S. S. Bhosale and A. R. Acharya. "Review On Applications of Micro Channel Heat Exchanger". In: *International Research Journal of Engineering and Technology (IRJET)* 07.03 (Mar. 2020). DOI: 10.13140/RG.2.2.31044.65922. URL: https://doi.org/10.13140/RG.2.2.31044.65922.

[17] ANSYS Inc. *Ansys Fluent Theory Guide*. ANSYS Inc. Press, 2023.

[18] H. Darcy. *Les fontaines publiques de la ville de Dijon: exposition et application des principes à suivre et des formules à employer dans les questions de distribution d'eau*. Vol. 1. Victor dalmont, 1856.

[19] M. Quintard. "Introduction to Heat and Mass Transport in Porous Media". In: *NATO, S&T Organization public release* (2016).

[20] D. Krempus et al. "Organic Rankine Cycle Waste Heat Recovery Systems for Aircraft Engines". PhD thesis. Delft University of Technology, 2025. DOI: 10.4233/uuid:5e565f99-a9f4-4208-95e9-2c542fd720f8. URL: https://doi.org/10.4233/uuid:5e565f99-a9f4-4208-95e9-2c542fd720f8.

[21] F. Beltrame et al. "Optimal Design of a Ram Air Cooling Duct housing the Condenser of an Airborne ORC WHR Unit". In: *Global Power & Propulsion Society* GPPS-TC-2024-0107 (2024).

[22] E. N. Sieder and G. E. Tate. "Heat Transfer and Pressure Drop of Liquids in Tubes". In: *Industrial Engineering Chemistry* 28.12 (Dec. 1936), pp. 1429–1435. DOI: 10.1021/ie50324a027. URL: https://doi.org/10.1021/ie50324a027.

[23] K. Hooman and H. Gurgenci. "Porous Medium Modeling of Air-Cooled Condensers". In: *Transport in Porous Media* 84.2 (Nov. 2009), pp. 257–273. DOI: 10.1007/s11242-009-9497-8. URL: https://doi.org/10.1007/s11242-009-9497-8.

[24] O. Halim et al. "A comparative analysis of detailed and reduced CFD approaches to model wire-wrapped fuel bundles for LMFBRs applications". In: *Annals of Nuclear Energy* 211 (Oct. 2024), p. 110937. DOI: 10.1016/j.anucene.2024.110937. URL: https://doi.org/10.1016/j.anucene.2024.110937.

[25] M. Drela. "Aerodynamics of heat exchangers for high-altitude aircraft". In: *Journal of Aircraft 33* 176 (1996).

[26] F. W. Meredith. *Cooling of aircraft engines with special reference to ethylene glycol radiators enclosed in ducts*. Tech. rep. No 1683. Aeronautical Research Committee Reports and Memoranda, Aug. 1935. URL: https://naca.central.cranfield.ac.uk/handle/1826.2/1425?show=full.

[27] M. R. Nichols. "Investigation of Flow through an Intercooler Set at Various Angles to the Supply Duct". In: *NACA Wartime Report* (Apr. 1942). URL: https://digital.library.unt.edu/ark:/67531/metadc62653/m2/1/high_res_d/19930093676.pdf.

[28] C. Graff. *P-51 Mustang: Seventy-Five Years of America's Most Famous Warbird*. Zenith Press, 2015.

[29] A. Marcellan, M. Henke, and S. Schuldt. "A numerical investigation of the Water-Enhanced Turbofan laboratory-scale ground demonstrator". In: *AIAA SCITECH 2022 Forum* (Jan. 2022). DOI: 10.2514/6.2022-0062. URL: https://doi.org/10.2514/6.2022-0062.

[30] H. Richter. *Advanced Control of Turbofan Engines*. Springer New York, Oct. 2011. DOI: 10.1007/978-1-4614-1171-0. URL: https://doi.org/10.1007/978-1-4614-1171-0.

[31] P. Alves, M. Silvestre, and P. Gamboa. "Aircraft Propellers—Is There a Future?" In: *Energies* 13.16 (Aug. 2020), p. 4157. DOI: 10.3390/en13164157. URL: https://doi.org/10.3390/en13164157.

[32] G. C. Oates. *Aerothermodynamics of Gas Turbine and Rocket Propulsion*. American Institute of Aeronautics and Astronautics, Inc., Jan. 1997. DOI: 10.2514/4.861345. URL: https://doi.org/10.2514/4.861345.

[33] O. Sjögren et al. "Estimation of Design Parameters and Performance for a State-of-the-Art Turbofan". In: *ASME Turbo Expo*. June 2021. DOI: 10.1115/gt2021-59489. URL: https://doi.org/10.1115/gt2021-59489.

[34] G. Stich et al. "Validation of Actuator Disk, Actuator Line and Sliding Mesh Methods within the LAVA Solver". In: *The 11th International Conference on Computational Fluid Dynamics*. ICCFD11-2022-0903. 2022.

[35] W. Froude. *On the elementary relation between pitch, slip, and propulsive efficiency*. Tech. rep. National Advisory Committee for Aeronautics, 1920.

[36] R. G. Rajagopalan and J. B. Fanucci. "Finite difference model for vertical axis wind turbines". In: *Journal of Propulsion and Power* 1.6 (1985), pp. 432–436.

[37] F. Baratchi et al. "Assessment of blade element actuator disk method for simulations of ducted tidal turbines". In: *Renewable Energy* 154 (2020), pp. 290–304.

[38] S. Spinner et al. "A Blade Element Theory Based Actuator Disk Methodology for Modeling of Fan Engines in RANS Simulations". In: *AIAA Aviation 2019 Forum* (June 2020). DOI: 10.2514/6.2020-2749. URL: https://doi.org/10.2514/6.2020-2749.

[39] S. Goldstein and L. Prandtl. "On the vortex theory of screw propellers". In: *Proceedings of the Royal Society of London Series A Containing Papers of a Mathematical and Physical Character* 123.792 (Apr. 1929), pp. 440–465. DOI: 10.1098/rspa.1929.0078. URL: https://doi.org/10.1098/rspa.1929.0078.

[40] C. Hughes. "Aerodynamic performance of scale-model turbofan outlet guide vanes designed for low noise". In: *40th AIAA Aerospace Sciences Meeting & Exhibit*. Jan. 2002. DOI: 10.2514/6.2002-374. URL: https://doi.org/10.2514/6.2002-374.

[41] H. Hoheisel. "Aerodynamic aspects of engine-aircraft integration of transport aircraft". In: *Aerospace Science and Technology* 1.7 (Oct. 1997), pp. 475–487. DOI: 10.1016/s1270-9638(97)90009-2. URL: https://doi.org/10.1016/s1270-9638(97)90009-2.

[42] E. Tinoco and A. Chen. "Transonic CFD applications to engine/airframe integration". In: *22nd Aerospace Sciences Meeting* (Jan. 1984). DOI: 10.2514/6.1984-381. URL: https://doi.org/10.2514/6.1984-381.

[43] I. Goulos et al. "Civil turbofan propulsion aerodynamics: Thrust-drag accounting and impact of engine installation position". In: *Aerospace Science and Technology* 111 (Jan. 2021), p. 106533. DOI: 10.1016/j.ast.2021.106533. URL: https://doi.org/10.1016/j.ast.2021.106533.

[44] H. Kodama and S. Nagano. "Potential Pressure Field by Stator/Downstream Strut Interaction". In: *Journal of Turbomachinery* 111.2 (Apr. 1989), pp. 197–203. DOI: 10.1115/1.3262256. URL: https://doi.org/10.1115/1.3262256.

[45] A. B. Parry. "Optimisation of Bypass Fan Outlet Guide Vanes". In: *Volume 2: Aircraft Engine; Marine; Microturbines and Small Turbomachinery* (June 1996). DOI: 10.1115/96-gt-433. URL: https://doi.org/10.1115/96-gt-433.

[46] A. Savelyev et al. "Nacelle design and optimization for ultra high bypass ratio turbofan". In: *Proc., Greener Aviation Conf. Melville, NY: AIP Publishing LLC*. 2016.

[47] F. C. Mund and P. Pilidis. "Performance simulation of a high-bypass turbofan with a 2D representation of the intake and fan components". In: *The Aeronautical Journal* 112.1137 (Nov. 2008), pp. 673–682. DOI: 10.1017/s0001924000002645. URL: https://doi.org/10.1017/s0001924000002645.

[48] M. Robinson et al. "Nacelle design for ultra-high bypass ratio engines with CFD based optimisation". In: *Aerospace Science and Technology* 113 (Sept. 2020), p. 106191. DOI: 10.1016/j.ast.2020.106191. URL: https://doi.org/10.1016/j.ast.2020.106191.

[49] Y. Kaplan. "Aerodynamic optimization of inlet design for high bypass ratio turbofan". MA thesis. Middle East Technical University, 2024.

[50] S. Farokhi. *Aircraft Propulsion*. 2nd ed. John Wiley and Sons, 2014, p. 339.

[51] H. Zimmermann et al. "CFD Study of Nozzle Configurations for Ultra High Bypass Engines". In: *International Gas Turbine and Aeroengine Congress and Exposition*. the American Society of Mechanical Engineers (ASME), May 1993. DOI: 10.1115/93-gt-389. URL: https://doi.org/10.1115/93-gt-389.

[52] M. Zennaro. "CFD Simulation of a Transonic Fan: Mesh sensitivity study, mapping and 3D validation". MA thesis. Università degli Studi di Padova, 2020.

[53] F. Mund et al. "Enhanced Gas Turbine Performance Simulation Using CFD Modules in a 2D Representation of the Low-Pressure System for a High-Bypass Turbofan". In: *Journal of Engineering for Gas Turbines and Power* 129.3 (Feb. 2006), pp. 761–768. DOI: 10.1115/1.2364197. URL: https://doi.org/10.1115/1.2364197.

[54] A. Heidebrecht et al. “Parametric Geometry and CFD Process for Turbofan Nacelles”. In: *ASME Turbo Expo 2016: Turbomachinery Technical Conference and Exposition*. the American Society of Mechanical Engineers (ASME), June 2016. DOI: 10.1115/gt2016-57784. URL: https://doi.org/10.1115/gt2016-57784.

[55] F. Menter. “Improved two-equation k-omega turbulence models for aerodynamic flows”. In: *NASA STI/Recon Technical Report N* 93 (Oct. 1992), pp. 22809–. URL: https://ntrs.nasa.gov/api/citations/19930013620/downloads/19930013620.pdf.

[56] F. Menter. “Zonal Two Equation k-w Turbulence Models For Aerodynamic Flows”. In: *23rd Fluid Dynamics, Plasmadynamics, and Lasers Conference* (July 1993). DOI: 10.2514/6.1993-2906. URL: https://doi.org/10.2514/6.1993-2906.

[57] S. Ahlinder. “On Modelling of Compact Tube Bundle Heat Exchangers as Porous Media for Recuperated Gas Turbine Engine Applications”. PhD thesis. BTU Cottbus-Senftenberg, 2006.

[58] S. Grace et al. “Correction: Statistics and structure of turbulence in fan/FEGV interstage and their aeroacoustic implications”. In: *AIAA/CEAS Aeroacoustics Conference* (June 2018). DOI: 10.2514/6.2018-4186.c1. URL: https://doi.org/10.2514/6.2018-4186.c1.

[59] F. Beltrame et al. “Reduced Order Modelling of optimized Heat Exchangers for Maximum Mass-Specific Performance of Airborne ORC Waste Heat Recovery Units”. In: *Proceedings of the 7th International Seminar on ORC Power Systems*. Jan. 2024, pp. 563–573. DOI: 10.12795/9788447227457\{_}93. URL: https://doi.org/10.12795/9788447227457_93.

[60] I. Celik et al. “Procedure for estimation and reporting of uncertainty due to discretization in CFD applications”. In: *Journal of fluids Engineering-Transactions of the ASME* 130.7 (2008).

[61] ANSYS Innovation Space. *fluent : turbulent flow u+ vs y+*. 2018. URL: https://innovationspace.ansys.com/forum/forums/topic/fluent-turbulent-flow-u-vs-y/ (visited on 2024).

[62] C. Clemen, P. Albrecht, and S. Herzog. “Systematic Optimisation of a Turbofan Bypass Duct System”. In: *Proceedings of ASME Turbo Expo 2012*. the American Society of Mechanical Engineers, June 2012, pp. 1655–1666. DOI: 10.1115/gt2012-68276. URL: https://doi.org/10.1115/gt2012-68276.

[63] R. Bajimaya et al. “Heat exchanger integration with an aero-engine bypass duct”. In: *Aerospace Europe Conference 2023 – 10th EUCASS – 9th CEAS* (2023).

[64] D. W. Zingg, M. Nemec, and T. H. Pulliam. “A comparative evaluation of genetic and gradient-based algorithms applied to aerodynamic optimization”. In: *European Journal of Computational Mechanics* (Aug. 2008), pp. 103–126. DOI: 10.13052/remn.17.103-126. URL: https://doi.org/10.13052/remn.17.103-126.

[65] H. Witte and C. Bode. “Gradient-Based Optimization of the Propulsor Bypass Duct Under the Influence of Functionally Integrated Heat Transfer Structures”. In: *AIAA SCITECH 2025 Forum*. The American Institute of Aeronautics and Astronautics, 2025, p. 2107. DOI: 10.2514/6.2025-2107. URL: https://doi.org/10.2514/6.2025-2107.

[66] K. Schittkowski. “NLPQL: A fortran subroutine solving constrained nonlinear programming problems”. In: *Annals of Operations Research* 5.2 (June 1986), pp. 485–500. DOI: 10.1007/bf02022087. URL: https://doi.org/10.1007/bf02022087.

[67] N. Salem. *Parameterized Finite Element Analysis With Optimization of a Superplastic Forming Process Using ANSYS®*. DAAAM International, Jan. 2017, pp. 319–332. DOI: 10.2507/daaam.scibook.2017.24. URL: https://doi.org/10.2507/daaam.scibook.2017.24.

[68] R. Christie et al. “The use of hybrid intuitive class shape transformation curves in aerodynamic design”. In: *Aerospace Science and Technology* 95 (Oct. 2019), p. 105473. DOI: 10.1016/j.ast.2019.105473. URL: https://doi.org/10.1016/j.ast.2019.105473.

[69] H. Sobieczky. “Parametric Airfoils and Wings”. In: *Notes on Numerical Fluid Mechanics* 68, Vieweg Verlag (1999), pp. 71–88.